Effects of lava ponding on Hawaiian fountain heights: an experimental investigation

PEARCE CONDREN

How to cite:

CONDREN, PEARCE (2019) Effects of lava ponding on Hawaiian fountain heights: an experimental investigation. Masters thesis, Durham University.

Effects of lava ponding on Hawaiian fountain heights: an experimental investigation

Pearce Joseph Condren

Department of Earth Sciences

Durham University

2019

This thesis is submitted to Durham University for fulfilment of the requirements for an MSc by research in Volcanology.

Abstract

Hawaiian eruptions are characterized by long-lived eruptions that produce lava fountains that last 300-10000 seconds and can reach 10s to 100s of meters high. During an eruption pyroclasts can fall back and accumulate proximal to the eruption site, forming ramparts or scoria cones that create topographic wells. Lava can accumulate within these topographic wells, creating lava ponds that may affect the behaviour of subsequent lava fountains. When a fountain ascends through a lava pond, it entrains previously erupted pyroclasts and accelerates them; this reduces the flow velocity of the ascending fountain, decreasing its overall height. Published studies have examined the relationship between ponding and variations in lava fountain heights from a theoretical perspective, though these studies have not yet received experimental verification. For this reason, an experimental kit is designed to conduct scaled analogue experiments to investigate the variation of fountain heights with ponding depth. Dimensional analysis is used to facilitate the comparison between laboratory and natural behaviours, while experiments are performed for varying parameters of; pressure head, ponding depth, conduit diameter and fluid viscosity. The collected dataset indicates that increasing volumetric flux corresponds to greater fountain heights, while increased ponding depth reduces fountain heights. A dimensionless model is then identified between dimensionless fountain height and dimensionless ponding depth, which allows the reduction in fountain height due to ponding to be evaluated.

The Road goes ever on

by J.R.R Tolkien.

Roads go ever ever on,

Over rock and under tree,

By caves where never sun has shone,

By streams that never find the sea;

Over snow by winter sown,

And through the merry flowers of June,

Over grass and over stone,

And under mountains in the moon.

Roads go ever ever on

Under cloud and under star,

Yet feet that wandering have gone

Turn at last to home afar.

Eyes that fire and sword have seen

And horror in the halls of stone

Look at last on meadows green

And trees and hills they long have known.

Table of Contents

List of Figures

List of Tables

1. Geological Context

1.1 Motivation for study

Basaltic volcanism produces the majority of the earth's magma output and can occur in a wide variety of tectonic settings; forming in extensional, convergent, or intraplate settings (Crisp 1982, Valentine and Gregg 2008). Over 75% of volcanism on the planet occurs at mid ocean-ridges, while the remainder of volcanic activity occurs in subduction, intraplate or continental settings (Crisp 1982). In a continental setting, basaltic volcanoes are the most abundant type of volcano on the planet (Valentine and Gregg 2008).

Basaltic eruptions typically initialize as fissures when a dyke intersects the earth's surface (Fig 1.1), and can feature episodes of lava fountaining, where pyroclastic materials are ejected vertically from a vent several hundreds of meters into the air (Swanson et al 1979, Valentine and Gregg 2008, Orr et al 2015, Wolfe et al 2018). Well documented cases of lava fountaining behaviour exist for historic eruptions such as during the 2014 Holuhruan eruption in Iceland or the 1983 Pu'u 'O'o eruption of Hawaii's Kīlauea volcano (Swanson et al 1979, Witt et al 2018). Eruptions then localize over time due to solidification of magma within a fissure, eventually localizing to singular vents (Bruce and Huppert 1990). Ejected pyroclasts are deposited proximally to the eruption site, which accumulate to construct spatter ramparts or scoria cones (Fig 1.2) (Swanson et al 1979, Witt et al 2018, Wolfe et al 1988). Cones and ramparts create topographic wells within which lava may pond, flooding the eruption site and consequently altering the behaviour of subsequent lava fountains (Swanson et al 1979, Wolfe et al 1988, Jones et al 2017). Lava ponds reduce lava fountain heights or may suppress lava fountaining entirely, such as during the 2015 Kamoamoa fissure eruption Hawaii’s Kīlauea volcano (Wilson et al 1995, Orr et al 2015).

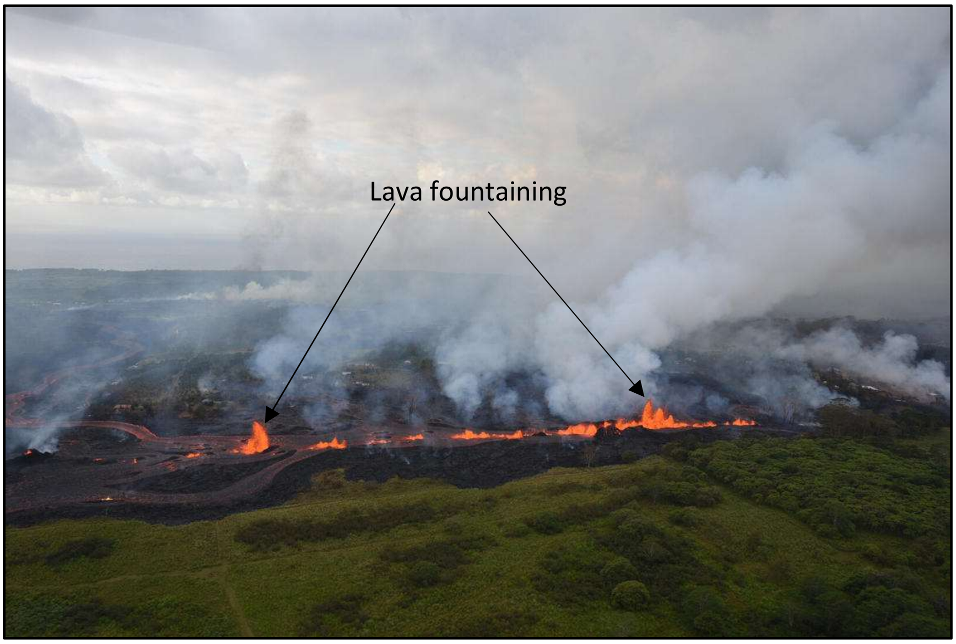

Figure 1.1: Basaltic fissure eruption undergoing an episode of lava fountaining. Photograph taken from the lower east rift zone of Hawaii’s Kīlauea volcano on the 19th of May 2018 by the United States Geological Survey.

Published theoretical models have examined how lava fountain behaviour varies with; gas content, volumetric flux, conduit geometry, viscosity, bubble coalescence and ponding depth (Head and Wilson 1987, Wilson et al 1995, Parfitt et al 1995. However, published models have yet to be validated by experimental means. Therefore, this study aims to produce a dataset against which published theoretical models (Wilson et al 1995, Parfitt et al 1995) could be validated. This approach intends to provide insight into the fundamental processes defining fountains using carefully scaled laboratory experiments. Scaled experiments provide insights into fountain behaviour which can’t otherwise be replicated through modelling or field observations.

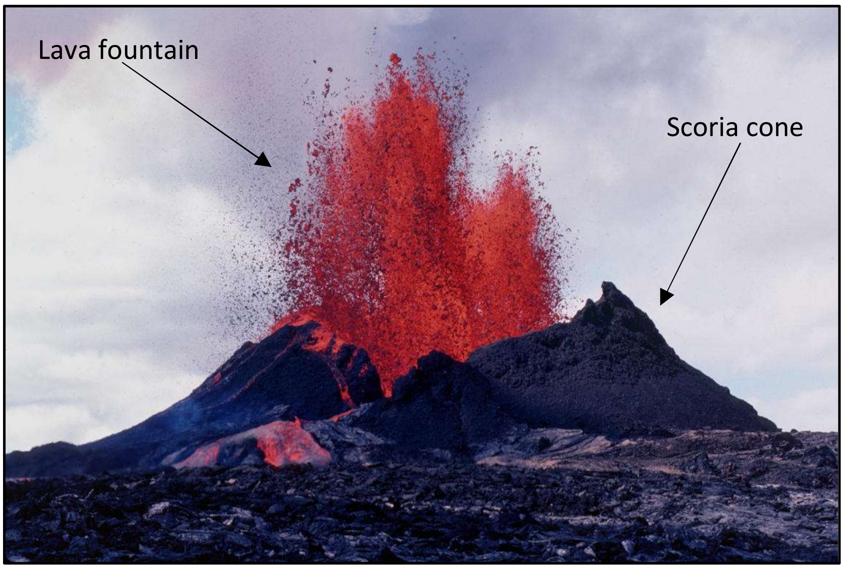

Figure 1.2: 50 m Lava fountaining from a localized vent. Accumulated spatter has formed a scoria cone around the vent. Photograph taken during eruption episode 8 of the Pu’u ‘O’o eruption of Hawaii’s Kīlauea volcano, on the 6th of September 1983 by the United States Geological Survey.

1.2 Basaltic eruptions

Basaltic eruptions are the most common form of volcanic activity on the planet (Crisp 1982, Parfitt 2004). While many styles of eruptions exist, sub-aerial basaltic eruptions consist predominantly of 3 varieties; effusive eruptions, Strombolian eruptions and Hawaiian eruptions (Parfitt 2004, Valentine and Gregg 2008).

Effusive eruptions are defined by lava flows emanating from a vent or fissure (Parfitt 2004, Valentine and Gregg 2008). Strombolian eruptions are characterized by mild, short-lived (<20 seconds) explosions from a vent due to the accumulation of gas beneath ascending magma within a conduit (Parfitt 2004, Valentine and Gregg 2008, Houghton et al 2016). Hawaiian eruptions occur along both fissures and vents, they are defined by long-lived eruptions that generate lava fountains that are 10s to several 100s of meters in height (Parfitt 2004, Valentine and Gregg 2008). Hawaiian eruptions are distinguished from Strombolian eruptions by their increased mass flux and duration, lasting 300-10000 seconds longer on average than Strombolian eruptions (Parfitt 2004, Valentine and Gregg 2008, Houghton et al 2016).

Lava fountains are comprised of pyroclasts, as well as fragmented material consisting of ash, lapilli and spatter (Swanson et al 1979, Wolfe et al 1988, Sumner et al 2005). Pyroclasts within lava fountains undergo variable cooling rates, due to the presence of a thermal gradient within the fountain (Fig 1.3), pyroclasts at the fountain’s centre are thermally insulated, producing highly vesicular clasts due to continued bubble coalescence, while clasts at the fountain edges are cooled much more quickly due to greater thermally diffusivity (Stovall et al 2010).

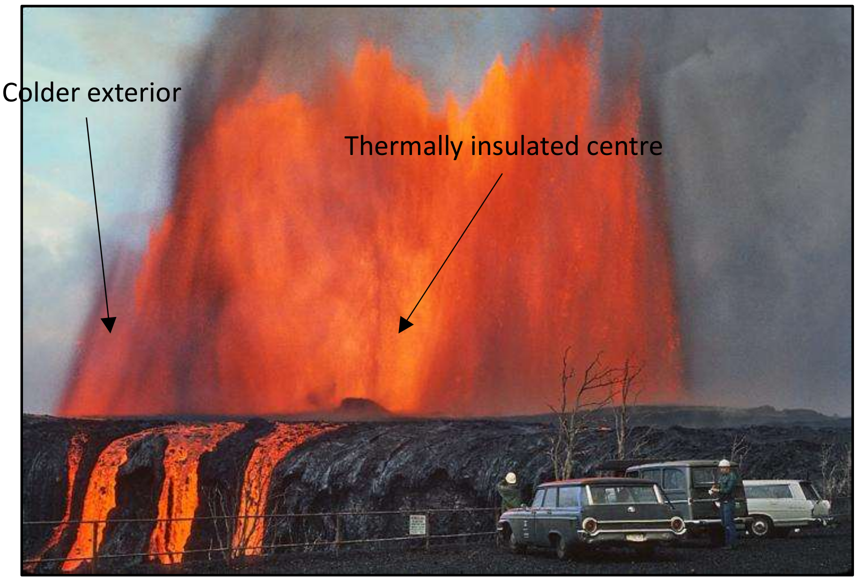

Figure 1.3: A 300m high lava fountain during the 1969 Mauna Ulu eruption, photo taken on the 30th of December 1969, by the United States Geological Survey. Clasts at the centre of the fountain (brighter area) are thermally insulated while clasts at the fountain's exterior (darker area) cool quicker.

The type of clasts derived from fountains are dependent upon their position within the fountain, clasts produced in the interior are comprised of three predominant types (Sumner et al 2005). The three types of interior clasts are; fluid clasts, which stick together upon impact, fluidal clasts, that splash on impact and clasts with a brittle core/fluid rim formed from recycled pyroclasts (Sumner et al 2005). Clasts produced within the fountain exterior consist of brittle clasts (scoria) and clasts with viscous rims/fluid interiors (Sumner et al 2005).

The continued accumulation of pyroclasts during an eruption can construct spatter ramparts along fissures, or form scoria cones when deposited proximally to a single vent. (Sumner et al 2005, Reynolds et al 2016, Swanson et al 1979, Wolfe et al 1988). The geometry of spatter deposits is influenced by pre-existing local topography (Percheta et al 2012). Downslope transport and remobilization of previously erupted spatter can alter deposit structure, producing asymmetrical ramparts and cones (Swanson et al 1979, Percheta et al 2012, Witt et al 2018).

1.3 Localization

Over time fissure eruptions exhibit a shift in behaviour, with eruptions becoming increasingly localized to fewer localities along the length of a fissure (Bruce and Huppert 1990, Jones et al 2017). Localization is a well-documented process during basaltic fissure eruptions, such as during the 1969 Mauna Ulu, 1983 Pu'u 'O'o and 2011 Kamoamoa eruptions of Hawaii's Kīlauea volcano (Swanson et al 1979, Wolfe et al 1988, Orr et al 2015). Localization occurs due to magma solidification within a dyke, either as a result of magma stagnation, or due to the volcanic conduit becoming blocked during an eruption (Swanson et al 1979, Bruce and Huppert 1990, Jones et al 2017).

Magma flowing through a dyke loses heat to the colder surrounding country rock as it ascends, causing it to stagnant and eventually solidify along the margins of the dyke (Bruce and Huppert 1989, Bruce and Huppert 1990). The rate at which solidification occurs is dependent upon dyke geometry, magma temperature and flow rate (Delany and Pollard 1982). Eruptions with low magma discharge may only be sustained for several hours before total solidification occurs within a conduit (Delany and Pollard 1982).

Solidification modifies the conduit shape, decreasing the diameter of the affected conduit, which restricts flow (Bruce and Huppert 1989). The restriction of flow causes magma to ascends at reduced rates, which increases the amount of heat advection occurring and therefore increases the rate of solidification (Bruce and Huppert 1989).

Continued discharge without the complete solidification of a conduit can reverse the solidification process by re-melting the solidified magma along the dyke’s margin, widening the conduit and promoting increased flow (Bruce and Huppert 1989, Bruce and Huppert 1990).

A fissure eruption is therefore comprised of several “fingers”, hot regions of continued discharge separated by colder regions which progressively solidify and clog the fissure, eventually restricting an ongoing eruption to a small number of vents or a single source (Helfrich 1995).

1.4 Lava fountain mechanics

Lava fountains are formed due to the decompression of magma during ascent within a conduit, causing fragmentation as gases exsolve from rising magma (Wilson et al 1995, Parfitt et al 1995, Parfitt and Wilson 1995). Exsolved gases expanded due to decreasing pressure as they ascend, accelerating the surrounding denser magma, which produces a lava fountain (Swanson et al 1979, Wilson et al 1995, Parfitt and Wilson 1995).

Fountains are defined as jets with a downward acting buoyancy force, driven upwards by momentum from a source till they reach a steady height about which they fluctuate (Turner 1966, Lin and Linden 2005). The momentum of a fountain decreases with height till it becomes zero, where upon reaching this point fluid falls down around the upward flowing jet (Turner 1966). The interaction between these regions of up-flow and down-flow (Fig 1.5) within a fountain reduce the maximum achievable fountain height (Turner 1966, Bloomfield and Kerr 2002, Lin and Linden 2005).

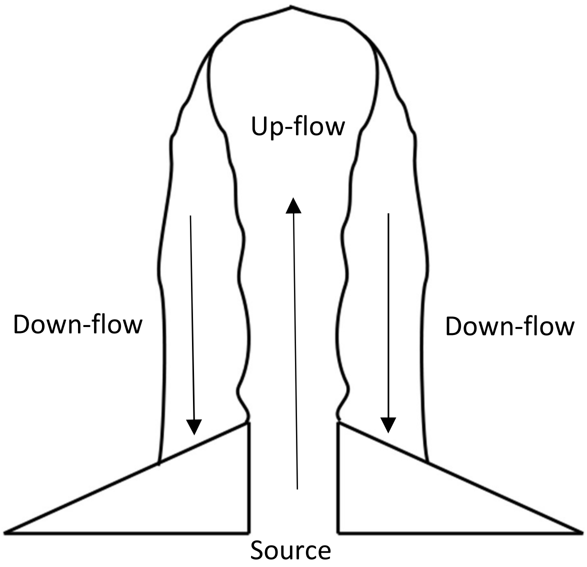

Figure 1.4: Schematic drawing of a fountain, illustrating regions of up-flow and down-flow (modified from figure 1 of Turner 1966).

Lava fountain height is a function of magma gas content, volumetric flux, bubble coalescence, viscosity and conduit geometry, with volumetric flux and gas content being considered the primary controls on fountain height and structure (Wilson et al 1995, Parfitt et al 1995, Head and Wilson 1998). Higher volumetric fluxes and gas content result in the formation of higher fountains (Fig 1.6), while higher viscosities decrease flow velocity, reducing fountain height (Wilson and Head 1981, Wilson et al 1995). Fountain temperature and the accumulation rate of pyroclasts are dependent upon volumetric flux and gas content, determining whether lava flows or spatter constructs are formed during an eruption (Head and Wilson 1998).

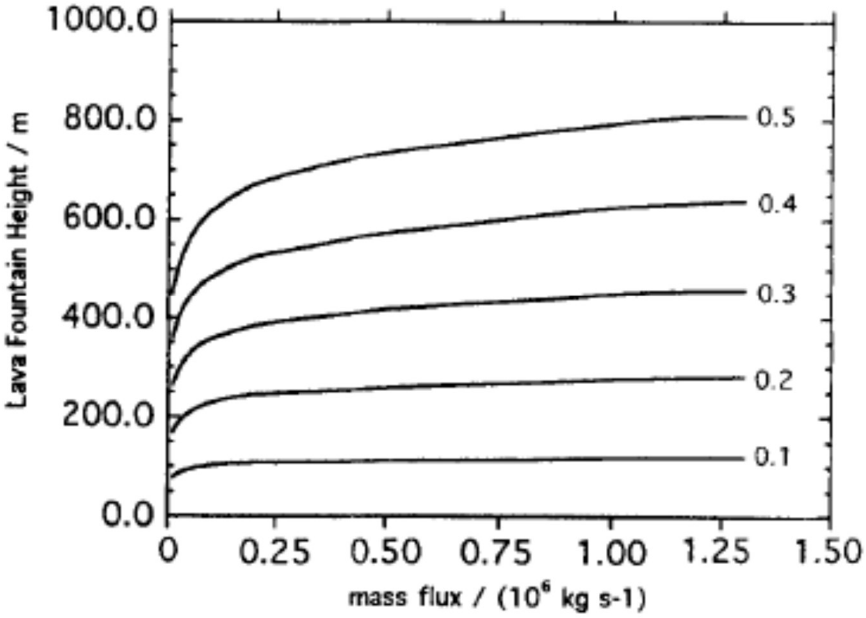

Figure 1.5: Lava fountain height as a function of erupted mass flux and magma gas content (curves labelled in weight percentage of water), taken from Figure 2 of Wilson et al 1995.

Lava fountain height has been observed to increase with ongoing localization, lava fountains during the 1969 Mauna Ulu eruption ranged from 10s of meters along the length of the fissure, to 100s of meters as localization continued, the largest fountain of the entire eruption reaching 540m in height and was confined to a single vent (Swanson et al 1979). This increase in fountain height is explained by the previously mentioned dependency of fountain height on volumetric flux, the ascending magma supply is confined to a smaller number of vents after localization, increasing the volumetric flux through the remaining open vents, which produces larger fountains (Wilson et al 1995).

1.5 Lava Ponding

The accumulation of lava within topographic wells, also known as ponding, occurs when the discharge rate of lava from a vent exceeds the drainage rate of lava from the eruption site (Swanson et al 1979, Jones et al 2017, Witt et al 2018). Lava ponds consist of two varieties, active lakes; when formed directly on top of an active vent, or inactive lakes; when form by passive ponding within pre-existing local topographic wells (Tilling 1987). The depth of lava ponds can vary from 10s to 100s of meters during the course of an eruption and fluctuation over time (Tilling 1987, Orr et al 2015).

Individual vents are more prone to becoming flooded due to constructed spatter ramparts and scoria cones forming local topographic wells in which lavas may accumulate (Wilson et al 1995). Fissure eruptions are less susceptible to being flooded, due to the availability of additional lava drainage pathways (Wilson 1995, Jones et al 2017). The formation of lava ponds alters the behaviour of subsequent lava fountains during an eruption, reducing the height of fountains that ascend through lava ponds (Swanson et al 1979, Wolfe et al 1988, Orr et al 2015). Variation in fountain heights with ponding depth is due to the effects of entrainment, the process by which an ascending lava fountain incorporates surrounding pre-erupted material into its up-flow, expending energy to accelerate the newly incorporated material (Wilson et al 1995, Parfitt et al 1995). Previously erupted pyroclasts are “recycled” into the ascending fountain, decreasing flow velocity and therefore decreasing fountain height. A fountain’s susceptibility to the effects of entrainment is related to the fountain’s volumetric flux (Fig 1.7), increasing volumetric flux lessens the effects of entrainment (Wilson et al 1995, Parfitt et al 1995). Low volumetric flux fountaining can be suppressed entirely for sufficiently large ponding depths, such as during the 2011 Kamoamoa fissure eruption of Hawaii's Kīlauea volcano (Wilson et al 1995 Orr et al 2015). Fountain suppression causes underlying magma to stagnate within a conduit, increasing magma viscosity and promoting localization (Jones et al 2017). Ascending magma within a fissure can laterally migrate to avoid areas of suppression and stagnation more readily than individual vents, causing progressive shifts in activity over the course of an eruption (Wolfe et al 1988, Jones et al 2017).

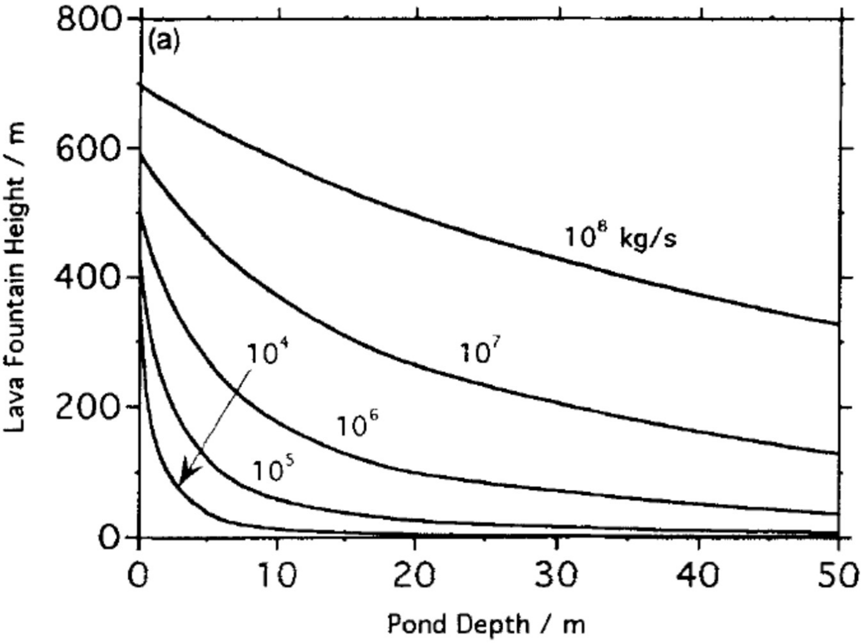

Figure 1.6: Variation of lava fountain height with increasing ponding depth for a series of erupted mass fluxes (black curves) with a water content of 0.3 weight percentage (taken from Figure 5 Wilson et al 1995).

2. Experimental Scaling

2.1 Introduction

To investigate lava fountain behaviour in the laboratory, experiments must be conducted on a smaller scale than otherwise found in nature. When reducing the scale of the system, it is important that the processes observed within the laboratory are comparable to those that would be observed in the natural system. This is accomplished by utilizing scaling analysis for experiments.

When adjusting experiments to a smaller scale, it is necessary to scale material properties, in this case fluid viscosity, to maintain dynamic similarity.

This chapter begins with detailing how dimensional analysis facilitates drawing a relationship between laboratory data and the lava fountain behaviour in nature. Buckingham Pi theorem is then explored as a method of dimensional analysis, with a worked example of the calculations conducted. The chapter concludes with addressing the scaling of materials to emulate nature.

Mathematical notation is defined at first use and a complete summary of notation is presented within Appendix A.

2.2 Dimensional analysis

The comparison, addition or subtraction of quantities must be between quantities of the same dimension, i.e. time cannot be subtracted from length. When expressing the magnitude of quantities in identical units, such as length and diameter, those quantities are said to be dimensionally homogenous.

Each physical quantity with both a magnitude and a dimension can be also be expressed in its basic units, the fundamental units from which other unit systems are derived. There are seven fundamental units; length (m), mass (kg), time (s), temperature (°C), ampere (A), candela (cd) and mole (mol). Dimensional analysis seeks to create dimensionless groups that detail the regimes of behaviour, as they are dimensionless, they are scale independent and can be used as a direct comparison between the laboratory and nature to garner insight into natural processes.

One such dimensionless group is the Reynolds number, it represents the ratio of inertial forces to viscous forces within a fluid, which is a dimensionless measure of the ordering of flow streamlines within a fluid (Reynolds 1883). The Reynolds number, Re, is defined by the following equation:

$$Re = \frac{\rho V D}{\mu}. \tag{2.1}$$

where ρ (kg/m^3) is the fluid density, V (m/s) is the flow velocity, D (m) is the pipe diameter and μ (Pas) is the viscosity. The technique for dimensional analysis utilized by this study is known as Buckingham Pi theorem and the method of doing so will now be discussed.

2.2.1 Buckingham Pi theorem

The number of dimensionless groups, also known as Π groups, which describe the behaviour of a system are related to the number of governing parameters of a system and the number of independent dimensions present, as described by the following equation:

$$m = n - k \qquad 2.2$$

where m is the number of dimensionless groups, n the number of governing parameters and k the number of independent basic units (Buckingham 1914).

To determine the number of governing parameters that are relevant to this study, quantities that are expected to affect fountain height in the natural system must be considered and how they might affect the dependent variable. The dependent variable for this study is the fountain height h (m), the measured quantity of interest.

The governing parameters of interest to this study are expressed in terms of their fundamental units in table 2.1 (these parameters and their relevance to experiments are detailed in chapter 3). Having identified the governing parameters, the number of basic units present for the system must be determined. From table 2.1 it is evident that that there are 3 basic units present: length [L], mass [M] and time [T]. Applying equation 2.2 for the 9 governing parameters detailed in table 2.1 and their 3 basic units, indicates that there are six independent Π groups present.

Next the repeating variables must be selected, these are a number of variables equal to the number of basic units represented amongst the governing parameters.

The following rules should be adhered to when choosing repeating variables: these variables must not form a Π group by themselves; all the basic units must be represented; no two repeating variables can have the same basic units, dimensionally simple variables should be prioritized (variables with only 1 basic unit); and the dependent variable, which is h, must not be chosen (Buckingham 1914).

The chosen repeating variables for this analysis are: ρ, V and D and when expressed together in their basic units give a value with units $\mathrm{L}^{-1}M\mathrm{T}^{-1}$, which is a non-dimensionless group. The calculation for the first Π group will now be demonstrated while the remaining groups will simply be listed.

To determine a Π group the repeating previously identified repeating variables are taken along with any of the other governing parameters, in this case fountain height, then raised by an unknown power. Therefore the first Π group becomes;

$$\Pi_1 = \rho^a V^b D^c h^d \tag{2.3}$$

Each variable is then expressed in terms of their basic units, so that:

$$\Pi_1 = [L^{-3a} M^a][L^b T^{-b}][L^c][L^d] \tag{2.4}$$

Each dimension must sum to zero to produce a Π group, so the terms for each basic unit are grouped and evaluated as a set of 3 simultaneous equations:

$$M\colon a = 0 \tag{2.5}$$

$$L\colon -3a + b + c + d = 0 \tag{2.6}$$

$$T: -b = 0 \tag{2.7}$$

	Length [L]	Mass [M]	Time [T]	Description
$\boldsymbol{h}$ (m)	1	-	-	Fountain height
$\boldsymbol{D}$ (m)	1	-	-	Pipe diameter
$\boldsymbol{z}$ (m)	1	-	-	Ponding depth
$\boldsymbol{\rho}$ (kg/$\mathbf{m^3}$)	-3	1	-	Fluid density
$\boldsymbol{P}$ (Pa)	-1	1	-2	Pressure
$\boldsymbol{\mu}$ (Pa s)	-1	1	-1	Fluid viscosity
$\boldsymbol{V}$ (m/s)	1	-	-1	Flow velocity
$\boldsymbol{g}$ (m/$\mathbf{s^2}$)	1	-	-2	Gravitational acceleration
$\boldsymbol{Q}$ ($\mathbf{m^3}$/s)	3	-	-1	Volumetric flux

Table 2.1: dimension matrix with governing parameters for system of interest, detailed in SI units and their respective fundamental units.

Equations 2.5-2.7 can then be solved such that $a = 0$, $b = 0$ and $d = -c$.

Using these values to simplify equation 2.3 then gives:

$$\Pi_1 = D^{-c} h^{d} \tag{2.8}$$

Evaluating $d = -c$ for when $c = 1$ then gives:

$$\Pi_1 = \frac{h}{D} \tag{2.9}$$

Which is dimensionless conduit diameter. This same methodology is repeated to calculate the remaining Π groups.

The second dimensionless group has ponding depth z as the additional variable:

$$\Pi_2 = \frac{z}{D} \tag{2.10}$$

The third dimensionless group has pressure P as the additional variable:

$$\Pi_3 = \frac{P}{\rho V^2}. \tag{2.11}$$

The fourth dimensionless group has gravitational acceleration as the additional variable and is expressed as:

$$\Pi_4 = \frac{Dg}{V^2}. \tag{2.12}$$

Which is dimensionless gravitational acceleration. This group is known as the Froude number and more commonly expressed as:

$${\Pi_4}^{-1/2} = \frac{V}{\sqrt{Dg}}. \tag{2.13}$$

The fifth dimensionless group has volumetric flux as the additional variable:

$$\Pi_5 = \frac{Q}{VD^2}. \tag{2.14}$$

The sixth dimensionless group has viscosity as the additional variable:

$$\Pi_6 = \frac{\rho VD}{\mu}, \tag{2.15}$$

Which is the Reynolds number as previously described previously for equation 2.1.

While Buckingham Pi theorem is an effective method of identifying dimensionless groups, other dimensionless groups can be determined by simply combining parameters with identical dimensions, such as two quantities that both have a basic unit of length [L].

As this study seeks to investigate the variation in fountain height with ponding depth, it would be useful to have a means of quantifying reductions in fountain height experienced in the presence of ponding. A final dimensionless group is therefore introduced to do so, which is dimensionless fountain height:

$$\Pi_7 = \frac{h}{h_o} \tag{2.16}$$

Where h is the measured fountain height (m) and h_o is mean un-ponded fountain height (m). The mean un-ponded fountain height is calculated for a given pressure head and pipe diameter by firstly summing the heights of un-ponded fountains for these parameters, then averaging this value to obtain h_o. This dimensionless group therefore indicates that when fountain height is unchanged, $\Pi_7 \cong 1$ (due to minor fluctuations) and when fountaining is suppressed entirely $\Pi_7 = 0$.

While all the derived dimensionless groups and the method by which they are determined are included above for the sake of completeness, some of these groups are not examined within this thesis. The dimensionless groups which will be examined by this thesis are as follows; equations 2.10, 2.15 and 2.16.

2.3 Scaling materials

Having identified the relevant dimensionless groups for scaling, the next challenge lies in properly scaling experimental materials, in this case fluid viscosity. It is apparent that the viscosity of the fluid will play a vital role in influencing fountain behaviour as it dictates the Reynolds number of the system. However, in nature the viscosity of basaltic lavas can range (Fig 2.1) from 10 to 10^5 Pas (Gonnermann and Manga 2007), which is impractical for use from the perspective of this study.

Instead of using such viscous fluids, manipulation of the Reynolds number equation provides a method of scaling experimental materials to be consistent with values found in the natural system. This accomplished due to have experimental control over 3 parameters within the Reynolds number, pipe diameter, pressure head (which in turn varies flow velocity) and fluid viscosity. To determine the appropriate viscosities for laboratory experiments, the Reynolds number encountered for the natural system must be evaluated. Approximating the range of values for pipe diameter, flow velocity and viscosity present in the natural system based on parameters detailed in the literature, allows an estimation of the range Reynolds numbers likely to be encountered.

Drawing from previously established studies, the ranges encountered for these parameters are assumed to be; an average density for basaltic lavas of 2750 $\mathrm{kg/m^3}$ (Daly et al 1966, Chistensen and Wilkens 1982, Moore 2001); velocities of the magnitude 10^1-10^2 m/s (Wilson et al 1980, Freret-Lorgeril et al 2018); viscosities of the magnitude 10-10^5 Pas (Gonnermann and Manga 2007); and vent diameters of the magnitude 10^0-10^1 m (Wilson et al 1980; Wilson et al., 1995).

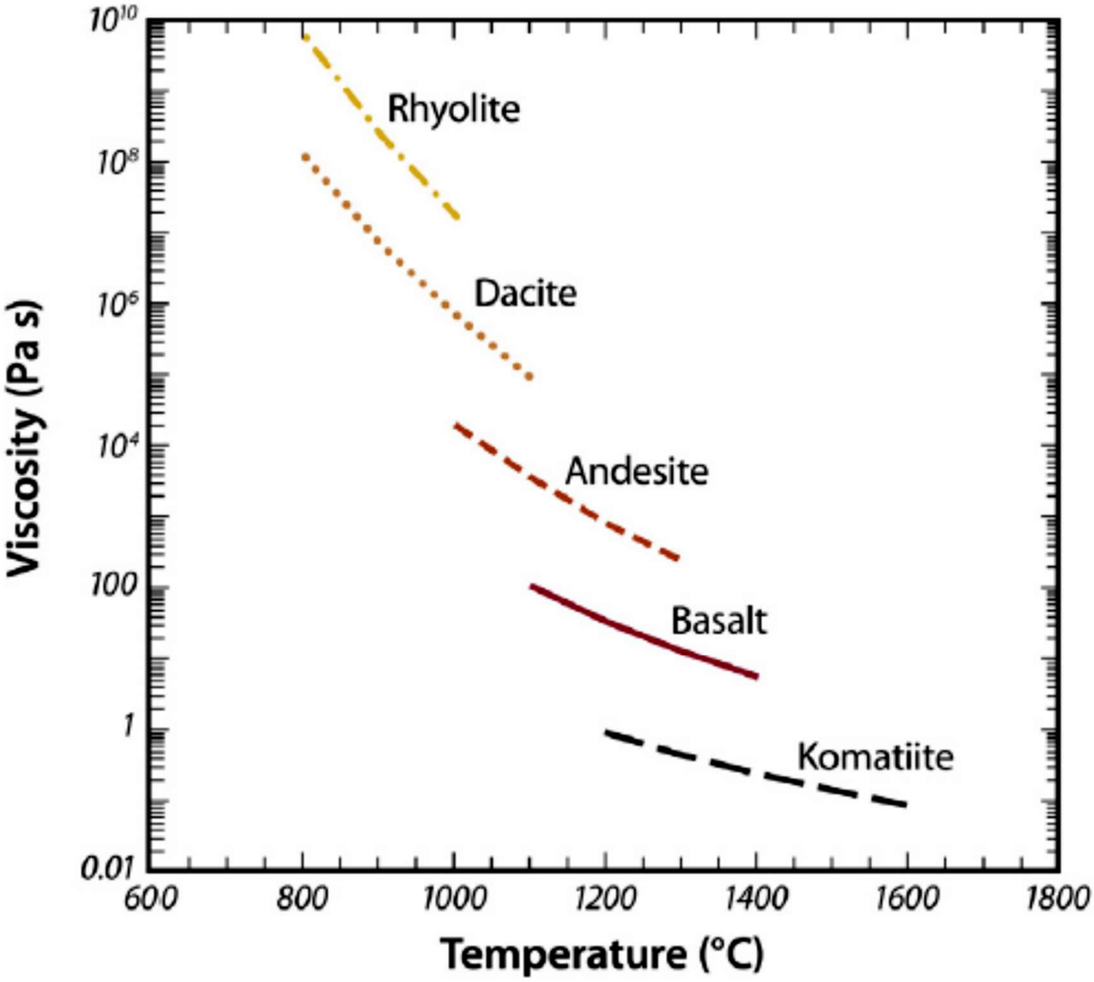

Figure 2.1: Viscosity as a function of temperature for a compositional range of lavas at a pressure of 1 bar, the temperature range is typical of eruptive temperatures for each composition (Taken from figure 5.4, page 123, Encyclopedia of volcanos)

The largest encountered Reynolds numbers would be present when the magnitudes of velocity and diameter are at their greatest and viscosity is at its lowest, such that:

$$Re = \frac{2750(10^2)(10)}{10}, \qquad 2.17$$

Evaluating this equation determines 275000 to be approximately the maximum value for Reynolds numbers expected in natural basaltic fountains. The lowest Reynolds numbers encountered would be present when the magnitudes of velocity and diameter are at their minimum and viscosity is at its maximum, such that:

$$Re = \frac{2750(10^{1})(10^{0})}{10^{5}}, \tag{2.18}$$

Solving this equation indicates that 0.275 is approximately the minimum Reynolds number encountered. The effective range of the Reynolds number in nature is therefore 0.275-275000.

Based on the previous calculations, natural lava fountains experience two different regimes of flow, either laminar or turbulent flows (Reynolds, 1883). As both these regimes occur in nature it is necessary to reflect that in experimental design, with chosen fluids being able to generate a comparable range of Reynolds numbers.

To accommodate this range, it is necessary to use fluids of differing viscosities within the laboratory to best capture the full suite of flow behaviour present in nature. Two fluids were identified for usage in experiments, water was chosen as a fluid due to ease of usage, and will be used to emulate the turbulent regime. It has a known viscosity of 8.9x10^{-4} Pa s. Golden syrup was identified as another suitable fluid, due to the ease with which it can be diluted with water to vary viscosity (this is further examined in chapter 4).

3. Experimental Methodology

3.1 Introduction

For carrying out experimental tests of fountain properties, an analogue experimental kit was constructed (Figure 3.1). A main consideration during design and construction was ensuring a functionally simple build, to allow for easy usage, while also allowing for tight controls to be placed on studied input parameters for experimental fidelity and easy measurement of output parameters.

This chapter begins with an overview of the components that make up the experimental kit (Detailed descriptions and technical drawings are available in Appendix B), which can be broadly divided into three sections; the tower, tank and vent. This is followed by a description of the experimental procedure used for data collection.

The remainder of the chapter details the methods employed for video analysis and data processing, with a description of the techniques used to extract usable data from recorded footage of fountain behaviour during testing (this data is available in chapter 5, Results and analysis).

Mathematical notation is defined at first use and a complete summary of notation is presented within Appendix A.

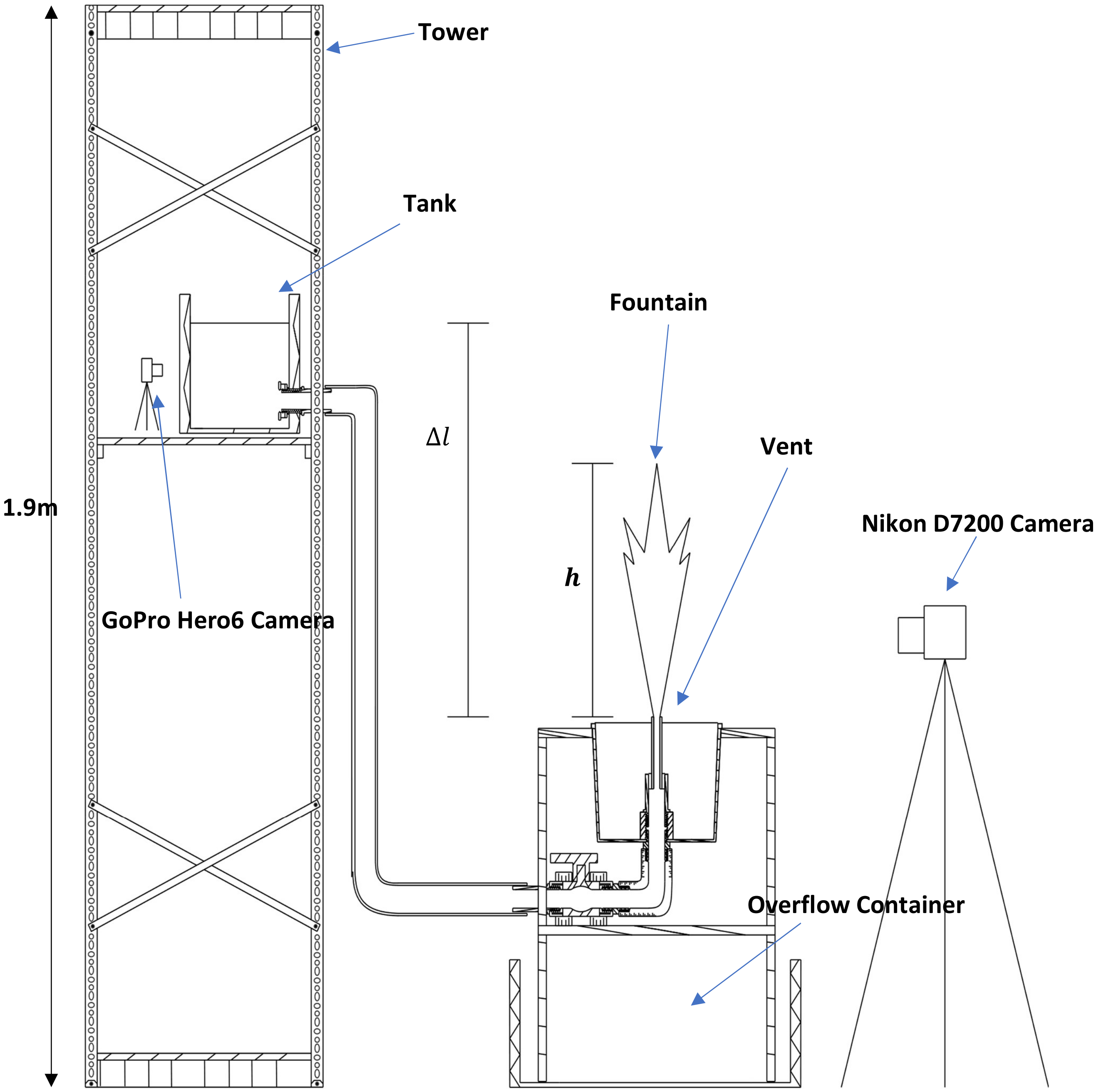

Figure 3.1: Experimental setup for collecting data. The driving pressure for flow is determined by Δl (m), the difference in elevation between the two fluid surfaces. The fountain height, h (m), is captured on a Nikon camera, while the GoPro records the rate at which the tank empties. An overflow container allows for fluid to be collected and recycled if necessary.

3.2 Tower

While the volcanic system is driven by buoyancy arising from bubble growth attempting to achieve equilibrium, in the laboratory the driving pressure for flow is generated by creating a pressure head. This pressure head is the difference in height between two fluid surfaces, the surfaces within the tank and vent. This relationship between pressure and height is expressed by the following equation:

$$P = \rho g \Delta l \tag{3.1}$$

Where P (Pa) is the pressure, ρ is the fluid density ($\mathrm{kg/m^3}$), g is the acceleration due to gravity ($\mathrm{m/s^{-2}}$) and Δl is the pressure head (m).

The tank sits on an adjustable platform within the tower, allowing Δl to be varied. The pressure heads examined were: 0.25, 0.75, 1 and 1.75m.

The tower has a solid frame and roof for stability, joined by slotted angle iron lengths. Joist struts attached at intervals along the tower reduce twisting effects.

3.3 Tank

The header tank is transparent to allow for the fluid level to be observed and recorded during experiments. A ruler placed within the tank provides a scale bar. An outlet within the tank has a flexible pipe, which with a diameter of 5.08cm, attached with t-clamps, joining the tank and vent together. Around the outlet, fixtures have o-rings attached to prevent leakage.

3.4 Vent

Pipe flow from the vent enters a plastic cylindrical tank mounted on a metal frame. This tank can be filled with liquid to create ponding, ponding depth is then varied by inserting pipes and affixing them in place at the desired depth. The pipe exit is positioned 8cm below the top of the tank, allowing for variation of ponding depth within that range. The ponding depths examined in this study were: 0 (the absence of ponding), 0.01, 0.02, 0.04 and 0.08 m. The pipe diameter can also be adjusted by inserting pipe lengths of smaller diameters and fixing them in place with plasticine, the pipe diameters used were 0.01, 0.018 and 0.03 m and were 0.15, 0.182 and 0.17 m in length respectively. To maintain a constant ponding depth, the tank is constantly overflowing.

A ball valve upstream of the pipe exit is used for controlling the flow of fluid from the tank to the vent. To prevent leakages, Polytetrafluoroethylene (PTFE) tape is placed around the threads of each plumbing fixture.

3.5 Experimental procedure

The apparatus is arranged as shown in figure 3.1 to the desired pressure head, checking that all structures are level and balanced. A ruler is secured against the side of the tank to measure the change in fluid level over time, with footage being recorded by a GoPro HERO6 camera (video footage shot at 1920x1080 pixels and 240 frames per second) with a Theia SL1250M varifocal telephoto lens.

The appropriate pipe section is chosen for the desired testing diameter and fixed in place at the desired ponding depth (Figure 3.2). For capturing the fountain generated from the vent, a Nikon D7200 camera with a Nikon AF-S DX 18-140 3.505.6G ED VR lens attachment is mounted on a tripod a sufficient distance from the vent so that the whole fountain body can be captured in frame (video footage shot at 1920x1080 pixels and 29.97 frames per second).

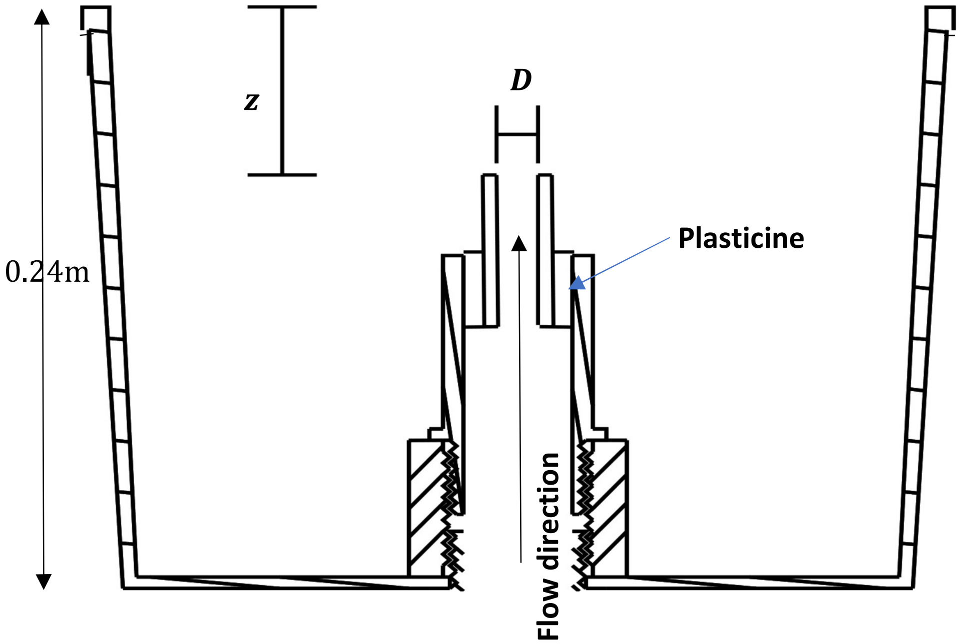

Figure 3.2: Vent sketch showing variation of ponding depth z (m) and pipe diameter D (m). Plasticine holds the smaller pipe in place.

To determine this distance, preliminary runs are done using conditions identical to those being tested. With both cameras now in place, the focus and zoom functions are adjusted to provide the highest definition video with markings being clearly visible. A metre stick is then placed into the vent and held upright, while being recorded by the Nikon camera. This footage is used as a reference frame later during footage analysis to determine fountain height.

After completing the previous steps, the valve is closed to ensure no flow into the vent and fluid is then loaded into the tank, filling it to the desired level. After this initial period of filling the tank, the valve is opened slightly to fill the vent to the brim, allowing some overspill, after which the valve is closed again. The tank is then filled again until the fluid reaches the required level.

All values for pressure head, pipe diameter, pipe length, ponding depth, fluid viscosity and respective timestamps are recorded in a notebook detailing experimental conditions. The air temperature within the laboratory is then measured and recorded using a thermocouple.

After completing these setup preparations, a final visual inspection is conducted to ensure that all factors are properly controlled and recorded, both cameras then start recording. A whistle is blown to provide an audio cue to help with synchronization between both cameras, with recording continuing for the duration of fountaining. The inspection of both cameras continues during fountaining to ensure that the video quality is clear throughout. Overspill from the tank is collected in an overflow tank surrounding the vent. When the experiment has finished, the valve is closed and the header tank is refilled for the next experiment.

3.6 Video analysis

The video footage of experiments is necessary for extracting two important values, the fountain height, h and the volumetric flux, Q. To obtain these values from the captured video requires the combined use of the VLC media player and imageJ, an image processing software (Abramoff et al 2004).

3.6.1 Fountain Height

A reference frame video (obtained as described in section 3.5) is loaded into the media player and examined by individual frames, searching for the clearest frames where the meter stick scale bar is visible. When finding the appropriate frame, a picture is taken using the media players snapshot feature, the picture is then opened in ImageJ to be examined. By measuring the height denoted by the ruler visible in the reference frame, a height scale can be determined for fountains recording using that respective reference frame (figure 3.3).

To account for parallax, the number of pixels per 10 cm height above the ponding surface is recorded. This is plotted to produce a calibration curve, such as that presented in figure 3.4. In most cases calibration curves show a linear relationship, however, in a minority of cases, the curve is nonlinear, indicating that parallax effects are present in the respective acquired footage.

Video footage from an experiment is then taken and examined in the media player software for periods of steady state fountaining, which is when the footage indicates that fountain behaviour is stable and height is not undergoing any major fluctuations. . The duration of these periods of steady state fountaining were dependent on the flow rate, varying anywhere between 1 second (during the highest flow rates) to 30 seconds in length (during the lowest flow rates). A snapshot of the fountain during this period (figure 3.5) is taken and then examined in the ImageJ software to determine the fountain height.

Figure 3.3: Example reference frame, where meter stick markings are clearly visible, with 10cm increments denoted by red markings.

3.6.2 Volumetric flux

Video footage from the GoPro is examined to determine volumetric flux. By measuring with a ruler, the tank was determined to have an area of 0.090475 ± $4.5\text{x}10^{-4}\mathrm{m}^2$ (error was calculated using equations presented in section 3.8), multiplying this by the height of the column of fluid present within the tank gives the volume of fluid present within the tank. While running an experiment, the height of the fluid column decreases while the tank drains. By taking the difference between the height of the fluid column before and after a

time interval, T, the change in volume can be determined. This is denoted by the following equation:

$$Q = \frac{v}{\mathrm{T}} \tag{3.2}$$

Where Q (m^3/s) is the volumetric flux, v (m^3) is the volume of the tank and T (s) is the elapsed time interval.

The time interval, T, varied depending on the rate of drainage from the header tank. When the flow rate was relatively low (such as using the narrow pipes), the time interval could be between 10-30 seconds in length. In instances with wider pipes the flow rate was much higher, the time interval was much shorter as a result, varying between 1-5 seconds in length. Error associated with this method was determined by taking a representative video and repeating the measurement 10 times, examining the number of frames (with each frame being 0.004167 seconds due to the high frame rate) by which each attempt deviated. Using this method error on time was determined to be 0.25 seconds.

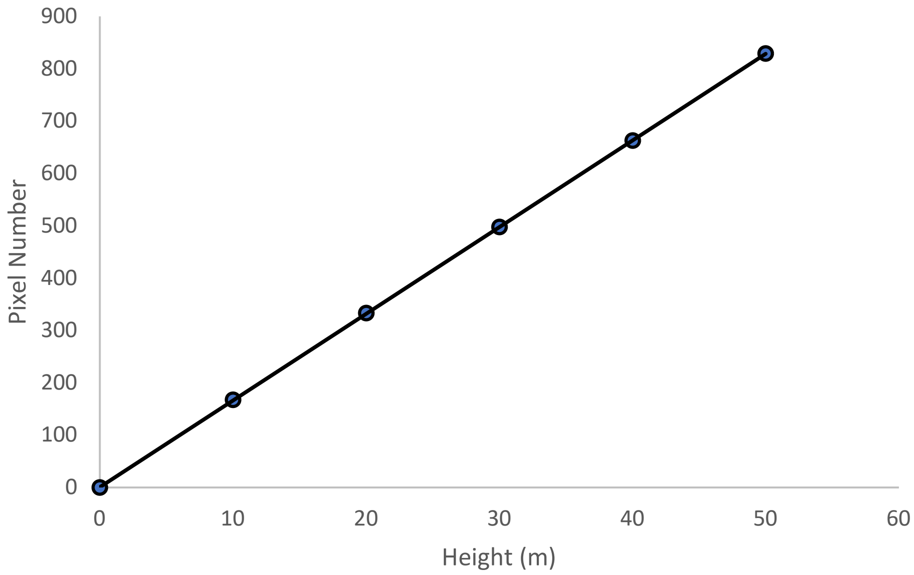

Figure 3.4: Calibration curve for reference frame displayed in Figure X.2. Best fit line of the form y = 16.551x + 1.153 (R^2=1). Plots for other reference frames display identical relationships in almost all cases. Error bars are smaller than data points.

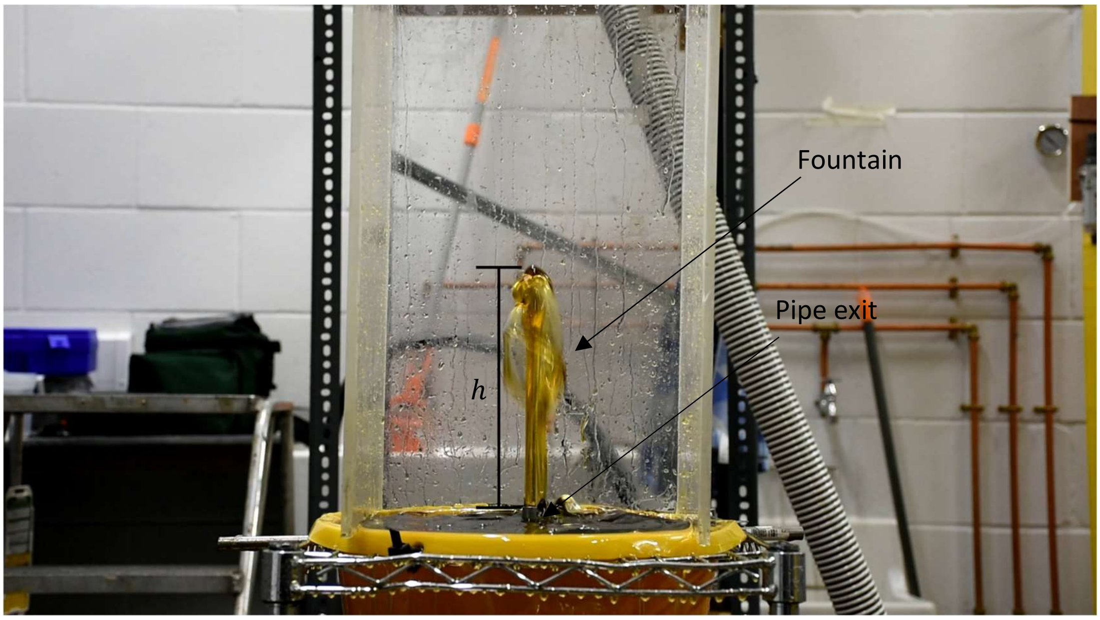

Figure 3.5: Image of fountain taken during steady state fountaining. Measurements for fountain height, h, are taken from the pipe exit.

3.7 Data processing

Taking the values for volumetric flux obtained through video analysis, the mean velocity of flow can be calculated using the following equation:

$$V = \frac{Q}{A} \tag{3.3}$$

Where V is the flow velocity (m/s) and A (m^2) is the cross-sectional area of the inserted pipe.

The pressure head determined using equation 3.1 is used to calculate a modelled flux to facilitate a comparison between modelled and measure flux values. Doing so provides a way of identifying potential anomalous experimental results. Performing this analysis requires calculation of the major and minor losses of pressure within the pipe system. Analysis of these losses are discussed in the next chapter.

3.8 Error analysis

It is necessary to account for uncertainties within collected data as these errors propagate through all calculations. Error analysis allows this uncertainty to be quantified. There are 3 equations by which this can be done:

$$S = a + b - c \rightarrow \delta S = \sqrt{(\delta a)^2 + (\delta b)^2 + (\delta c)^2} \tag{3.4}$$

$$S = \frac{ab}{cd} \rightarrow \frac{\delta S}{S} = \sqrt{\left(\frac{\delta a}{a}\right)^2 + \left(\frac{\delta b}{b}\right)^2 + \left(\frac{\delta c}{c}\right)^2 + \left(\frac{\delta d}{d}\right)^2} \tag{3.5}$$

$$S = x^n \rightarrow \frac{\delta S}{S} = \left|n \frac{\delta x}{x}\right| \tag{3.6}$$

where S, a, b, c and d are quantities, and δS, δa, δb, δc and δd are the uncertainties on each respective quantity. The uncertainties on measured values are determined through replicated measurements or approximated based on the preciseness of measurement techniques. Measurements taken using a ruler were taken to have an assumed error of $\pm\ 0.01$ m as this was smallest measurement the instrument was capable of making. Due to temperature measurements being made for the air temperature within the lab. rather than the fluid, errors on temperature adopted an overly conservative assumed error of $\pm$ 1 ℃ to compensate for any fluctuations that may have arisen while testing within the laboratory.

4. Mathematical Description of Flow

4.1 Introduction

Fluid dynamics is a branch of mathematics that details the flow of liquids and gases. It is used in a wide variety of disciplines, such as aerodynamics, hydrology and meteorology. With applications in such a wide variety of areas, a great deal of resources exist describing the governing conditions of fluid flow to better understand and predict associated phenomena.

This study seeks to draw from the body of pre-established mathematics for describing the processes involved with fluid flow within a pipe and applying them to determine the pressure loss along a pipe with added fixtures and fittings. This approach allows the comparison of measured and modelled flow rates.

The chapter starts with a description of the characteristic flow types; laminar and turbulent flow, along with the physical processes that define them. Then the chapter details the derivation and assumptions of the mathematical descriptions used when examining fluid flow to properly quantify the processes occurring within the experimental system. The chapter then examines the equations of pressure losses within a pipe due to the occurrence of friction and the presence of plumbing fixtures along the flow path. Equations to determine a modelled volumetric flux are addressed as a method of identifying anomalous experimental results. The chapter concludes with a description of scaling viscosity for golden syrup dilutions to emulate laminar flow. Mathematical notation is defined at first use and a complete summary of notation is presented within Appendix A.

4.2 Internal flow

An incompressible fluid flowing along a pipe has a characteristic velocity profile, the shape of which is dependent on the Reynolds number, and it is considered to be “fully developed” when displaying such a profile. When analysing fluid flow mathematically in this study, an important assumption is that flow is fully developed within a pipe. However, when initially entering a pipe, a fluid does not adopt this profile, it instead gradually develops across a characteristic development length. This entrance region where a flow lacks its full definition is referred to as the hydrodynamic entry region, while the area of fully developed flow is called the hydrodynamically fully developed region.

When entering the pipe, fluid particles moving in streamlines in contact with the pipe walls come to a stop due to frictional forces, causing them to have a velocity of zero. This process is known as the no-slip condition and has a significant impact in determining the shape of a fluid’s velocity profile. The now stationary particles along the boundary walls also slow adjacent fluid streamlines within the pipe, so to uphold the conservation of mass principle, the velocity at the centreline of flow increases (When the fluid is incompressible).

Flow can then be separated into two regions within a pipe (Fig 4.1). The first region is the boundary layer, the region of flow where shearing forces due to viscous effects and large changes in velocity are experienced perpendicular to the flow direction. The second region is known as the core flow region, where frictional effects are considered negligible and velocity is constant. For laminar flow, boundary layer thickness increases in the direction of flow and eventually occupies the entire pipe, becoming “fully developed”. The entrance of a pipe is an area of high-pressure loss, due to the boundary layer being at its minimum area.

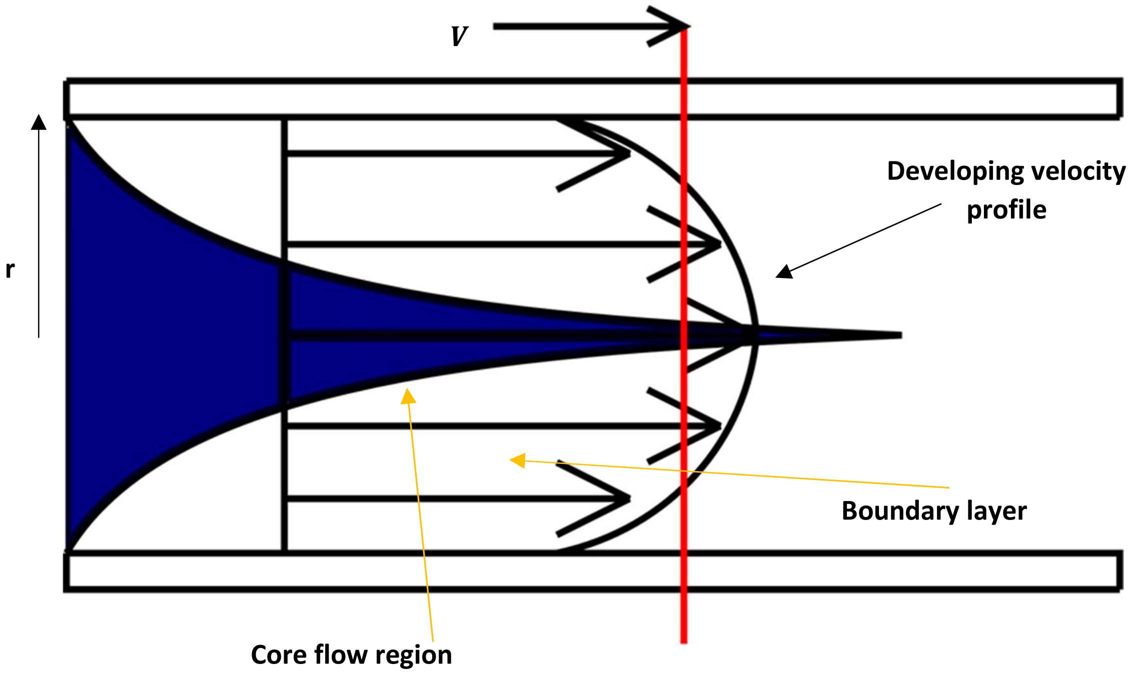

Figure 4.1: Developing velocity profile within a pipe for a low Reynolds number flow, the core flow region (coloured in blue) decreases with flow direction, while the boundary layer (coloured in white) increases till it occupies the entire pipe. The average velocity of flow is represented by V and r is the radius of the pipe.

Flow regimes within a pipe are characterised primarily as two types of flow: Laminar and Turbulent flow. Both describe the relative motion of fluid streamlines within them and are dependent upon several factors, such as: velocity, geometry, density and the viscosity of the fluid used (Reynolds 1883). These are reflected in the Reynolds Number, a dimensionless number that expresses the ratio of inertial to viscous forces in a fluid. It is denoted by the equation:

$$Re = \frac{\rho V D}{\mu} \tag{4.1}$$

where Re is the Reynolds number, ρ is the density of the fluid ($\mathrm{kg/m^3}$), V is the average velocity of the flow ($\mathrm{m/s}$), D is the diameter of the pipe (m) and μ is the viscosity of the fluid ($\mathrm{Pa\ s}$).

4.2.1 Laminar flow

Flow is considered to be laminar for an incompressible fluid in a circular pipe for $\mathrm{Re} \leq 2300$, where the viscous forces are sufficient to keep fluid particle motion restricted to highly ordered parallel streamlines (Figure 4.2). Laminar flow adopts a parabolic velocity profile when flow is fully developed, due to the effects of the no-slip condition as previously discussed. There is no radial motion and the velocity profile is unchanged along the flow direction.

4.2.2 Turbulent flow

Flow is considered to be turbulent for an incompressible fluid in a circular pipe for $\mathrm{Re} \geq 4000$, turbulent flow is characterized by chaotic motion with areas of swirling fluid, called eddies (Figure 4.3), present throughout. Unlike laminar flow, there is radial motion present in turbulent flow, with eddies transporting mass, momentum and energy across streamlines. This increased mixing has a higher degree of friction associated with it, leading to turbulent flow being defined by a flatter velocity profile.

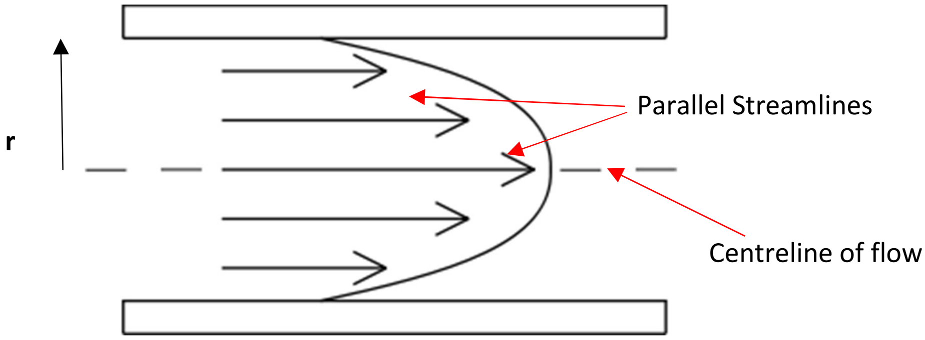

Figure 4.2: The characteristic laminar flow parabolic velocity profile for fully developed flow in a pipe of radius r. The flow pattern is highly organized, with fluid particles moving parallel to one another in streamlines. The parabolic profile develops due to the effects of the no-slip condition, where fluid particles at the pipe wall are at rest.

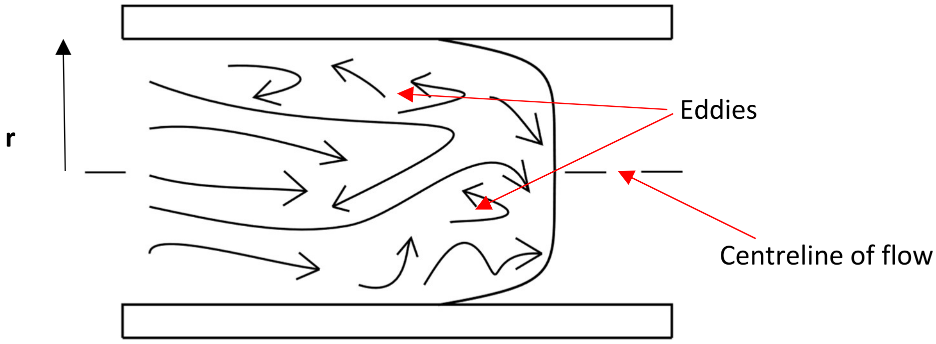

Figure 4.3: Visual representation of chaotic motion of fluid particles in fully developed turbulent flow in a pipe of radius r. Eddies within the fluid body distribute mass, momentum and energy, increasing friction effects and causing a flatter velocity profile to develop.

4.3 Major pressure losses

For any fluid flowing through a pipe there is an associated pressure drop due to frictional effects. Due to these losses, the apparent pressure head for flow within the experimental system differs from the actual pressure determining flow. Calculating the actual pressure head is important as it is this pressure that drives flux, which this study later seeks to relate to fountain height. Several pre-existing equations are available to assist in this process.

4.3.1 Darcy-Weisbach equation

A general equation exists for calculating the major pressure losses along a pipe system that is suitable for either laminar or turbulent flow (Weisbach 1845), it is expressed by the equation:

$$\Delta P = f\frac{L\rho V^2}{2D} \qquad 4.2$$

where ΔP is the pressure (Pa), f is the darcy friction factor, a dimensionless quantity for friction along a pipe. In instances of laminar flow, the value of the friction factor can be found by using the equation:

$$f = \frac{64}{Re} \qquad 4.3$$

For cases dealing with turbulent flow, a different equation is required to calculate the friction factor (See section 4.3.3).

4.3.2 Hagen-Poiseuille equation

Alternatively, the major pressure loss in a system can be calculated using the Hagen-Poiseuille equation. This relationship exists for a cylindrical pipe (figure 4.4) and is only valid in instances of laminar flow (Poiseuille 1840), it is given by the equation:

$$Q = \frac{\Delta P \pi r^4}{8\mu L}. \qquad 4.4$$

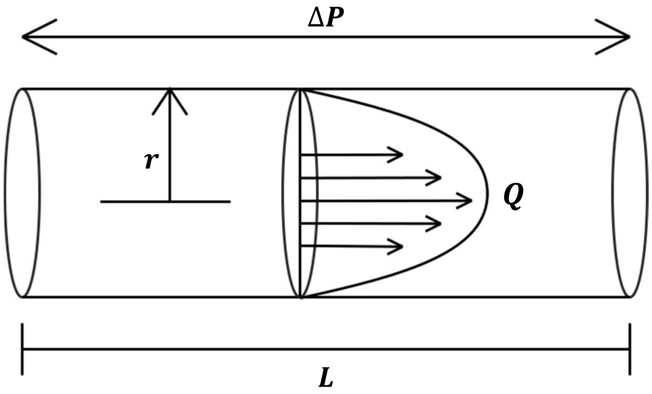

Figure 4.4: Laminar flow for an incompressible fluid within an impermeable, inelastic cylindrical pipe, demonstrating Hagen-Poiseulle law.

4.3.3 Colebrook equation:

While a simple solution for the friction factor exists for flow within the laminar regime, no such relationship exists for flow within the turbulent regime. Instead, the friction factor is determined by using the Colebrook equation (Colebrook 1939) which is given as:

$$\frac{1}{\sqrt{f}} = -2.0\log\left(\frac{\frac{\varepsilon}{D}}{3.7} + \frac{2.51}{Re\sqrt{f}}\right) \qquad 4.5$$

where ε is the roughness of a pipe (m). This can be visually represented as the Moody chart (figure 4.5), which plots the friction factor as a function of the Reynolds number and $\frac{\varepsilon}{D}$.

4.3.4 Haaland equation:

While the Colebrook equation requires an iterative solution to determine the friction factor, an approximate solution exists for friction factor valid to within 2 percent of values given by those of the Colebrook equation (Haaland 1981).

The Haaland equation for friction factor is defined as:

$$\frac{1}{\sqrt{f}} \cong -1.8log\left[\frac{6.9}{Re}+\left(\frac{\frac{\varepsilon}{D}}{3.7}\right)^{1.11}\right]. \qquad 4.6$$

By using this equation to calculate the friction factor, then substituting into the Darcy-Weisbach equation, it allows for major pressure losses to be calculated for turbulent flows. Two types of pipes were used in experiments, which were made of plastic and steel, these have respective roughness's of 0 and $0.045x10^{-4}$m (values taken from page 350, Cengel, Y.A., and Cimbala, J.M., Fluid Mechanics: Fundamentals and Applications. 3rd ed. Mc Graw Hill India: 2014).

4.4 Minor pressure losses

Aside from the major pressure losses across a system, minor losses also occur due to the presence of plumbing fixtures within the pipe network that disturb flow. Individual minor losses can generally be expressed by following equation:

$$h_L = K_L\frac{V^2}{2g} \qquad 4.7$$

where h_L is the head loss (m) due to the presence of the component, g is the acceleration due to gravity $(\mathrm{m/s^2})$ and K_L is the loss coefficient, determined experimentally by manufacturers. Losses tend to be expressed in head loss for convenience, they can be converted to pressure loss like so:

$$\Delta P_{minor} = \rho g h_L \qquad 4.8$$

where ΔP_{minor} is the minor pressure loss (Pa). The total minor pressure losses for all components present within a system is the sum of all the minor pressure losses, such that:

$$\Delta P_{minor} = \sum \Delta P_1 + \Delta P_2 \ldots + \Delta P_n \qquad 4.9$$

where the subscripts each denote a separate component within the system.

There are two exceptions to experimentally determined loss coefficients, these are instead determined mathematically, they arise when a sudden contraction or a sudden expansion within a system is present.

The loss coefficient for a sudden expansion is calculated by following equation:

$$K_L = \left(1 - \frac{d^2}{D^2}\right)^2 \qquad 4.10$$

where d is the diameter (m) of the narrower pipe and D is the diameter (m) of the wider pipe. For sudden contractions the loss coefficient can be determined by using figure 4.6. The complete list of areas of minor loss within the experimental configuration used to produce this research are available in table 4.1.

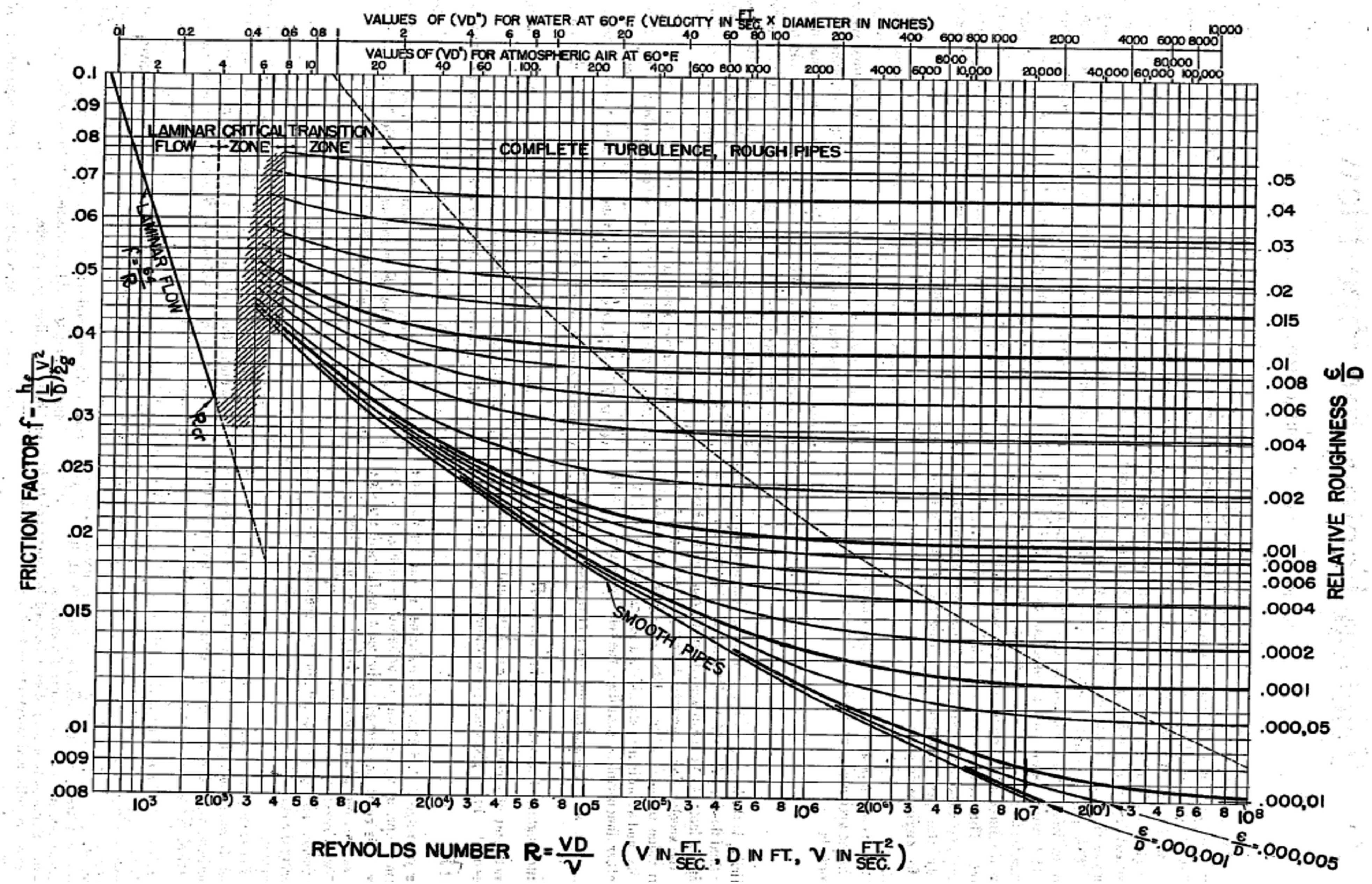

Figure 4.5: The relationship between the friction factor f, the Reynolds number, and roughness ε for fully developed pipe flow (Taken from figure 1, Moody 1944). It is a visual representation of the Colebrook Equation. While neater graphical forms exist, this relationship is still utilized in modern fluid dynamics.

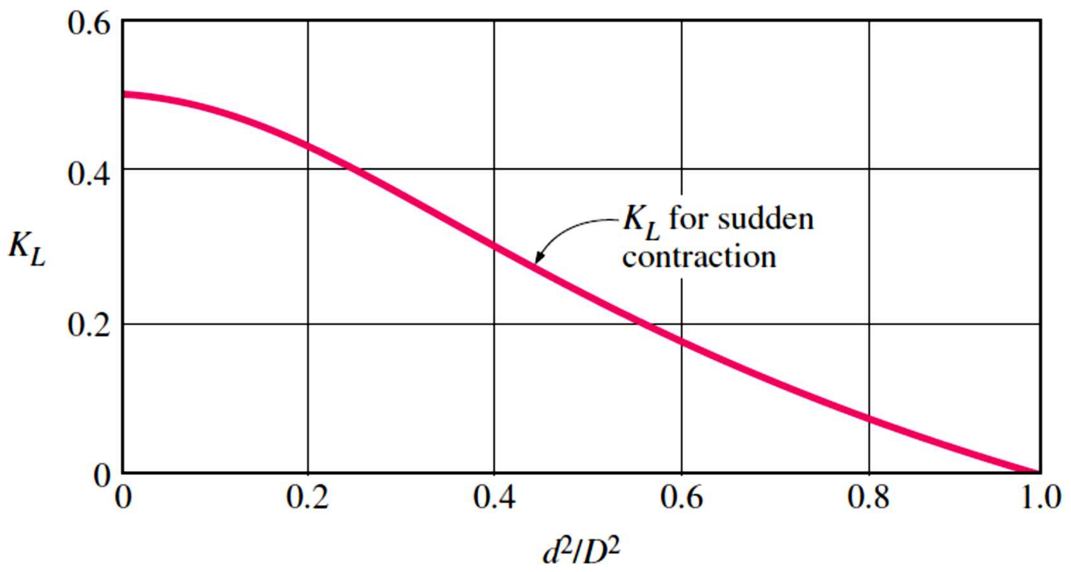

Figure 4.6: Chart for determining the loss coefficient for a sudden contraction within a pipe network (obtained from page 350, Cengel, Y.A., and Cimbala, J.M., Fluid Mechanics: Fundamentals and Applications. 3rd ed. Mc Graw Hill India: 2014.).

By summing all the individual minor losses as well the major pressure losses, the total pressure drop over the entirety of the experimental system can be found for, which can be expressed by the following general equation:

$$\Delta P_{total} = \Delta P_{major} + \Delta P_{minor} \tag{4.11}$$

where each subscript denotes the respective sums of the type of pressure loss experienced. For all experiments, calculated values for minor losses are sufficiently small when compared to the overall pressure head that they can be considered negligible.

4.5 Calculation of pressure losses

While equation 4.10 provides a general equation for determining pressure loss, the actual calculation is slightly more complex, due to the experimental system being comprised of two sections of pipe, each of a different diameter, length and material.

Component	Loss coefficient	Equation
Pipe inlet	0.5	$h_L = 0.5\frac{V^2}{2g}$
Open Ball valve	0.05	$h_L = 0.05\frac{V^2}{2g}$
$90°$ Threaded elbow	0.9	$h_L = 0.9\frac{V^2}{2g}$
Pipe exit	α	$h_L = \alpha\frac{V^2}{2g}$
Sudden expansion	See equation 4.10	$h_L = K_L\frac{V^2}{2g}$
Sudden contraction	See figure 4.6	$h_L = K_L\frac{V^2}{2g}$

Table 4.1: Complete list of minor loss causing components, with their respective loss coefficients and equations. For a pipe exit, loss coefficient is dependent upon whether the flow is turbulent or laminar, $\alpha = 2$ for laminar flow and $\alpha = 1$ for turbulent flow.

These calculations express flux as a function of pressure head and losses within the pipe, allowing the comparison of measured and modelled flow rates. This method allows any potential erroneous experimental setups to be identified, providing a legitimate reason to omit them from further analysis.

Taking the relationship for the continuity equation (Q=VA=constant), the velocity of flow within a pipe can be expressed as:

$$V = \frac{4Q}{\pi D^2}. \tag{4.12}$$

Substituting equation 4.12 into equation 4.2 and simplifying then gives the expression:

$$Q^2 = \frac{\pi^2 D^5 \Delta P}{8 f \rho L}. \tag{4.13}$$

Equation 4.13 gives a general expression for the volumetric flux for a pipe in terms of the respective losses within a pipe. Taking the definition of the continuity equation, that the volumetric flux within a pipe is constant, then the volumetric flux in both sections of pipe are equal to one another, such that $\mathrm{Q}_1 = \mathrm{Q}_2$. This can be expressed as:

$$\frac{\pi^2 D_1^5 \Delta P_1}{8 f_1 \rho L_1} = \frac{\pi^2 D_2^5 \Delta P_2}{8 f_2 \rho L_2} \tag{4.14}$$

with the subscripts 1 and 2 denoting the larger and smaller pipes respectively. Rearranging these equations and substituting (for $\Delta P_2 = \Delta P - \Delta P_1$):

$$\Delta P_1 = \frac{f_1 L_1 D_2^5 \Delta P}{f_2 L_2 D_1^5 + f_1 L_1 D_2^5}. \tag{4.15}$$

Substituting this equation into 4.13 then gives:

$$Q^2 = \frac{\pi^2 D_1^5 D_2^5}{8\rho} \frac{\Delta P}{f_2 L_2 D_1^5 + f_1 L_1 D_2^5}. \tag{4.16}$$

Equation 4.16 allows for the calculation of flux as a function of pressure head and losses within both the small and large pipe.

4.6 Rheology

Having discussed the scaling of materials, experimental parameters and pipe flow equations, it is now necessary to examine the appropriate viscosity required to emulate the laminar flow regime during experiments. As previously addressed in chapter 2, scaling material properties is important when analysing natural processes in the laboratory. In chapter 2 the range of Reynolds numbers encountered for natural lava fountains was approximated to be 0.275-275000. Water and syrup solutions were chosen as suitable fluids to capture the turbulent and laminar regimes respectively. The appropriate solution viscosity was determined by creating a system of equations in an excel spreadsheet to generate model fluxes and their corresponding Reynolds numbers for various experimental conditions. Experimentation with the configured system of equations revealed a viscosity of 0.1 Pa s as the most appropriate value, spanning a wide range of Reynolds numbers for the laminar flow regime.

4.6.1 Golden syrup

As previously mentioned in chapter 2, the viscosity of golden syrup can be varied by diluting it with water. Having identified a suitable viscosity for experiments, the next task is to determine the required amount of water to add to achieve the required viscosity. Drawing from a previous study by Jones 2018, which examined how golden syrup viscosity varies for water dilutions (Fig 4.7), a solution of 20% weight percent of water (which has a viscosity of 0.8654 Pas) was identified as starting point from which to develop an appropriate solution. Successive iterations found that 22% weight percent produced the desired viscosity of 0.1 Pas.

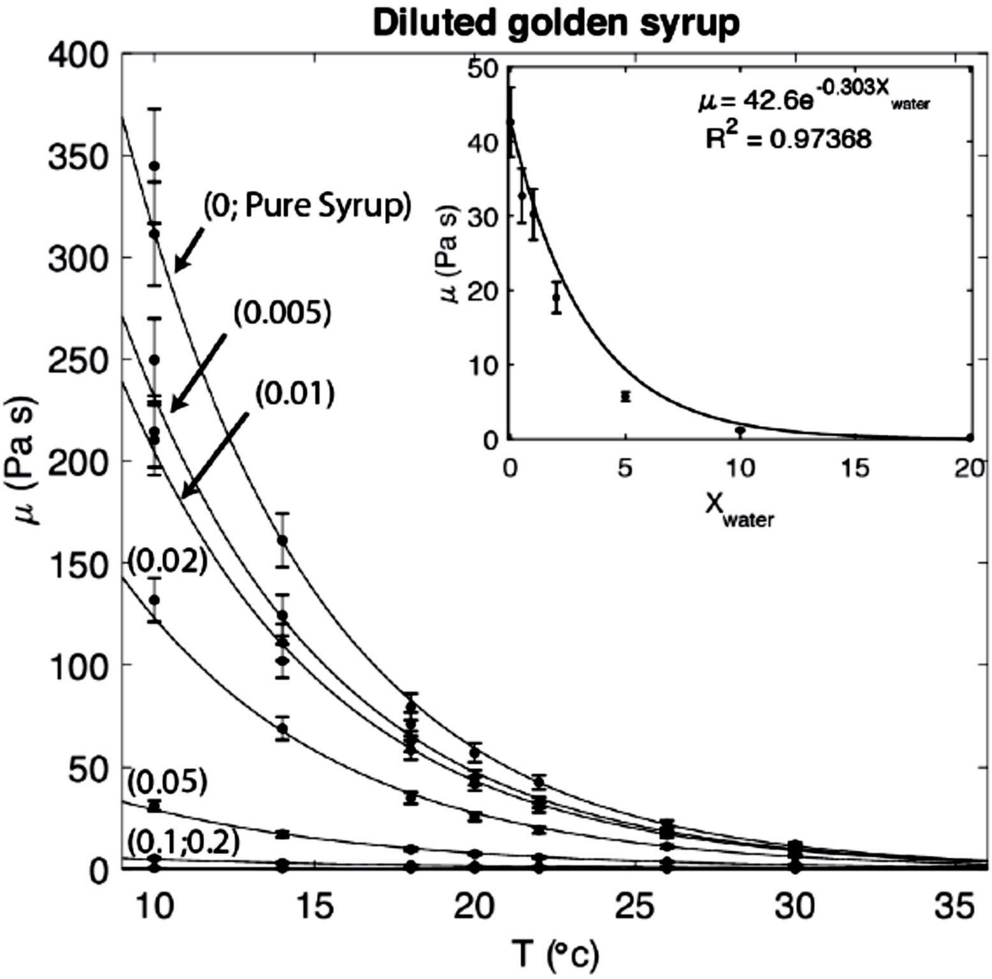

Figure 4.7: Viscosity of golden syrup and dilutions as a function of temperature. Graphical inset details golden syrup as a function of water dilution at a constant temperature of 22°C. (Taken from figure 4.3, page 78, Jones 2018).

Having determined the correction weight percentage of water to produce the required the solution, it was then necessary to determine the density of this solution. The previously mention study by Jones 2018 also developed a general equation for determined solution density as a function of temperature and weight percentage of water (Fig 4.8). This equation states that:

$$\rho = -0.58724t - 5.3542X_{water} + 1450.5 \qquad 4.17$$

Where t is temperature (℃) and X_{water} is the percentage of water dilution. Given that the density of this solution contains temperature as a variable, it is then necessary to examine the dependency of solution viscosity upon temperature.

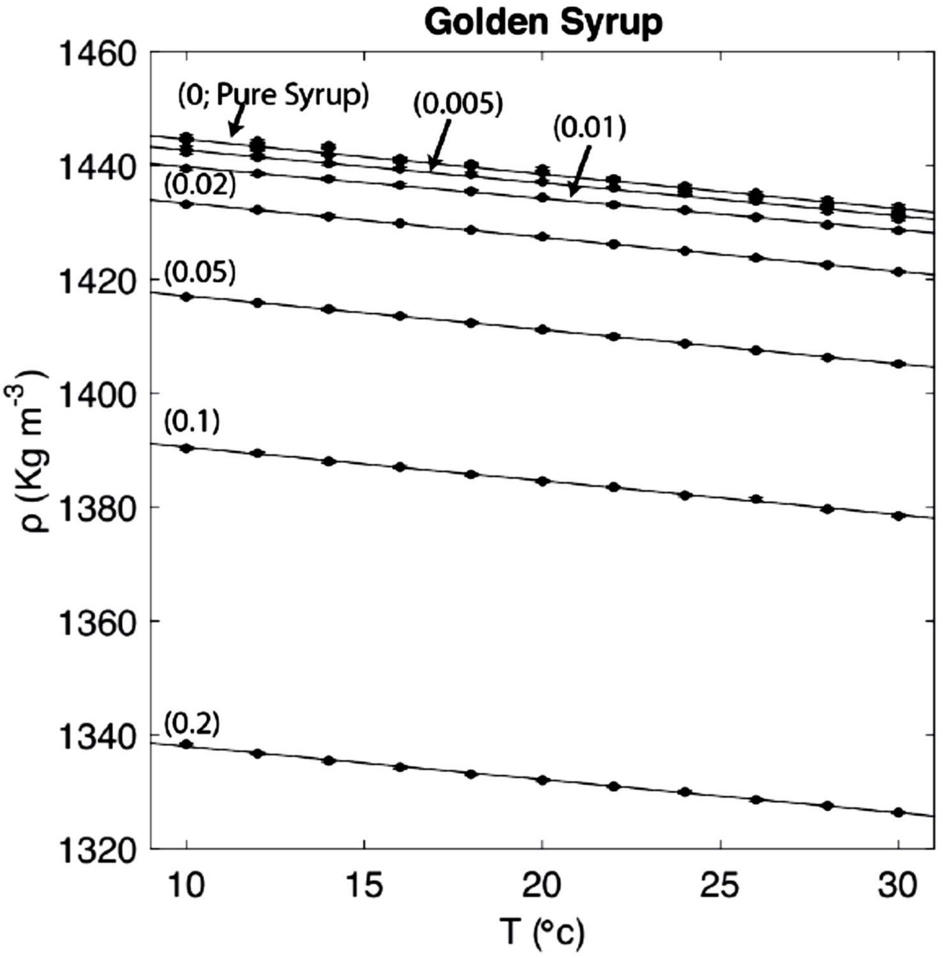

Figure 4.8: Density of golden syrup and dilutions as a function of temperature (Taken from figure 4.7, page 83, Jones 2018).

When using water as an experimental fluid, variation in viscosity as a function of temperature can be considered negligible. However, pure golden syrup viscosity is a function of temperature (Figure 4.9).

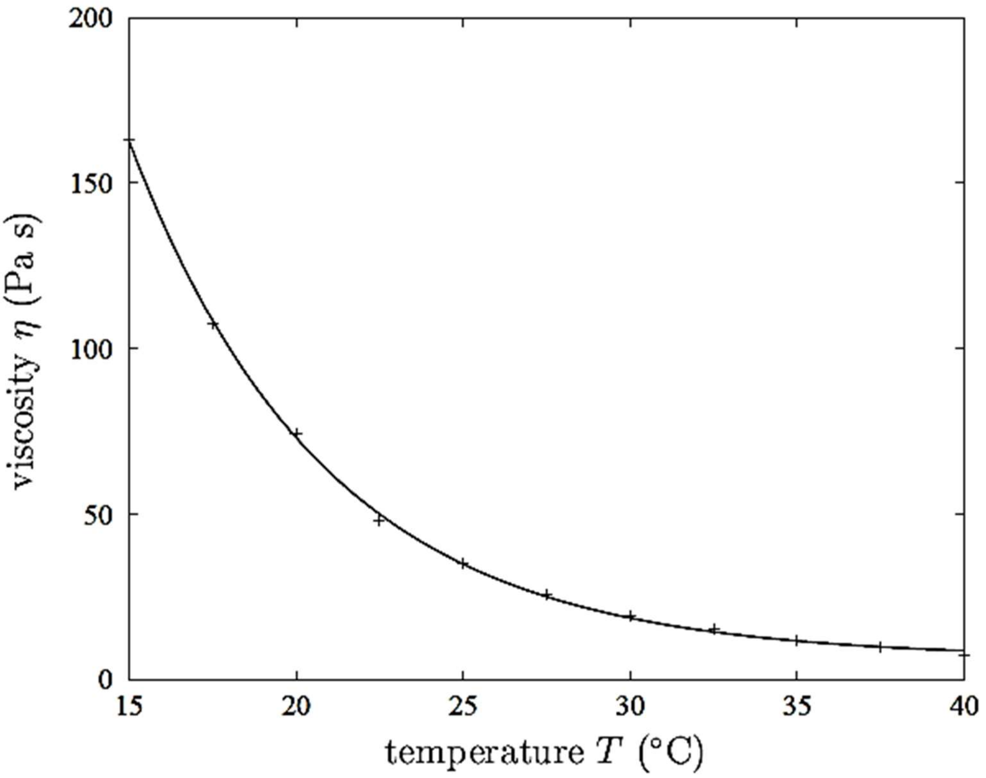

Figure 4.9: Viscosity of pure golden syrup as a function of temperature (Taken from figure 4.3, page 64, Llewellin 2002).

4.6.2 Rheometry

Accounting for the dependency of viscosity on temperature for golden syrup requires combining documentation of laboratory temperatures during experiments and rheometry of the manufactured solution. Samples were taken daily during use for analysis, the results of which are presented in figures 4.10-4.13.

Solution viscosity was determined using a Haake rotational rheometer with a temperature control function. The rheometer functions by applying a shear stress (Pa) and measuring the corresponding strain rate (s^{-1}) through a series of sensors. It does this in a series of incremental steps, with 30 second pauses between each measurement. The associated computer software allows tight control over all input values during the course of analysis.

The syrup dilutions were loaded into a container embedded into the rheometer stage, then a motorized sensor was lowered into the container, upon which a cap was placed to create an airtight seal. After loading a sample, it was allowed to rest for 6 minutes to reach the selected temperature before starting analysis. Temperatures selected for analysis were: 21°C, 22°C 23°C and 24°C, which is the temperature range encountered within the laboratory.

The range of applied stresses were between 0 and 100 Pa in a series of 15 incremental steps, after completing this series, the rheometer would then repeat these measurements in reverse order. For all tested temperature values, stress was proportional to strain rate, indicating a Newtonian rheology.

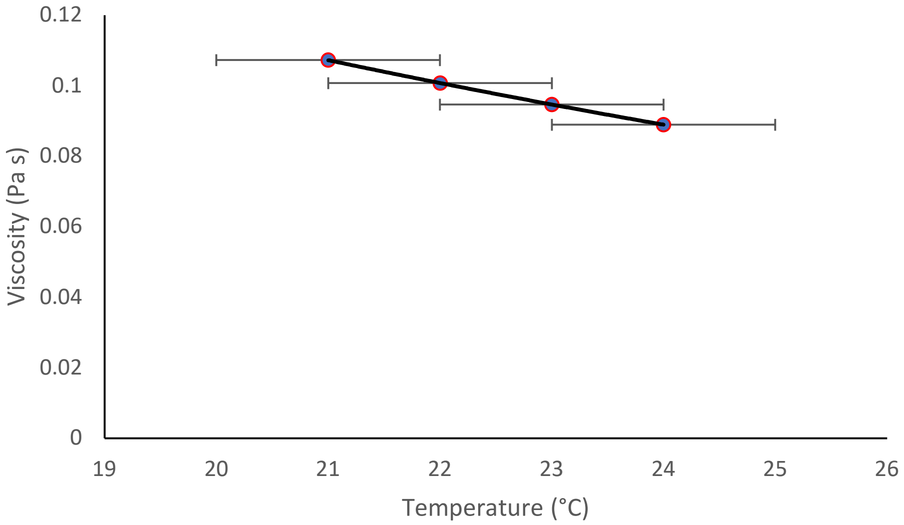

Figure 4.10: Viscosity of golden syrup as a function of temperature, sampled on the 15/8/18. Best fit line is of the form $\mu = 0.3975e^{-0.062t}$, $(\mathrm{R}^2 = 1)$.

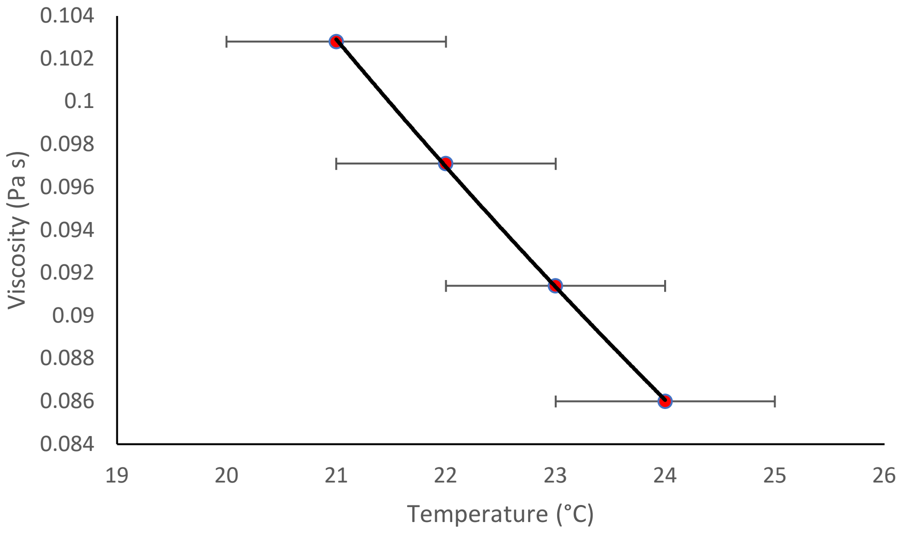

Figure 4.11: Viscosity of golden syrup as a function of temperature, sampled on the 16/8/18. Best fit line is of the form $\mu = 0.3596e^{-0.06t}$, $(\mathrm{R}^2 = 0.9998)$.

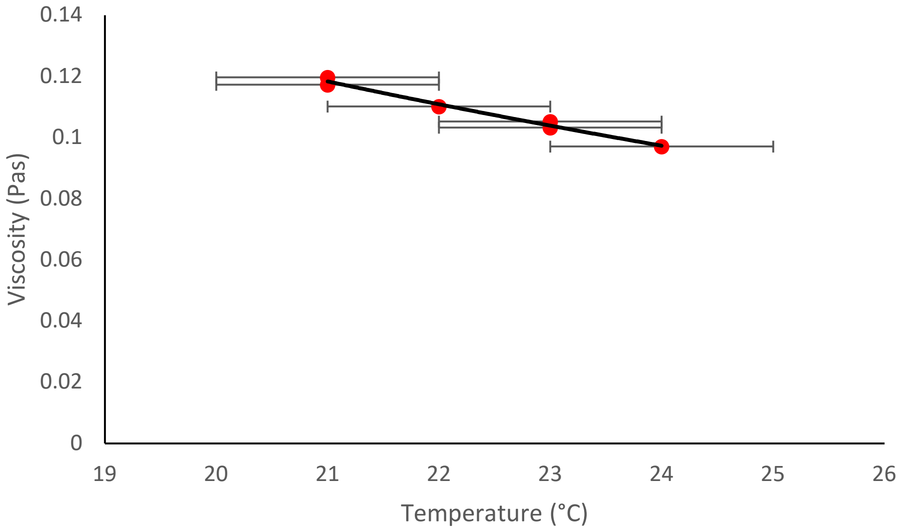

Figure 4.12: Viscosity of golden syrup as a function of temperature, sampled on the 23/8/18. Best fit line is of the form $\mu = 0.4653e^{-0.065t}$, $(\mathrm{R}^2 = 0.9853)$.

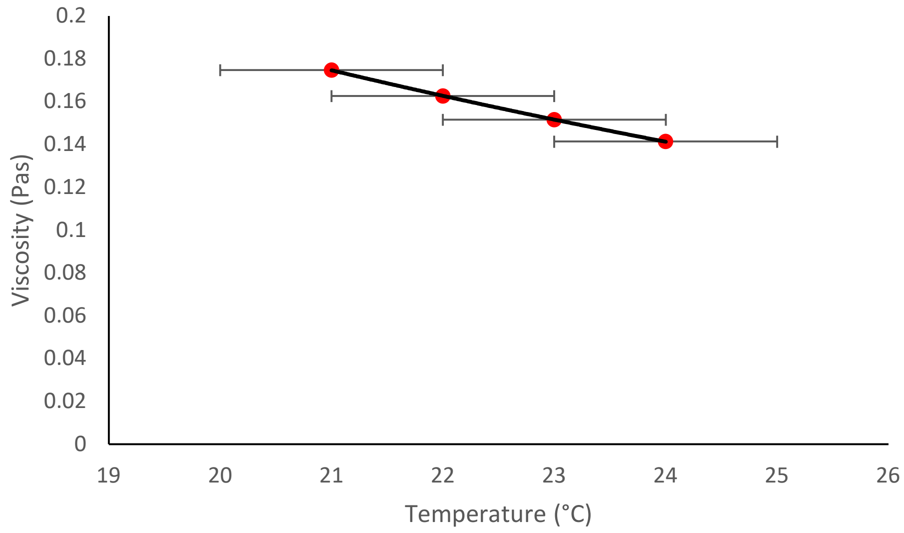

Figure 4.13: Viscosity of golden syrup as a function of temperature, sampled on the 28/8/18. Best fit line is of the form $\mu = 0.7711e^{-0.071t}$, $(\mathrm{R}^2 = 1)$.

5. Results and Analysis

5.1 Introduction

This chapter details the quantitative dataset collected using the previously described methodology in chapter 3. A qualitative description of fountain behaviour is presented, examining how changing experimental setups produce visible changes in fountain behaviour.

The collected dataset is then used to quantitatively analyse the variation in fountain behaviours with changing experimental setup. A modelled volumetric flux is calculated using the equations pipe flow equations previously discussed in chapter 4. These modelled values are compared to measured values for volumetric fluxes during experiments as a method of identifying outlier values. The effectiveness of the ballistic equation is evaluated as a means of determining fountain height with increasing ponding depth. The dimensionless groups previously derived in chapter 2 are then re-introduced, allowing a dimensionless relationship between dimensionless fountain height and dimensionless ponding depth to be identified.

5.2 Qualitative description

Visual observations during the course of experimentation allow for the inference of behavioural trends in collected data. A common trend was observed at the beginning of experiment, where produced fountains rapidly reached an initial maximum height, before undergoing a slight height reduction. This is interpreted to be due to the interaction between up-flowing and down-flowing elements. Fountains then achieved steady state behaviour (with some minor fluctuations) at this new height till flow ceased. Changing experimental conditions; ponding depth z (m), pipe diameter D (m), pressure head Δl (m) and fluid viscosity μ (Pa s), produced noticeable changes in fountain behaviour such as greater fountain heights, reductions in fountain height or increased lateral dispersion.

5.2.1 Water

Fountains produced using water achieved greater heights with increasing pressure head (Fig 5.1). Changing pipe diameter had no effect on un-ponded fountain heights for 0.75 and 1.75 m pressure heads, while decreasing pipe diameter produced higher fountains for a 1 m pressure head (Fig 5.2). For a 0.25 m pressure head, increasing pipe diameter corresponded with an increase in fountain height. Fountain height noticeably decreased as ponding depth increased, with fountains generated by narrower pipes experiencing a greater reduction in height than wider pipes (Fig 5.3).

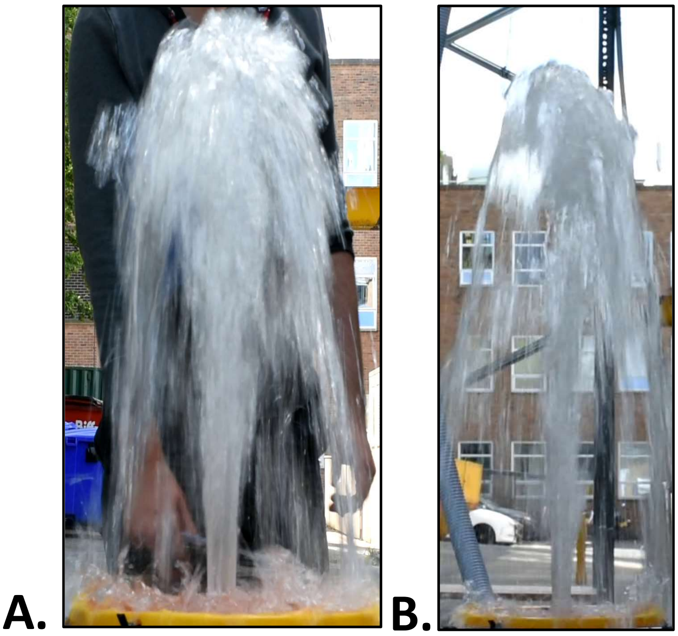

Figure 5.1: Two un-ponded fountains produced using water for a pipe of $D = 0.03$ m at two different pressure heads. A) A 0.49 m fountain produced at $\Delta l = 1$ m B) A 0.94 m fountain produced at $\Delta l = 1.75$ m

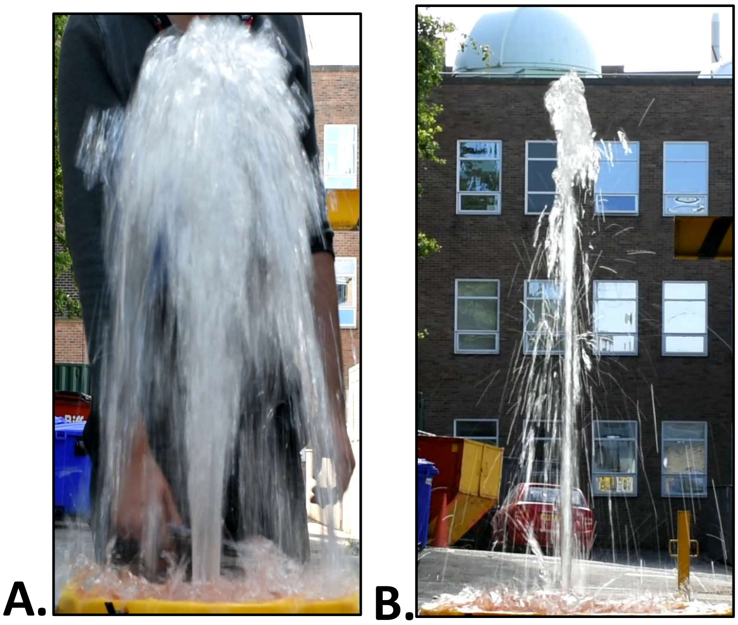

Figure 5.2: Two un-ponded fountains produced using water at $\Delta l = 1$ for two different pipe diameters. A) A 0.49 m fountain produced using a $D = 0.03$ pipe B) A 0.58 m fountain produced using a $D = 0.01$ m pipe.

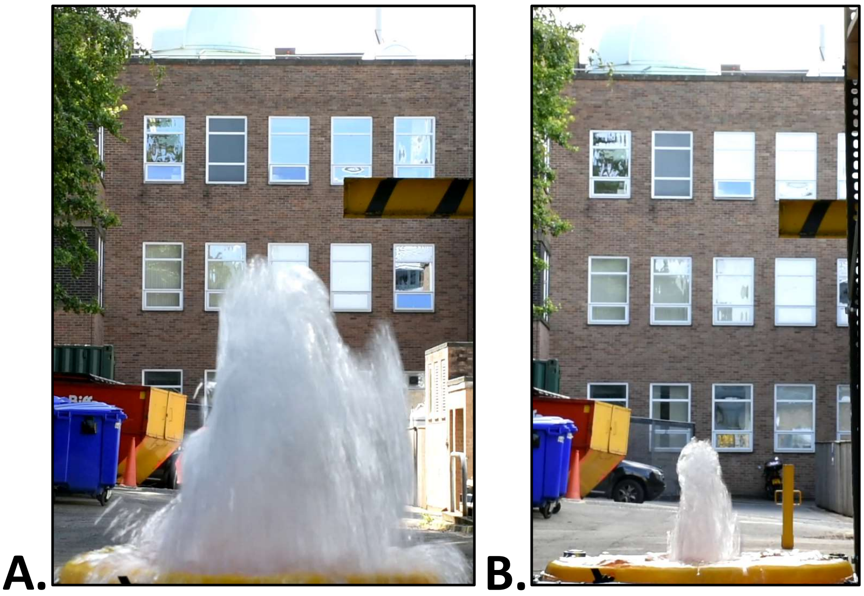

Figure 5.3: Two fountains produced using water for at $z = 0.08$ m at $\Delta l = 1$ for two different pipe diameters. A) A 0.3 m fountain produced using a $D = 0.03$ m pipe B) A 0.16 m fountain produced using a $D = 0.03$ m pipe.

5.2.2 Syrup solution

Fountains produced using a syrup solution also achieved greater heights with increasing pressure heads (Fig 5.4). Using larger pipe diameters produced greater fountain heights (Fig 5.5). Increasing ponding depth reduced fountain height as previously observed with water, with fountains generated by narrower pipes experiencing a greater reduction in height (Fig 5.6). In comparison to water, the produced fountains had overall lower heights when compared at identical conditions.

Figure 5.4: Two un-ponded fountains produced using a syrup solution for a pipe of $D = 0.03$ m at two different pressure heads. A) A 0.3 m fountain produced at $\Delta l = 1$ m B) A 0.6 m fountain produced at $\Delta l = 1.75$ m

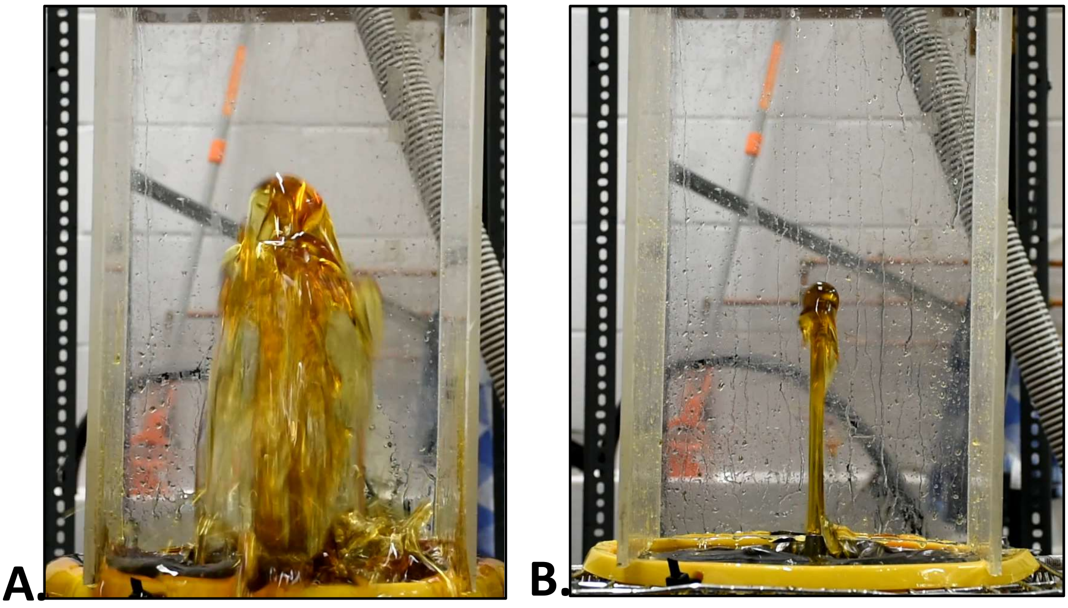

Figure 5.5: Two un-ponded fountains produced using a syrup solution at $\Delta l = 1$ for two different pipe diameters. A) 0.3 m fountain produced using a $D = 0.03$ pipe B) A 0.19 m fountain produced using a $D = 0.01$ m pipe

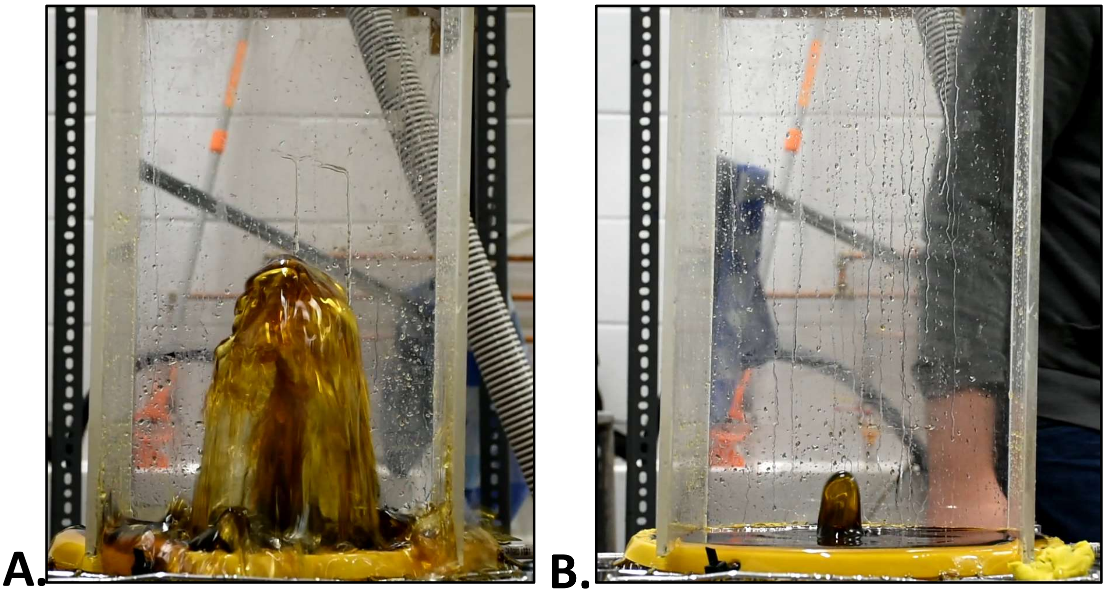

Figure 5.6: Two fountains produced using a syrup solution at $z = 0.08$ at $\Delta l = 1$ for two different pipe diameters. A) 0.21 m fountain produced using a $D = 0.03$ m pipe B) A 0.05 m fountain produced using a $D = 0.01$ m pipe.

5.2.3 Lateral dispersion

When increasing both pressure head and ponding depth, higher pressure fountains underwent a more noticeable reduction in fountain height with increased ponding depth relative to that experienced by low pressure fountains. This greater reduction in fountain height was accompanied by increased lateral dispersion of fountains with increasing pressure head. The effects of this are illustrated in figures 5.7-5.10 for both water and syrup solution fountains. Higher pressure fountains underwent increased lateral dispersion with ponding depth in comparison to their low-pressure counterparts. The most pronounced occurrences of this lateral dispersion where observed when producing water fountains.

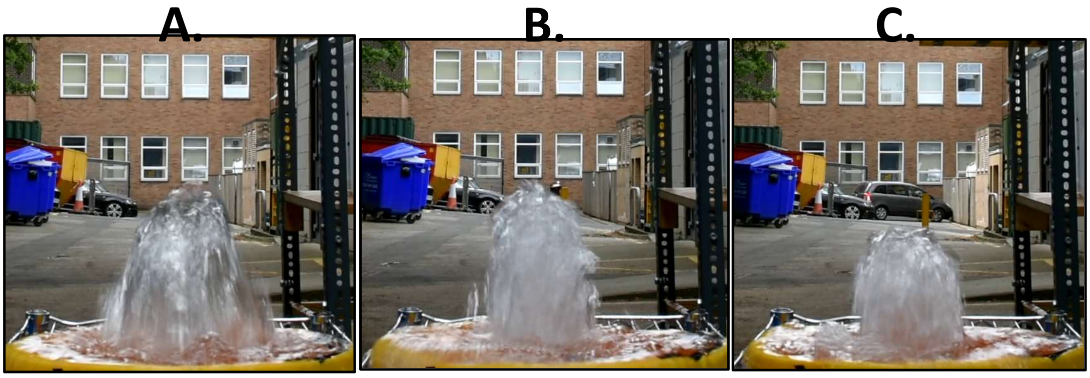

Figure 5.7: Three fountains produced using water at $\Delta l = 0.25$ m with a $D = 0.03$ m pipe at 3 different ponding depths. A) A 0.17 m fountain for $z = 0$ m B) A 0.13 m fountain for $z = 0.04$ m C) A 0.12 m fountain for $z = 0.08$ m.

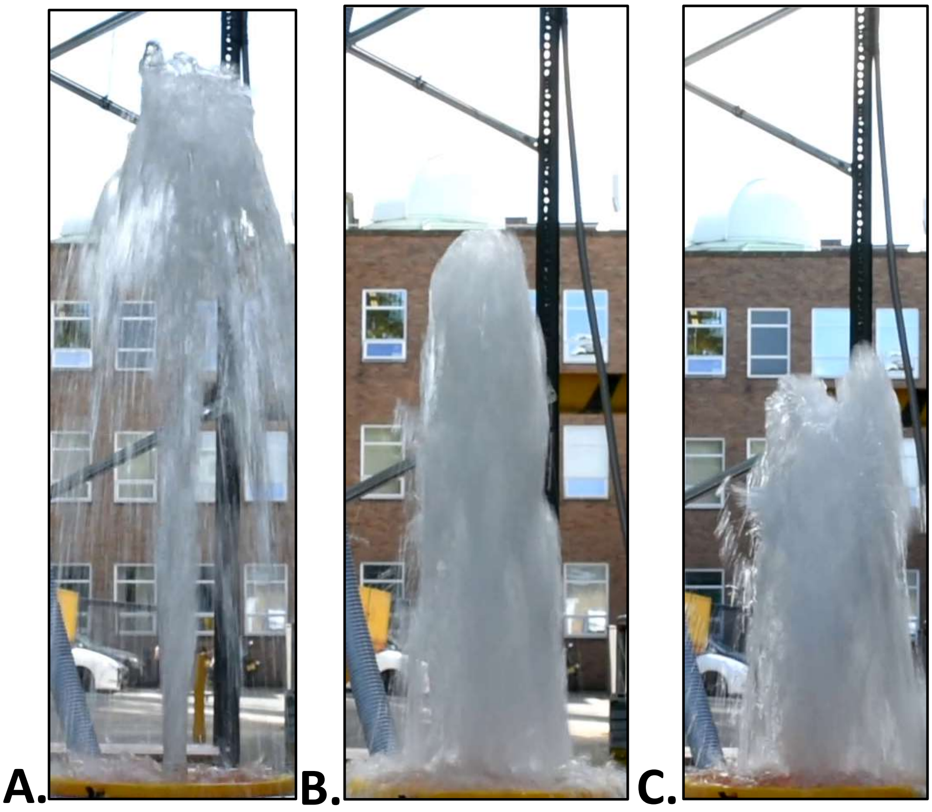

Figure 5.8: Three fountains produced using water at $\Delta l = 1.75$ m with a $D = 0.03$ m pipe at 3 different ponding depths. A) A 0.94 m fountain for $z = 0$ m B) A 0.70 m fountain for $z = 0.04$ m C) A 0.58 m fountain for $z = 0.08$ m.

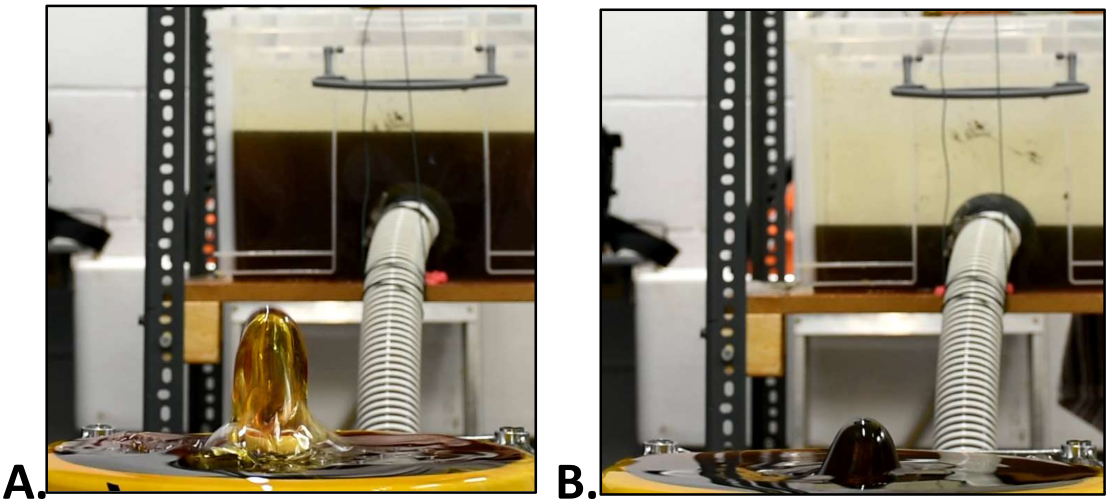

Figure 5.9: Two fountains produced using a syrup solution at $\Delta l = 0.25$ m with a $D = 0.03$ m pipe at 2 different ponding depths. A) A 0.09 m fountain for $z = 0$ m B) A 0.07 m fountain for $z = 0.08$ m.

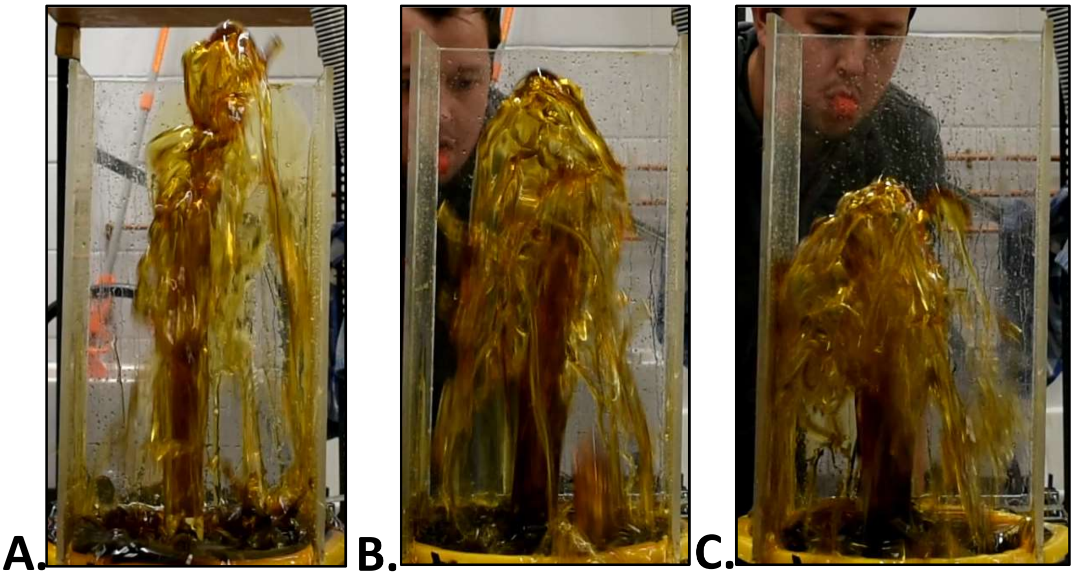

Figure 5.10: Three fountains produced using a syrup solution at $\Delta l = 1.75$ m with a $D = 0.03$ m pipe at 3 different ponding depths. A) A 0.57 m fountain for $z = 0$ m B) A 0.46 m fountain for $z = 0.04$ m C) A 0.38 m fountain for $z = 0.08$ m.

5.3 Quantitative analysis

A quantitative analysis allows the identification of numerical patterns present within a dataset that a qualitative description would not otherwise reveal. Quantitative measurements were performed using image processing software to determine fountain heights and variations in liquid volume within the tank during experiments. The mathematical equations previously presented in chapters 2, 3 & 4 allow the calculation of measured and modelled volumetric fluxes as well as the non dimensionalization of experimental parameters.

5.3.1 Modelled volumetric flux

While very precaution was taken during the experimental procedure, it is still important to inspect the collected dataset for outliers. Anomalous results within the collected data may be due to errors in experimental procedure or mistakes in data collection. The equations for pipe flow presented in chapter 4 are used to calculate model flux values, which are compared to measured flux values to help identify outliers in the collected dataset.

Modelled fluxes were calculated using an excel spreadsheet and a solver function add on. The spreadsheet was optimized to address that the experimental system consists of two pipes, each of different diameter, length and material. Initial values for modelled volumetric flux were computed using the equations for pipe flow detailed in chapter 4. The excel solver function was then applied to minimize the difference between measured and modelled values. The solver function accomplishes this by checking for solutions where the difference between measured and modelled values is at a minimum.

Measured volumetric flux for water is generally consistent with values expected from modelled fluxes (Fig 5.11), though for lower measured fluxes ($Q \leq 0.001\ \mathrm{m}^3/s$) there is a slight deviation between measured and modelled values for volumetric flux. Measured fluxes are slightly higher than anticipated by calculations, these discrepancies between measured and modelled values possibly indicate that the model is unable to fully reproduce all the pressure losses occurring with the pipe.

One particular noteworthy data point has a lower than expected flux compared to other experiments for identical experimental conditions. This data point has been highlighted in figure 5.11 and is considered to be due to errors in either experimental conditions or data collection, it is therefore omitted from further quantitative analysis.

Comparing modelled and measured fluxes by the factor for which they differ from one another (Fig 5.12) highlights a trend of increasing divergence between observed and modelled values with decreasing modelled flux. There 4 data points highlighted in figure 5.12 differ by approximately a factor of 6 when using this method, which is a significantly higher difference than other volumetric fluxes for identical experimental conditions. The values obtained for these 4 data points may have arisen either due to errors in experimental conditions or data collection. These data points are therefore excluded from further quantitative analysis, making it a total of 5 water experiments out of 211 that were discarded from further analysis.

Any remaining systemic divergence present within the remaining data points, where measured values are greater than modelled values, possess measured values that are consistent for identical conditions and therefore is considered valid for continued analysis. This divergence is inferred to indicate that the modelled flux is unable to fully reproduce all the pressure losses occurring within the pipe.

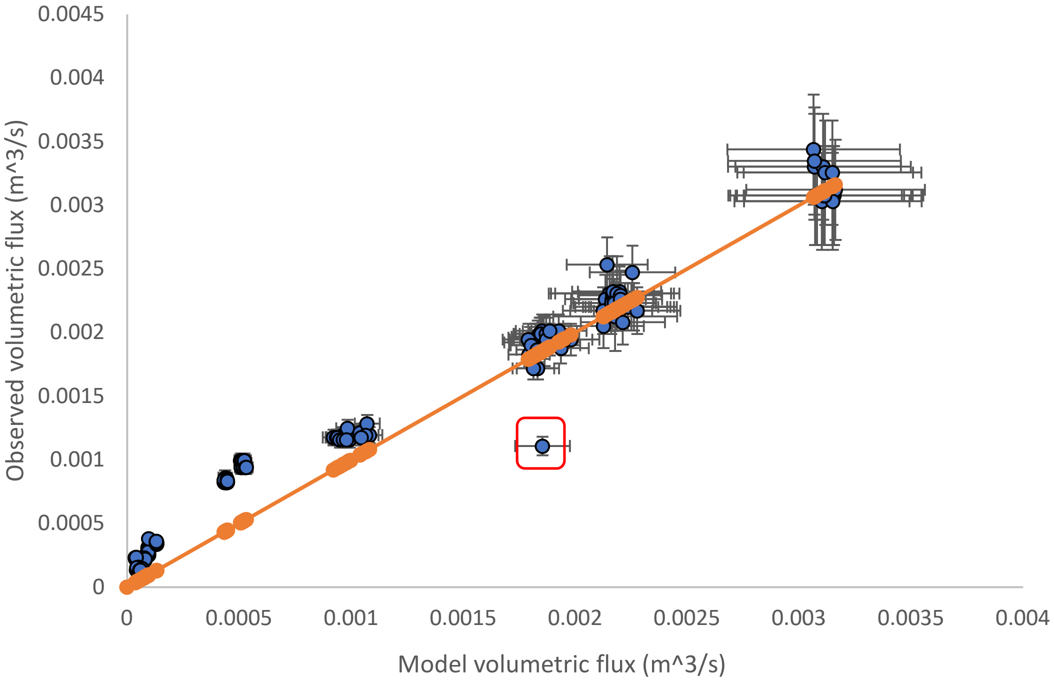

Figure 5.11: Comparison of measured and modelled volumetric fluxes (blue data points) for water. The orange line denotes the modelled volumetric flux ($\mathrm{R}^2 = 1$). Data point highlighted within red square diverges significantly from values for identical experimental conditions, indicating errors in either experimental conditions or data collection. Error bars denote propagated uncertainties due to assumed errors in measurements.

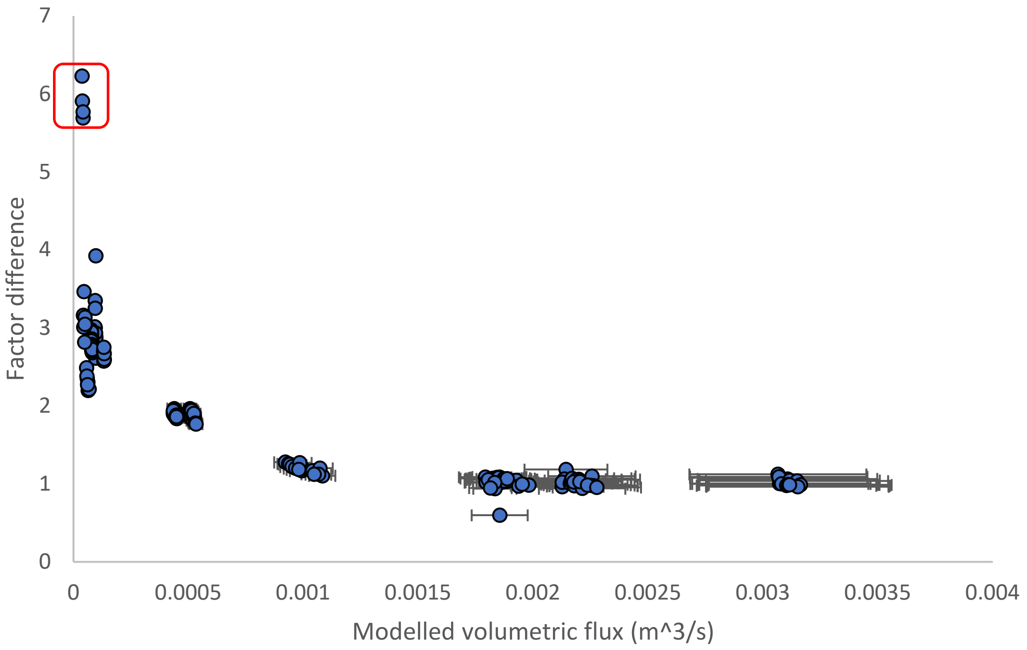

Figure 5.12: Factors by which measured and modelled volumetric fluxes for water differ from one another. Data points highlighted by red square indicate a significant divergence from expected fluxes, indicating possible errors in experimental conditions or data collection. Error bars denote propagated uncertainties due to assumed errors in measurements.

Comparing measured and modelled volumetric fluxes for the syrup solution displays a systemic divergence between measured and modelled values with increasing flux (Fig 5.13). In contrast to water experiments, the values by which measured and modelled fluxes differ reveals a large yet consistent divergence between measured and modelled values for the $D = 0.01$ m pipe, with measured values differing by a factor of 10 compared when compared to modelled values.

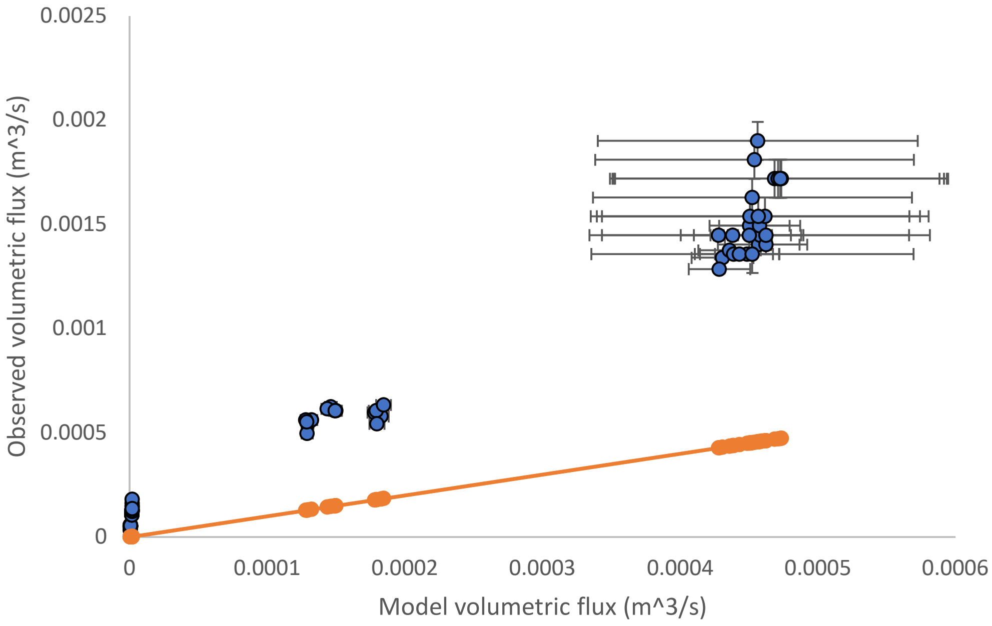

Figure 5.13: Comparison of measured (blue data points) and modelled volumetric fluxes for syrup solution experiments. The orange line denotes the modelled volumetric flux ($\mathrm{R}^2 = 1$). Error bars denote propagated uncertainties due to assumed errors in measurements.

As seen previously for modelled fluxes utilizing water, these discrepancies indicate that the modelled flux does not fully reproduce all the pressure losses occurring within the pipe. As the measured values obtained for syrup solution dataset are otherwise consistent when considering repeated experiments, it is considered valid for further quantitative analysis.

An interesting observation is for either laminar or turbulent flow, the most significant divergences between measured and observed fluxes occur for the lowest measured fluxes, again indicating that the modelled flux does not fully reproduce all the pressure losses occurring within the pipe.

5.3.2 Experimental data

Have identified and removed anomalous experiments from further analysis, fountain height is then plotted as a function of flow velocity for both water (Fig 5.14) and syrup solution (Fig 5.15) fountains. For both water and syrup the highest fountains generally possessed the greatest flow velocities. Fountains produced using water had overall both greater flow velocities and fountain heights.

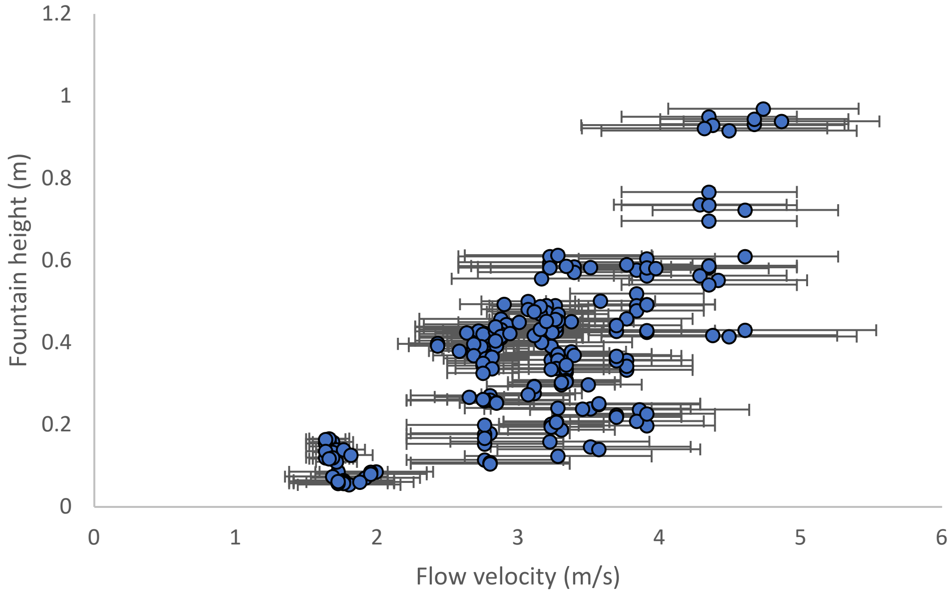

Figure 5.14: Variation in fountain height with flow velocity for water. Error bars denote propagated uncertainties due to assumed errors in measurements.

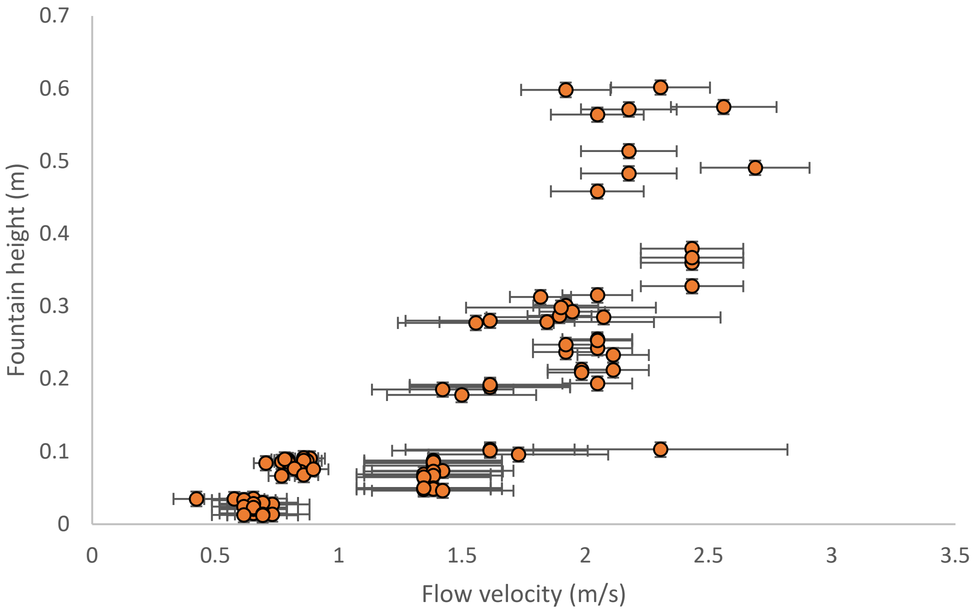

Figure 5.15: Variation in fountain height with flow velocity for syrup solution. Error bars denote propagated uncertainties due to assumed errors in measurements.

5.3.3 Ballistic equation

When modelling lava fountain behaviour, an important assumption is that the erupted mass is only considered to be comprised of pyroclasts (Wilson et al 1995). Although this assumption neglects the presence of gas within a natural lava fountain, it facilitates the use of the ballistic equation as a simplest method of calculating fountain height (Wilson et al 1995). This equation is expressed as:

$$h = \frac{V^2}{2g} \qquad 5.1$$

Where is V is the volumetric flux divided by the conduit cross sectional area (m/s), g is the acceleration due to gravity (m/s^2) and h is fountain height (m). This section seeks to examine how effective this assumption is for determining fountain heights and how its effectiveness might vary with changing ponding depth, pipe diameter, pressure head or fluid viscosity. Comparing measured un-ponded fountain heights for water to the ballistic equation (Fig 5.16), indicates that measured values are consistent with those expected from calculations. However, when comparing measured un-ponded syrup solution fountain heights to those of the ballistic equation (Fig 5.17), it is apparent there are discrepancies between measured and expected values.

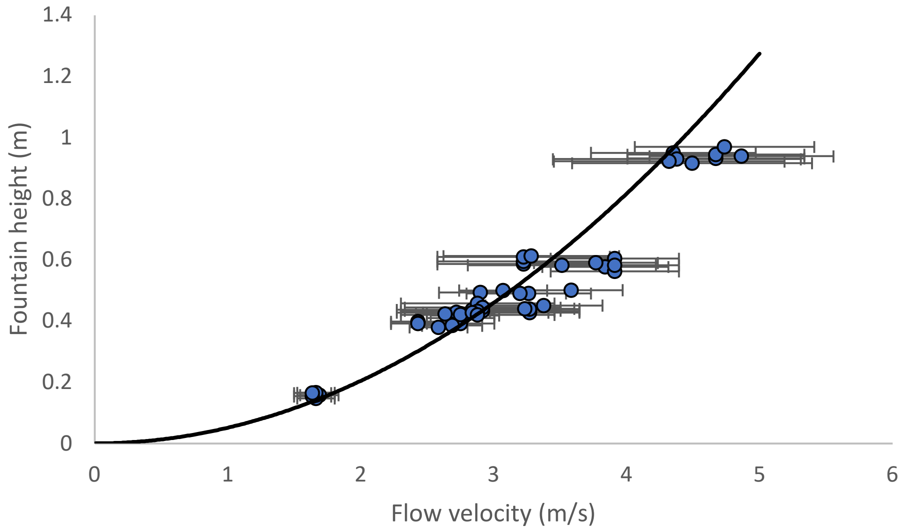

Figure 5.16: Modelled ballistic equation for a projectile (black line) compared to measured fountain height and flow velocity for water (blue data points). Error bars denote propagated uncertainties due to assumed errors in measurements

The explanation for this discrepancy is due to the parabolic velocity profile of laminar flow within a pipe (see chapter 4 for a full description of laminar flow). The flow velocity at the centreline of flow is twice that of the average flow velocity within the pipe. Therefore, when flow within a pipe has not adopted its full velocity profile, there is a significant portion of the fountain that has a velocity higher than the average velocity within the pipe. A correction factor can be applied to determine the corrected average flow velocity within the pipe for the syrup solution experiments. Examining the discrepancy between measured and anticipated values indicates that a correction factor of 1.37281 be applied to affected measured flow velocities. Plotting the corrected flow velocity against fountain height (Fig 5.18) indicates that measured values are consistent with those expected from calculations. When evaluating the remainder of the dataset in comparison to the ballistic equation (Fig 5.19), it is evident that there is a deviation between anticipated and measured fountain heights for identical flow velocities. This deviation is due to the effects of ponding upon fountain height.

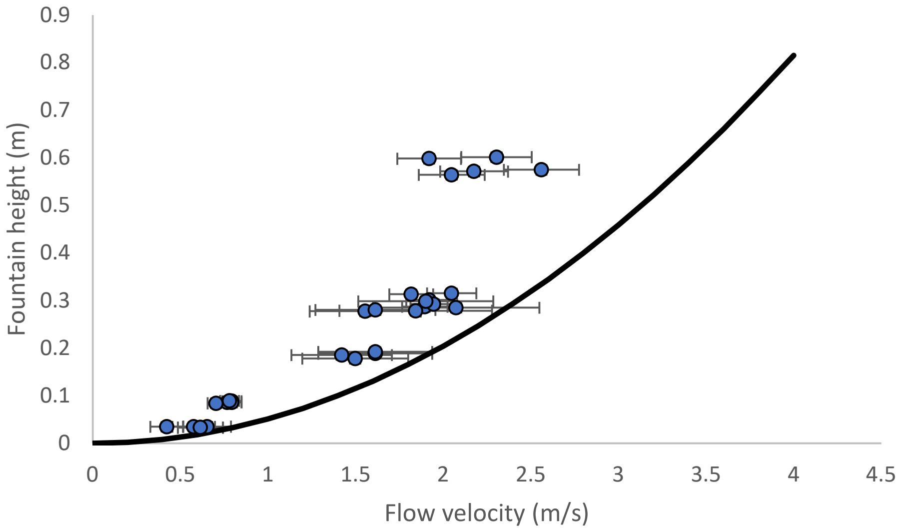

Figure 5.17: Modelled ballistic equation for a projectile (black line) compared to measured fountain height and flow velocity for syrup solution (blue data points). Error bars denote propagated uncertainties due to assumed errors in measurements.

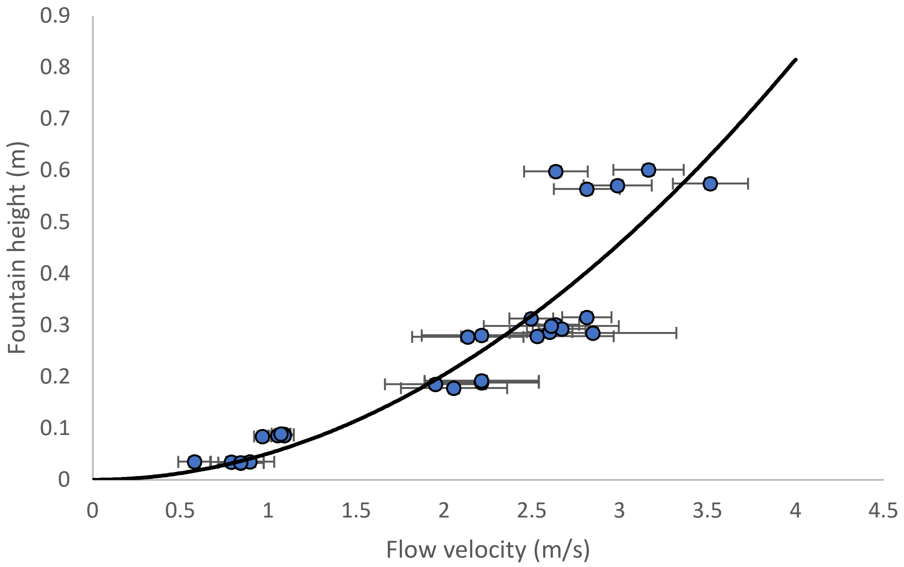

Figure 5.18: Modelled ballistic equation for a projectile (black line) compared to measured fountain height and corrected flow velocity for syrup solution (blue data points). Error bars denote propagated uncertainties due to assumed errors in measurements.

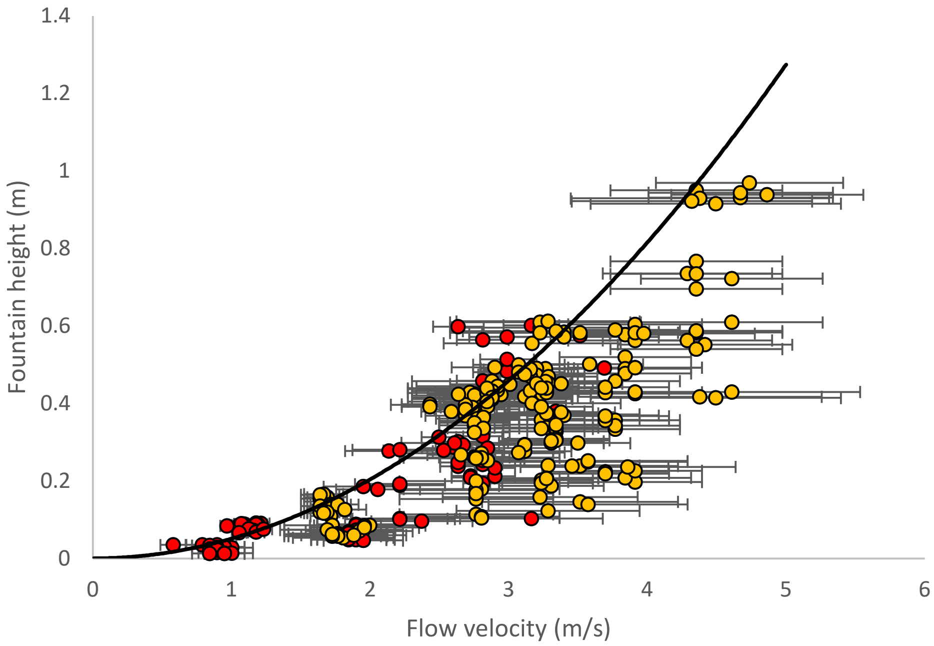

Figure 5.19: Modelled ballistic equation for a projectile (black line) compared to measured fountain height and corrected flow velocity for water (yellow data points) and syrup solution (red data points). Error bars denote propagated uncertainties due to assumed errors in measurements.

Indeed, characterizing the dataset according to ponding depth (Fig 5.20) shows that the ballistic equation is an accurate way of evaluating un-ponded fountains. However, with increased ponding depth measured values for height do not adhere to modelled values from the ballistic equation for identical flow velocities. The greatest divergences from expected values occur for the largest ponding depth of $z = 0.08$ m.

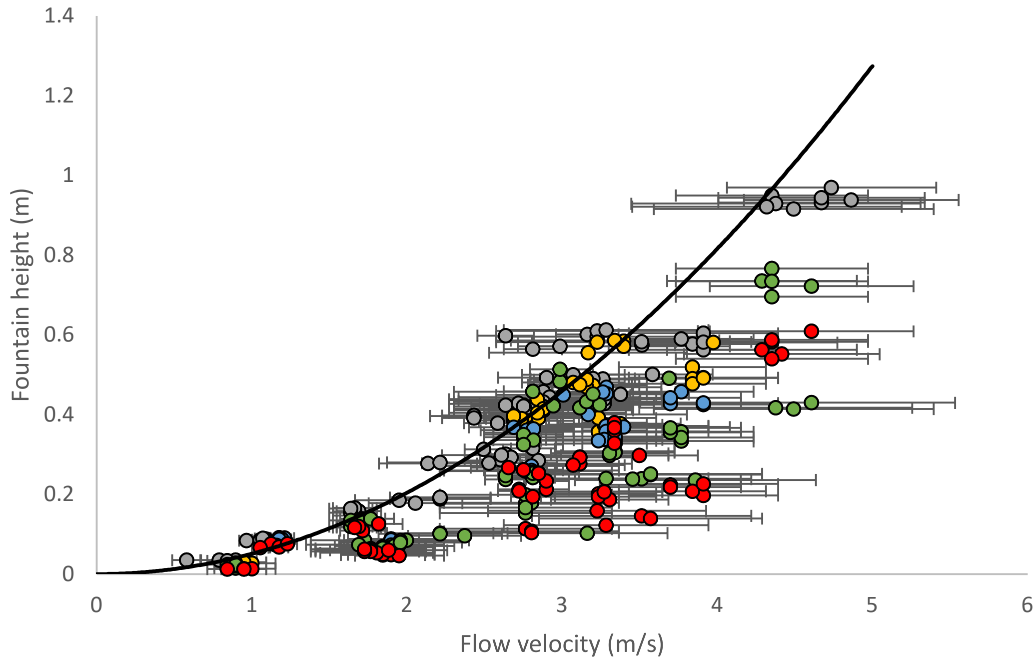

Figure 5.20: Ballistic equation for a projectile (black line) compared to measured fountain height and flow velocity for ponding depths of 0 (grey data points), 0.01 (yellow data points), 0.02 (blue data points), 0.04 (green data points) and 0.08 m (red data points). Error bars denote propagated uncertainties due to assumed errors in measurements.

When the dataset is characterized according to pipe diameter (Fig 5.21) also highlights visible trends. For water it is apparent that the highest fountains were produced using $D = 0.01$ and $D = 0.03$ m pipes, while the smallest fountains were generated using the $D = 0.01$ m pipe. For syrup the highest fountains were generated using the $D = 0.03$ m diameter pipe, while the smallest fountains were produced using the $D = 0.01$ m pipe. Comparing figures 5.20 and 5.21 clearly indicates that fountains produced using the $D = 0.03$ m pipe differ by lesser amounts than $D = 0.01$ and $D = 0.018$ m pipes for expected values of the ballistic equation. For instance, a water fountain generated using the $D = 0.03$ m pipe for $\Delta l = 1.75$ went from a height of approximately 1 m when un-ponded to a height of 0.7 m when subjected to $z = 0.04$ m. In comparison, for otherwise identical conditions, the same fountain went from a height of approximately 1 m when un-ponded to a height of 0.4 m when produced using the $D = 0.01$ m pipe.

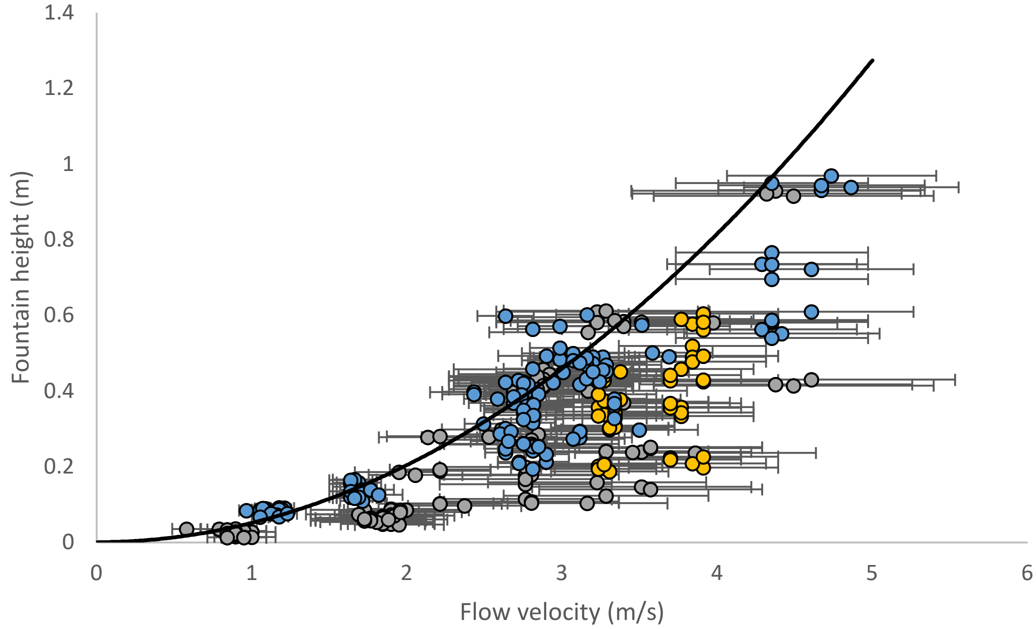

Figure 5.21: Ballistic equation for a projectile (black line) compared to measured fountain height and flow velocity for pipe diameters of 0.01 m (grey data points), 0.018 m (yellow data points) and 0.03 m (blue data points). Error bars denote propagated uncertainties due to assumed errors in measurements.

Filtering the data by pressure head (Fig 5.22) shows that increasing pressure head relates to an increase in flow velocity and fountain height, with the highest fountains and flow velocities corresponding to the largest pressure heads.

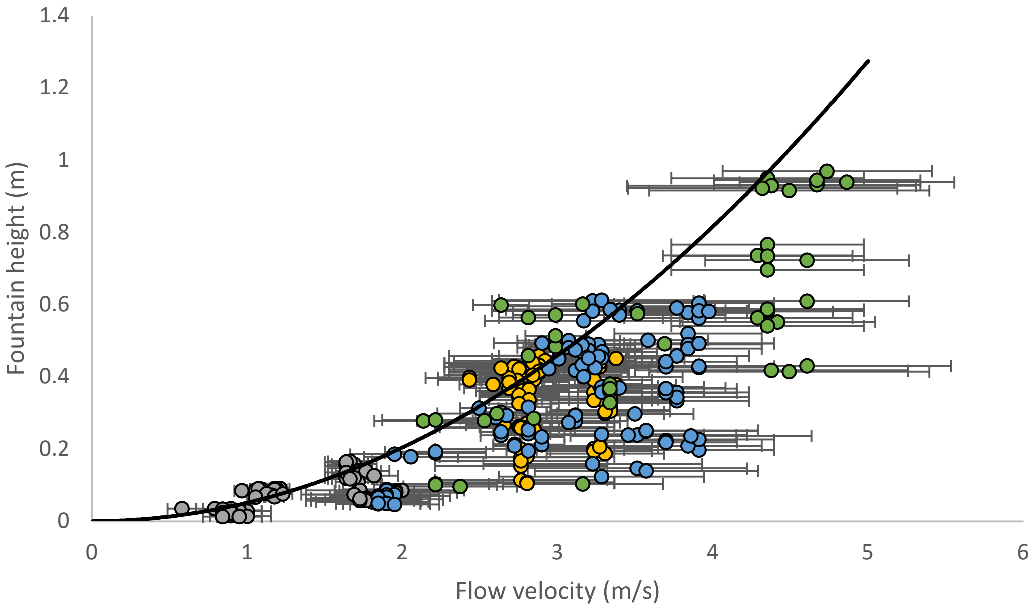

Figure 5.22: Ballistic equation for a projectile (black line) compared to measured values obtained for fountain height and flow velocity for pressure heads of 0.25 (grey data points), 0.75 (yellow data points), 1 (blue data points) and 1.75 m (green data points). Error bars denote propagated uncertainties due to assumed errors in measurements.

5.3.4 Dimensional analysis

As discussed in chapter 2, dimensional analysis allows for the comparison of analogue experiments and behaviours present in the natural volcanic system. Recalling from chapter 2, the equations for dimensionless ponding depth (equation 2.10) and dimensionless fountain height (equation 2.16), the relationship between both these groups will now be examined.

Plotting these two dimensionless groups together produces a visible systemic trend (Fig 5.23) that is identical for both water and syrup solution (Fig 5.24), which is expected when non-dimensionalization is successful.

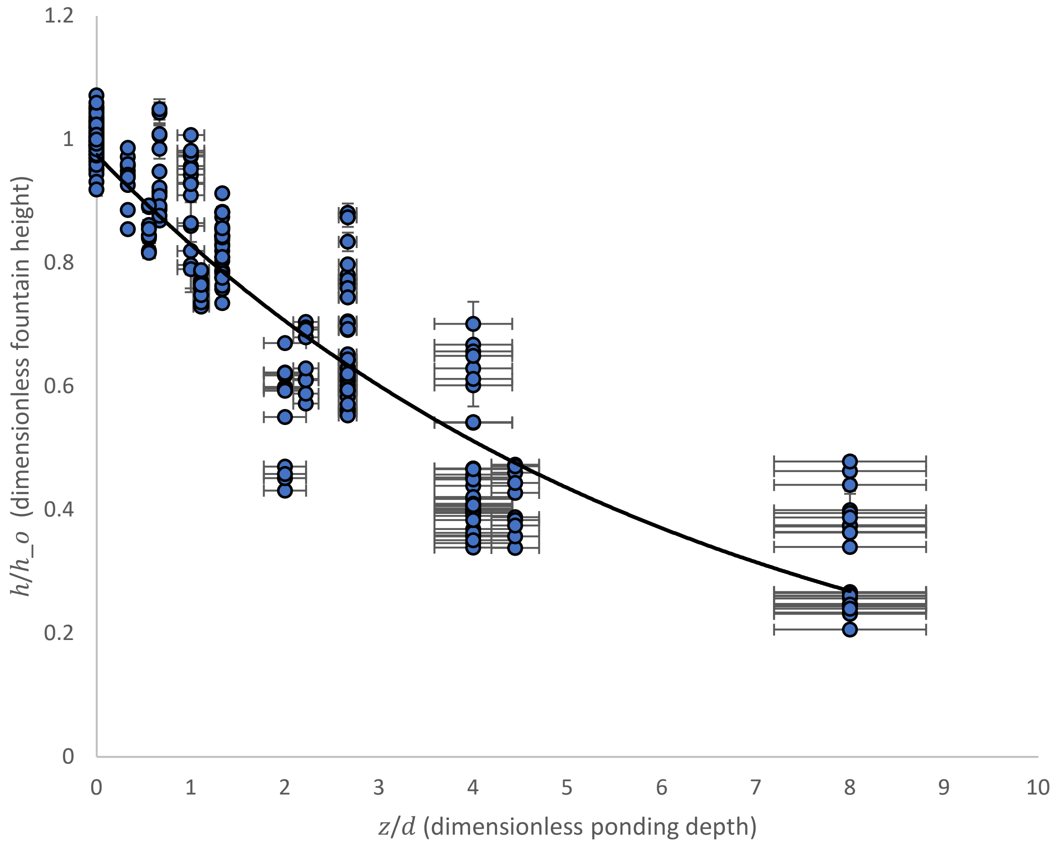

Figure 5.23: Variation of dimensionless fountain height with dimensionless ponding depth. Best fit line is of the form $\frac{h}{h_o} = e^{-1.61\frac{z}{d}}$, ($\mathrm{R}^2$ =0.8539). Error bars denote propagated uncertainties due to assumed errors in measurements.

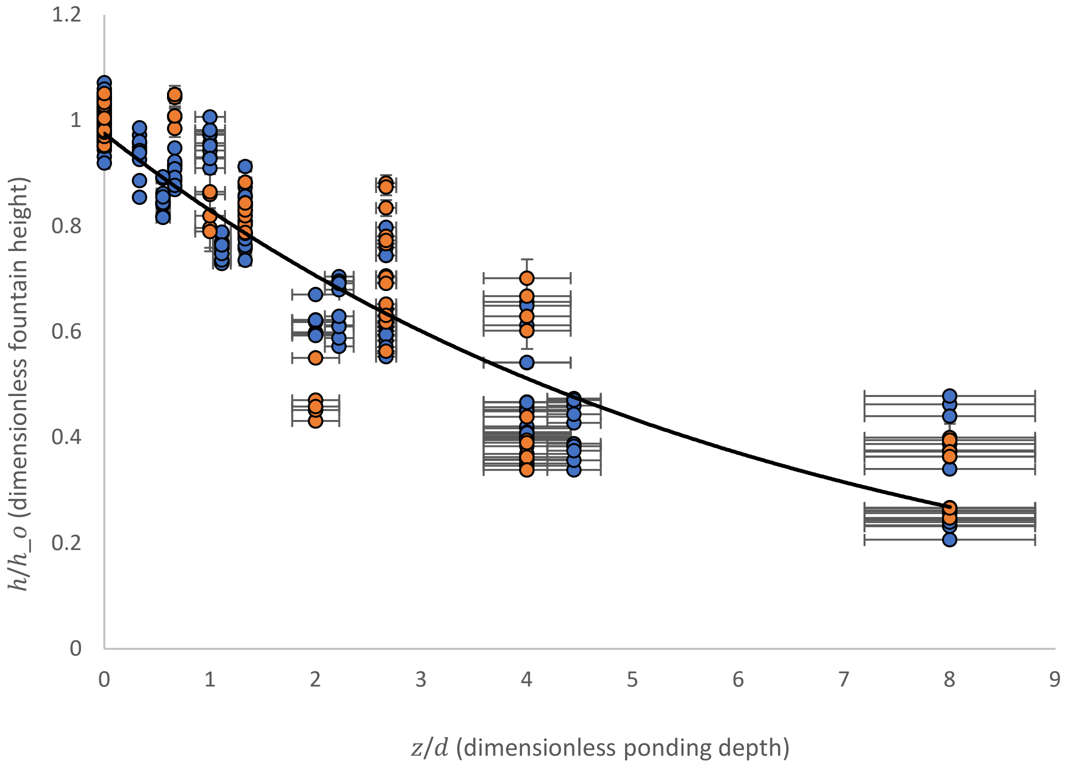

Figure 5.24: Variation of dimensionless fountain height with dimensionless ponding depth for water (blue data points) and syrup (orange data points). Best fit line is of the form $\frac{h}{h_o} = e^{-1.61\frac{z}{d}}$, ($R^2$ =0.8539). Error bars denote propagated uncertainties due to assumed errors in measurements.

Characterizing according to ponding depth (Fig 5.25) indicates that increasing dimensionless ponding depth correlates to a decrease in dimensionless fountain height, with the greatest reductions in height $\left(\frac{h}{h_o} \cong 0.2\right)$ occurring when dimensionless ponding depth is at its maximum value $\left(\frac{z}{d} = 8\right)$. When ponding is absent, $\frac{z}{d} = 0$ there is no reduction in fountain height and therefore $\frac{h}{h_o} \cong 1$.

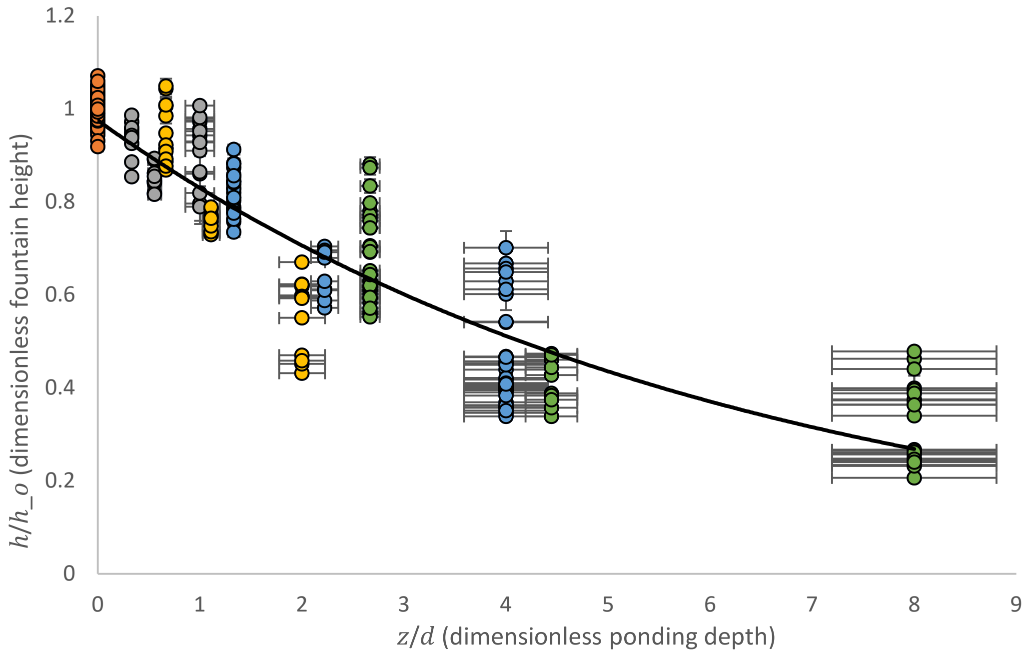

Figure 5.25: Variation of dimensionless fountain height with dimensionless ponding depth for ponding depths of 0 (orange data points), 0.01 (grey data points), 0.02 (yellow data points), 0.04 (blue data points) and 0.08 m (green data points). Best fit line is of the form $\frac{h}{h_o} = e^{-1.61\frac{z}{d}}$, ($R^2$ = 0.8539). Error bars denote propagated uncertainties due to assumed errors in measurements.

Characterizing this relationship for pipe diameter indicates that narrower pipes undergo a greater reduction in fountain height with increased ponding depth (Fig 5.26), with the largest reductions in fountain height $\left(\frac{h}{h_o} \cong 0.2\right)$ occurring for a pipe of D = 0.01 m at pressure head of 1 m. Increased pipe diameter corresponds to lesser reductions in fountain height, with reductions in fountain height being greatest at maximum ponding depth, where $z = 0.08$ m. For a $D = 0.03$ m pipe, a fountain undergoes a reduction of $\frac{h}{h_o} \cong 0.6$. This reduction in fountain height is significantly lower than that experienced by fountains produced using the 0.01 m diameter pipe for otherwise identical physical conditions. When considering this data alongside the relationship presented in figure 5.27, it is apparent that pipe diameter is important when examining fountain behaviour. For a constant pressure head and viscosity, the reduction in height $\left(\frac{h}{h_o} \cong 0.6\right)$ experienced for a fountain produced using a $D = 0.03$ m pipe at $z = 0.08$ m is less than the reduction $\left(\frac{h}{h_o} \cong 0.4\right)$ undergone by a fountain produced using a $D = 0.01$ m diameter pipe at $z = 0.04$ m. The range of values for which $\frac{h}{h_o}$ spans with increasing ponding depth for a 0.03 m diameter pipe $\left(0.5 \leq \frac{h}{h_o} \leq 1\right)$ is lower than the ranges spanned by the $D = 0.018$ m $\left(0.3 \leq \frac{h}{h_o} \leq 1\right)$ and $D = 0.01$ m $\left(0.2 \leq \frac{h}{h_o} \leq 1\right)$ pipes respectively.

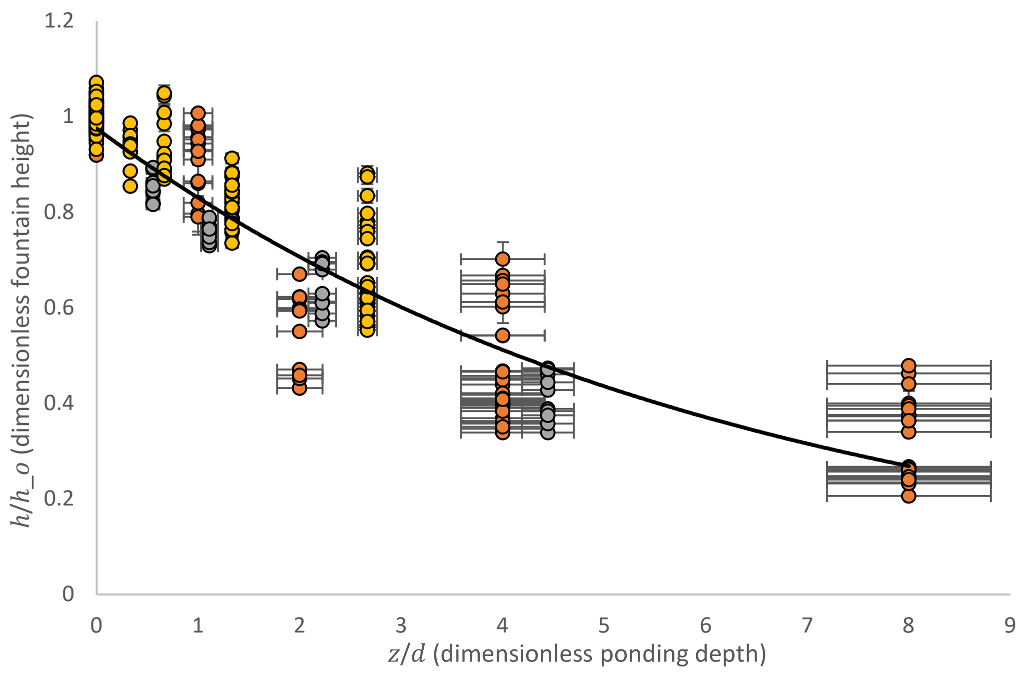

Figure 5.26: Variation of dimensionless fountain height with dimensionless ponding depth for pipe diameters of 0.01 (orange data points), 0.018 (grey data points) and 0.03 m (yellow data points). Best fit line is of the form $\frac{h}{h_o} = e^{-1.61\frac{z}{d}}$, ($\mathrm{R}^2$ = 0.8539). Error bars denote propagated uncertainties due to assumed errors in measurements.

Characterizing the dataset according to pressure head (Fig 5.27) indicates an interesting trend whereby higher pressure head fountain heights undergo greater amounts of fountain height reduction due to ponding depth in comparison to that of lower pressure fountains. For instance; fountains produced using a 0.25 m pressure head for a $D = 0.01$ m pipe at $z = 0.08$ m experienced a reduction of $\frac{h}{h_o} \cong 0.4$. Whilst fountains produced using a 1 m pressure head and otherwise identical parameters underwent a reduction of $\frac{h}{h_o} \cong 0.3$. Similarly, this relationship holds true for fountains produced using $D = 0.018$ and $D = 0.03$ m, with higher pressure fountains again undergoing a greater a reduction in height with increased ponding depth in comparison to their lower pressure counterparts.

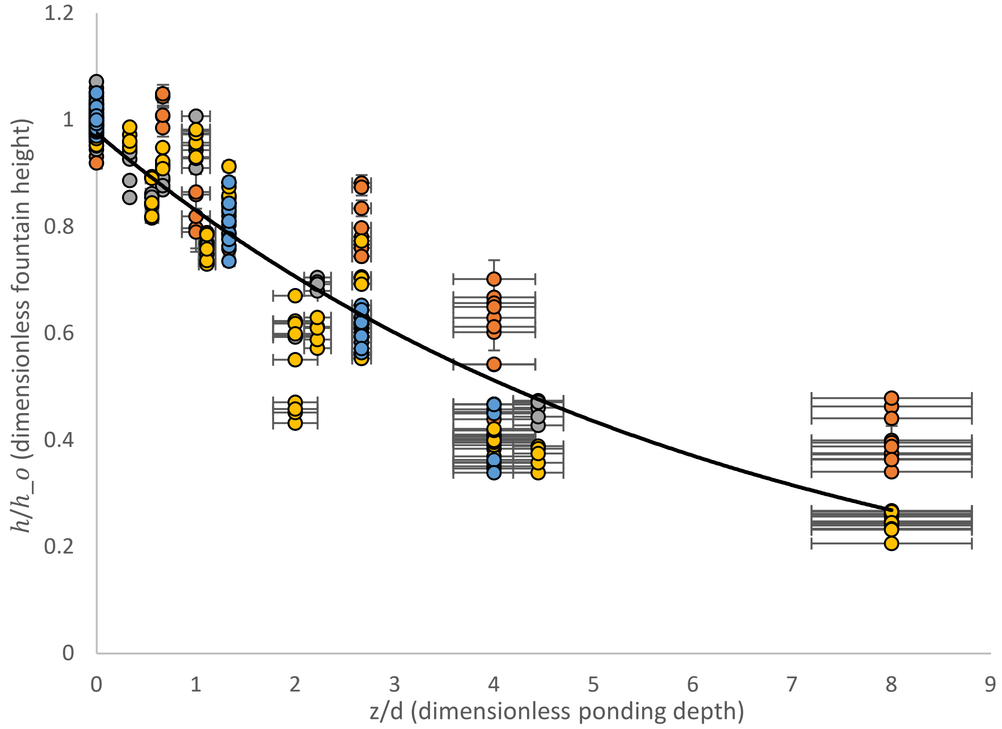

Figure 5.27: Variation of dimensionless fountain height with dimensionless ponding depth for pressure heads of 0.25 (orange data points), 0.75 (grey data points), 1 (yellow data points) and 1.75 m (blue data points). Best fit line is of the form $\frac{h}{h_o} = e^{-1.61\frac{z}{d}}$, ($R^2$ = 0.8539). Error bars denote propagated uncertainties due to assumed errors in measurements.

6. Discussion and Conclusions

6.1 Introduction

The intention of this thesis was to experimental investigate the interaction between fountain height and ponding depth, using carefully scaled experiments to facilitate a direct comparison between experimental fountains and natural lava fountains. Many processes were observed and recorded during the course of this study, leading to the creation of a model for dimensionless fountain height against dimensionless ponding depth.

This chapter discusses these findings in the context of modelled and natural fountain behaviour. Theoretical models for lava fountains are examined first, evaluating the key factors determining fountain height in published literature versus those determined experimentally during this study. Comparisons to natural lava fountains are then considered for several fountaining episodes of the Puu Oo eruption of the Kilauea volcano in Hawaii, between 1983 and 1984.

The implications of these findings and how they might better inform observations of lava fountains in nature is then discussed, followed by possible avenues of future work that could be explored to build upon the initial findings presented in this thesis. The chapter then concludes with a recap of the key findings of this study.

6.2 Comparison to fountain models

As discussed previously in chapter 5, the ballistic equation has been used in published theoretical studies as a simplistic method of calculating lava fountain heights, with the assumption that the erupted mass is only comprised of pyroclasts (Head and Wilson 1987, Wilson et al 1995). The data collected by this investigation indicates that this a suitable method of calculating lava fountain heights in the absence of ponding, as experimentally derived values are consistent with those calculated by the ballistic equation. However, there are increasing discrepancies between experimental values and calculated fountain heights as ponding depth increases. This relationship suggests that the ballistic equation is an ineffective method by which to examine scenarios where lava fountains and ponding are present together, as calculated values will diverge from observed values for fountain height.

Existing lava fountain models indicate that fountain height is determined by a complex function of several parameters, namely; gas content, volumetric flux, conduit geometry and entrainment (Wilson et al 1995, Parfitt et al 1995, Head and Wilson 1987, Wilson and Head 1981). Of these parameters, the most impactful in determining fountain behaviour are volumetric flux and entrainment, a relationship which appeared consistent with results obtained during the course of this study via laboratory experiments and subsequent data analysis (Wilson et al 1995, Parfitt et al 1995, Witt et al 2018). Increasing volumetric flux in experiments corresponded to increased fountain heights, with the largest fountains being produced by the largest volumetric fluxes. In contrast, entrainment had the opposite effect on fountain height, with increasing entrainment corresponding to decreasing fountain heights, due to incorporating pre-erupted material into the ascending fountain, reducing the flow velocity (Wilson et al 1995, Witt et al 2018).

Altering conduit geometry during experiments also influenced fountain heights, fountain height was found to increase when increasing conduit diameter, as this allowed for higher degrees of volumetric flux and reduced frictional effects within the conduit, a relationship which is consistent with previous work (Wilson et al 1995, Parfitt et al 1995, Witt et al 2018). Published studies also indicate that volumetric flux decreases with increasing fluid viscosity, as more viscous fluids act to hinder flow within a conduit, this phenomenon was evident during the course of data analysis, with fountains produced using a syrup solution displaying lower degrees of volumetric flux in comparison to those produced using water (Wilson and Head 1981, Giberti and Wilson 1990).

An interesting result identified within this study, is the interaction between increasing volumetric flux and ponding (and therefore increasing entrainment) and how that affects fountain heights. Published findings indicate that fountains become less susceptible to the effects of entrainment with increasing volumetric flux (Wilson et al 1995). When examining this relationship using the dimensionless model presented in chapter 5, larger volumetric fluxes would therefore be expected to correspond to lesser reductions in fountain height, in comparison to fountains produced using lower volumetric fluxes for otherwise identical ponding depths. However, the findings presented within this study instead point towards a more complicated relationship between volumetric flux and entrainment.

When producing experimental fountains with increasing conduit diameter and ponding depth (with all other parameters kept constant) the relationship between volumetric flux and entrainment proposed by the Wilson et al 1995 model is found to be accurate, fountains produced using larger conduit diameters are less affected by the entrainment process. However, this relationship does not hold when varying pressure head as an experimental parameter (which also changes the volumetric flux). Increasing pressure head corresponds to an increase in volumetric flux, but for increasing pressure head and increasing ponding depth (with all other factors kept constant), higher pressure head fountains underwent a greater reduction in vertical fountain height in comparison to their lower pressure head counterparts.

Despite this seemingly conflicting fountain behaviour, an explanation may exist when considering the phenomenon of lateral dispersion discussed previously in chapter 5. Figures 6.1 and 6.2 below are sampled from chapter 5 for the purposes of providing a reminder of this behaviour to supplement this explanation.

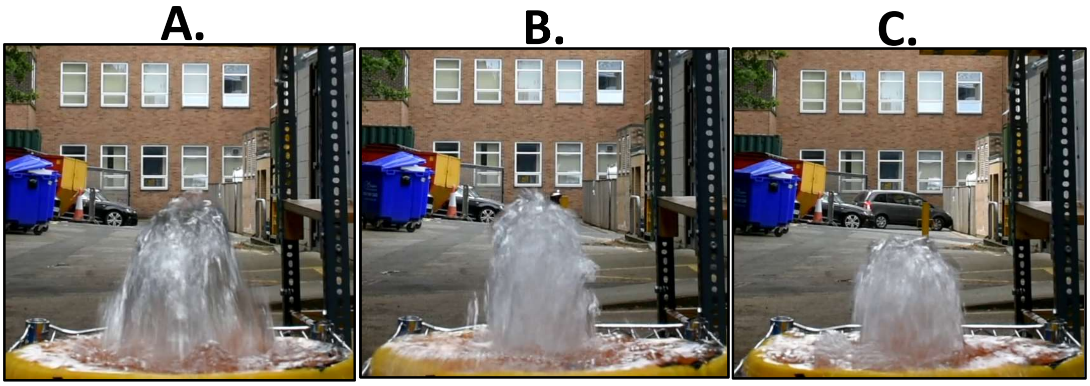

Figure 6.1: Three fountains produced using water at $\Delta l = 0.25$ m with a $D = 0.03$ m pipe at 3 different ponding depths. A) A 0.17 m fountain for $z = 0$ m B) A 0.13 m fountain for $z = 0.04$ m C) A 0.12 m fountain for $z = 0.08$ m.

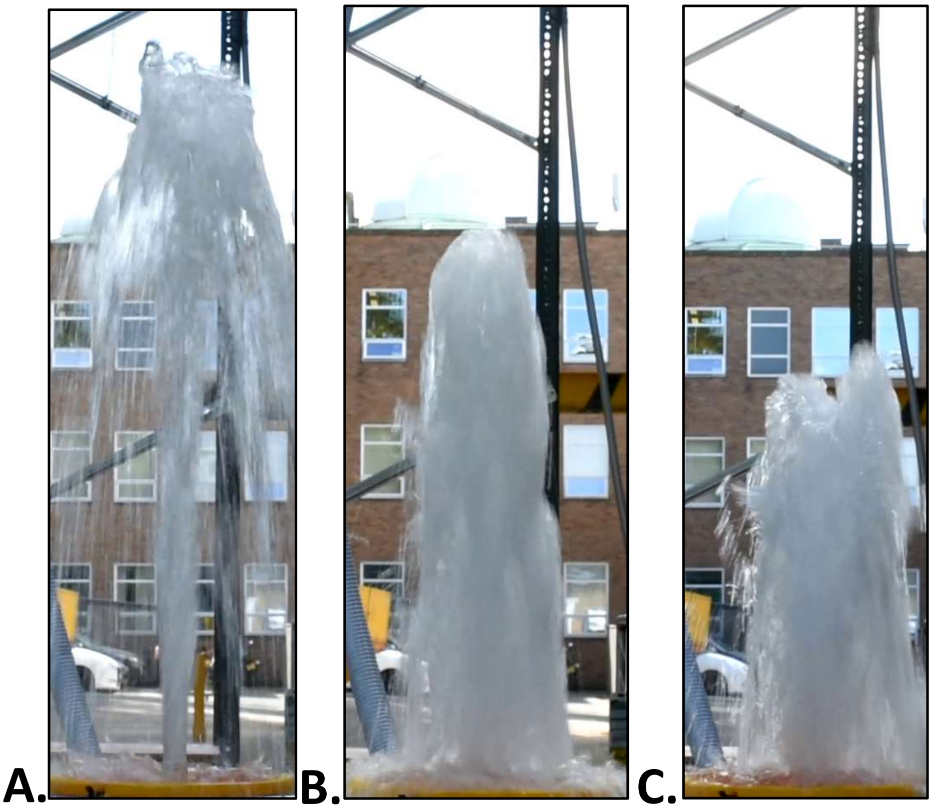

Figure 6.2: Three fountains produced using water at $\Delta l = 1.75$ m with a $D = 0.03$ m pipe at 3 different ponding depths. A) A 0.94 m fountain for $z = 0$ m B) A 0.70 m fountain for $z = 0.04$ m C) A 0.58 m fountain for $z = 0.08$ m.

As is evident from these figures, although the fountains produced using the higher pressure head undergo a greater reduction in fountain height with increased ponding, this reduction is accompanied by an increased lateral thickening of the fountain body. This process is perhaps an indicator that these fountains only appear more susceptible to entrainment when strictly considering vertical fountain height and that the relationship between volumetric flux and entrainment proposed by Wilson et al 1995 is still a valid one, given that such a relationship remains accurate when varying conduit diameter.

6.3 Comparison to natural fountains

Much like for theoretical fountain models, experimental fountains possess several behavioural similarities to those documented in nature. The previously discussed relationship between volumetric flux and fountain height is consistent with observed behaviour of historical eruptions such as; Mauna Ulu and Puu Oo of Kilauea, Hawaii, or Holuhraun in Iceland (Richter et al 1970, Swanson et al 1979, Wolfe et al 1988, Witt et al 2018). In 1983 over the course of several fire fountaining episodes at Puu Oo, a consistent pattern emerged whereby increasing volumetric flux from an active vent would correspond to increased lava fountain heights, with fountains reaching several hundred meters in height (Wolfe et al 1988). Likewise, for the 1969-71 eruption of Mauna Ulu, peak eruption rates coincided with the largest fountains, reaching up to 540m in height (Swanson et al 1979).

Altering conduit diameter is also documented to have similar effects upon natural fountains to those witnessed within the laboratory. During the 1959-1960 eruption of Kilauea, slumping material within a cone with an active vent partially clogged the conduit, leading to a noticeable reduction in fountain height during successive fountain episodes while the blockage persisted (Richter et al 1970). Analysis of several simultaneously active vents during the 2014-2015 eruption of Holuhraun saw a similar relationship, whereby vents fed by wider conduits generally achieved greater fountain heights than those with narrower conduits (Witt et al 2018).

The effects of entrainment are also apparent when examining historical eruptions, the 2011 Kamoamoa saw fountaining behaviour suppressed entirely due to ponding at various points during the eruption, while active vents at Holuhruan achieved lower fountain heights where great ponding depths were present (Orr et al 2015, Witt et al 2018).

The effectiveness of the dimensionless fountain height model will now be examined for several initial episodes of the historic 1983 Puu Oo eruption. Fountaining episodes from this period were chosen due to variations in fountain height being attributed almost entirely to the effects of volumetric flux and entrainment (Parfitt et al 1995).

The Puu Oo eruption began on the 3rd of January 1983 as a fissure eruption, following a series of seismic swarms, and has since been an ongoing eruption within the east rift zone of Kilauea for over 30 years (Heliker et al 2003, Orr et al 2015). Localization of the eruption occurred over time and led to the formation of a central vent, which underwent many episodes of lava fountaining through ponded lavas (Wolfe et al 1988, Heliker et al 2003)

The heights of these lava fountains are well documented (see figures 1.23 and 1.24 of Wolfe et al 1988) throughout these early episodes by Wolfe et al 1988, though several adjustments are required to make the available data suitable for analysis using the dimensionless model. The Wolfe et al 1988 dataset does not accurately record how ponding depth fluctuated during each episode, with the only available data indicating that ponding depths were typically 10 – 20 meters deep while fountaining occurred (Wolfe et al 1988). The only exception to this is during episode 3, where ponding was completely absent (Wolfe et al 1988). Therefore, for the purpose of this analysis it is assumed that the highest fountains during an episode correspond to maximum flux and minimal ponding (when $z = 0$), while the lowest fountain heights correspond to minimum flux and maximum ponding depth. While this assumption may not strictly be accurate, it serves as a useful first approximation that is consistent with established fountain behaviour.

The mean unponded of fountain height can now be identified as the highest fountains during each episode with this assumption, allowing dimensionless fountain height to be calculated. The conduit geometry remained relatively constant throughout episodes 1-20 of the Puu Oo eruption, measuring approximately 20m in diameter (Wolfe et al 1988, Heliker et al 2003). Ponding depth for each fountain can't be determined by normal means due to the vague data available for ponding depths, though an alternative solution is available. Recalling from chapter 5, the line of best for the dimensionless model is of the form: $\frac{h}{h_o} = e^{-1.61\frac{z}{d}}$, which allows ponding depth to be calculated if all other variables are known (The ponding depth for fountains where $\frac{h}{h_o} \geq 1$ is considered to be zero and does not need to be calculated, as these fountains are assumed to undergo no reduction in height). If the calculated values for ponding depth are found to be consistent with values for ponding depth referenced in the literature, the dimensionless model could be considered a successful method for explaining the variation in fountain height with ponding depth for natural lava fountains.

The results of these calculations are presented in figure 6.3, and indicate that while there is some overlap between values calculated using the dimensionless model and the <20 m ponding recorded in the literature, the majority of ponding depths fall into the 0-10 m range instead, which only captures the lower range of ponding depths observed during eruption episodes. These discrepancies maybe the result of dynamic changes during each episode, or perhaps due to errors in the loose assumptions preceding these calculations, which were necessary due to the difficultly with correlating fountain heights and ponding depths for the Wolfe et al 1988 data set.

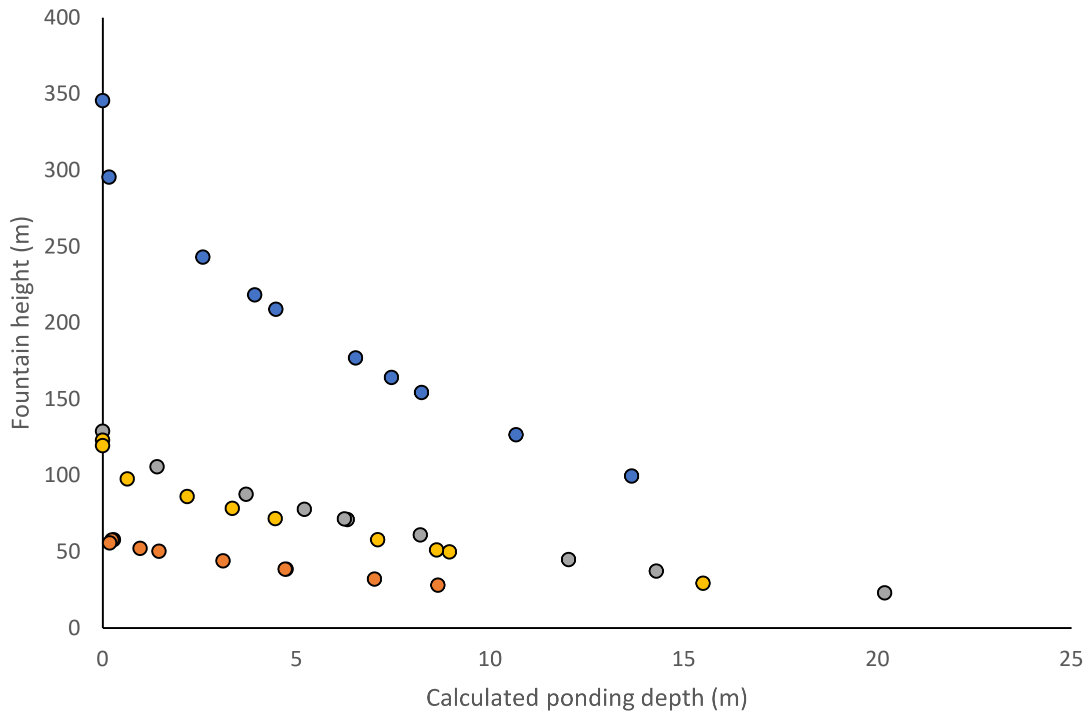

Figure 6.3: Variation of fountain height with calculated values for ponding depth for episodes 4 (orange), 6 (grey), 13 (yellow) and 15 (blue) of the 1983 Puu Oo eruption (values for fountain heights obtained from Wolfe et al 1988).

Additionally, although using the calculated values for ponding depth to produce a dimensionless model (figure 6.4) will give a perfect curve (given that the line of best fit was used to calculate ponding depth values) it also highlights a further discrepancy between natural processes and laboratory models. Episode 3 is documented in the literature as being devoid of ponding during the course of the eruption, yet the fountain heights varied considerably over the course of the episode, a behaviour for which the dimensionless model is unable to account for.

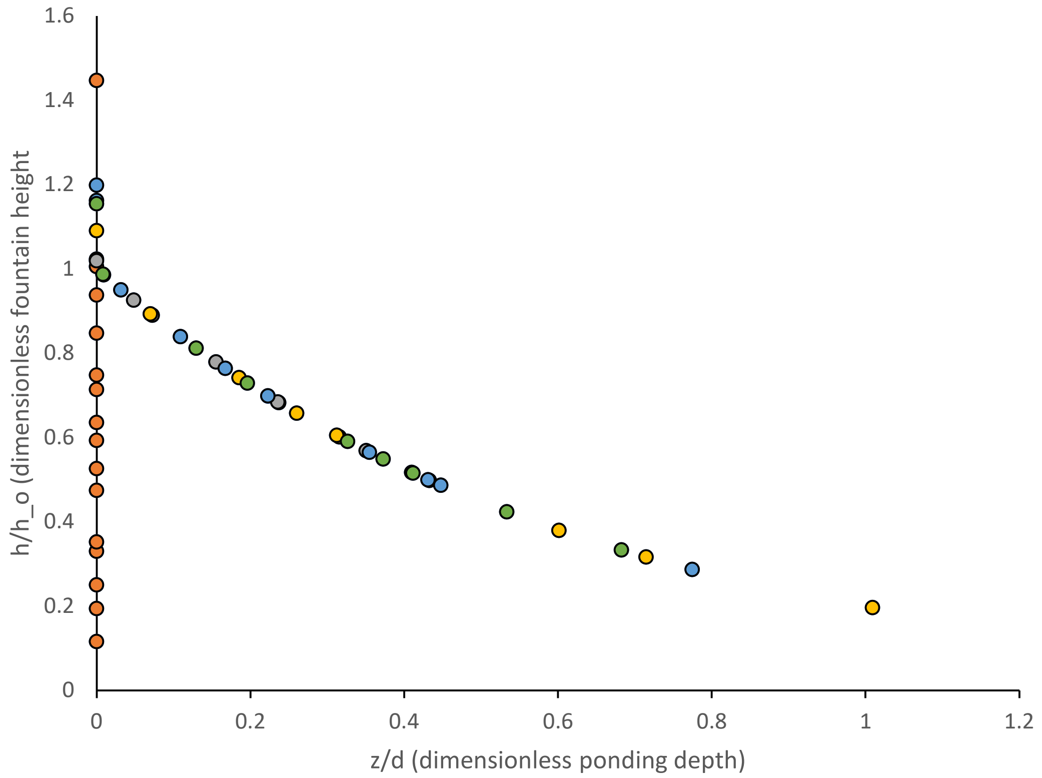

Figure 6.4: Variation of dimensionless fountain height with dimensionless ponding depth for episodes 3 (orange), 4 (grey), 6 (yellow), 13 (blue) and 15 (green) of lava fountaining during the 1983 Puu O'o eruption of Kilauea, Hawaii

6.4 Implications of findings

These findings document the pivotal role volumetric flux and entrainment play in defining fountain behaviour through extensive experimental testing, while also providing support to previously published theoretical studies that have suggested similar relationships. These results formed the basis of a dimensionless model, intended to replicate occurring within natural lava fountains, though was unable to fully do so. Potential future iterations of this model may have more success in completely capturing natural lava fountain behaviour. Nevertheless, this model serves as a useful tool to approximate the impact that ponding may have on subsequent lava fountain heights in the field, potentially identifying scenarios where lava fountains may be prone to suppression. The consequences of conduit suppression can alter ongoing basaltic eruptions, due to solidification and eventual shutdown within a conduit, shifting the eruptive focus to alternative vents (Delaney and Pollard 1982. Witt et al 2018). Similarly, pre-existing topography presents scenarios in which ponding and consequently suppression may occur (Jones et al 2017). As a result, identifying areas of potential stagnation may allow for more informed decision making when monitoring ongoing eruptions, such as providing insight into underlying changes of conduit geometry.

6.5 Future Work

While this study has provided insight into how fountains behave for a cylindrical conduit geometry, many avenues of research remain open for analysing lava fountain behaviour. One such possible direction of continued research could be to examine fountain mechanics for a fissure geometry. Given the common occurrence of lava curtains during basaltic fissure eruptions, quantifying fountain behaviour for a fissure geometry would be of great practical use when examining future basaltic eruptions (Swanson et al 1979, Wolfe et al 1988, Orr et al 2015). This could then be further expanded upon by investigating how the shift from a fissure to cylindrical vent due to localization progressively impacts upon fountain behaviour. The lack of detailed data sets documenting variations of lava ponding and fountain height from active eruptions also presents an interesting challenge. Live monitoring of a central vent eruption with ongoing lava ponding, combined with a methodical approach to data collection may provide even greater insights in fountain behaviour.

6.6 Conclusions

Over the course of this investigation a large data set comprising of over 300 experiments has been produced, providing a wealth of data available for analysis. Parameters were varied systemically for pressure head Δl (m), pipe diameter D (m), fluid viscosity μ (Pa s), and ponding depth z (m). The key findings of this thesis can be summarized as follows:

- Evaluated the effectiveness of the ballistic equation for determining lava fountain heights. It was found to be an effective method of determining the fountain height of un-ponded fountains for both laminar and turbulent flow. Experimental findings indicate that the ballistic equation is ineffective when evaluating fountains that interact with ponded fluids, due to the effects of entrainment. Therefore, the experimental findings are in agreement with published models for un-ponded fountains (Wilson et al 1995).
- Verified that volumetric flux is a key control in determining fountain height for viscous fluids, which is in agreement with previously published models (Wilson et al 1981, Wilson et al 1995, Parfitt et al 1995).
- Demonstrated that fountains with lower volumetric fluxes can be more susceptible to the effects of entrainment compared to those of higher volumetric fluxes, which is supported by previously published literature (Wilson et al 1995, Parfitt et al 1995).

- Identified that there are also scenarios where higher volumetric flux fountains appear more susceptible to the effects of entrainment, and that this process may be linked to lateral dispersion.
- Identified a potential dimensionless model for evaluating the reduction in fountain height encountered with increasing ponding depth. This model was then applied to several fountain episodes of the 1983 Puu Oo eruption of Kilauea, though was unable to fully replicate natural occurring processes, suggesting issues with the model when tackling dynamic changes in sub-surface volcanic processes.

Appendix A – Mathematical Notation

A	Pipe cross-sectional area	m^2
D	Pipe diameter	m
g	Acceleration due to gravity	9.81 $\mathrm{m}/\mathbf{s^2}$
f	Darcy friction factor	dimensionless
h	Fountain height	m
h_L	Head loss	m
h_o	mean un-ponded fountain height	m
k	Number of independent basic units	dimensionless
K_L	Loss coefficient	dimensionless
L	Length	m
M	Mass	kg
m	Number of dimensionless groups	dimensionless
n	Number of governing parameters	dimensionless
P	Pressure	Pa
$\boldsymbol{Q}$	Volumetric flux	m^3/s
r	Pipe radius	m
Re	The Reynolds number	dimensionless
T	Time	s
t	Temperature	℃
V	Flow velocity	m/s
v	Tank volume	m^3
X_{water}	Weight percentage of water	dimensionless
$\boldsymbol{z}$	Ponding depth	m
Δl	Pressure head	m
ΔP	Pressure loss	Pa
Π	Pi group	dimensionless
π	Pi	3.14
ε	Roughness of a pipe	m
ρ	Density	kg/m^3
μ	Viscosity	Pa s

Appendix B – Experimental Apparatus

This section details the physical descriptions and important dimensions of the components that make up the experimental apparatus. Detailed sketches are presented of the tower (figure B.1), tank (figure B.2) and vent (figure B.3).

B.1 Tower

[101]: MDF (medium-density fibreboard) boards form part of the roof and baseplate of the tower structure. MDF was chosen due to its flexibility and ease with which it can be shaped. To prevent moisture absorption, it is treated with varnish.

[102]: Construction timber lengths are arranged to form square frames to which an MDF board can be attached. Screws are placed vertically through the MDF into the oak timber lengths.

[103]: Zinc plated wood screws are used when needed to fasten wooden components together. The zinc plating prevents corrosion. Metal washers are placed between the head of the screws to better distribute the load of the screw on the wood.

[104]: D**exion slotted angle iron lengths** are affixed to the baseplate and roof. Attached to the interior of the base plate and roof are 4 shorter angle iron lengths, to increase structural stability.

[105]: Herringbone joist struts are fixed to the slotted angle iron lengths around the structure reducing any torque forces and providing lateral support to the construct.

[106]: Steel footplates provide structural stability when secured to the base of the tower. A galvanised finish prevents rusting.

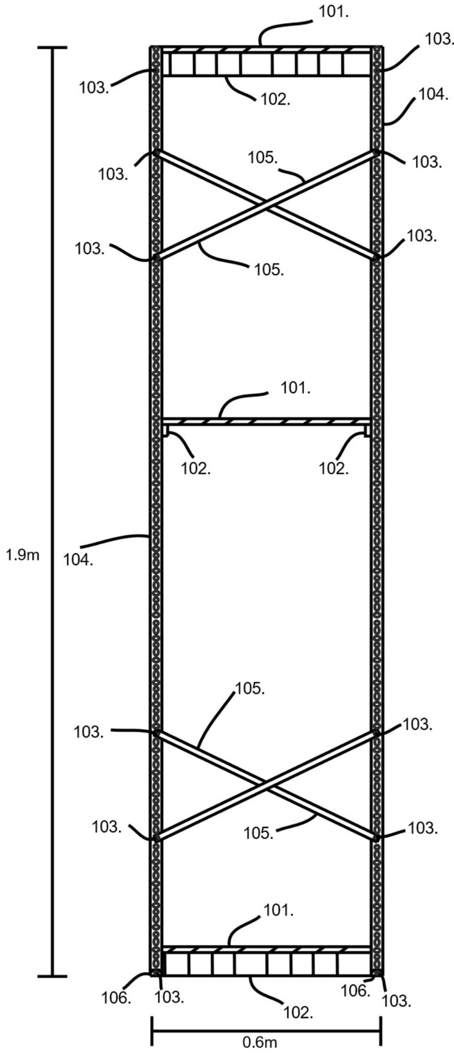

Figure B.1: Technical sketch detailing the components of the tower. It is made up of the following components: [101] mdf (medium-density fibreboard) boards, [102] construction timber, [103] Zinc plated wood screws, [104] dexion slotted angle iron lengths, [105] herringbone joist struts and [106] steel footplates.

B.2 Tank

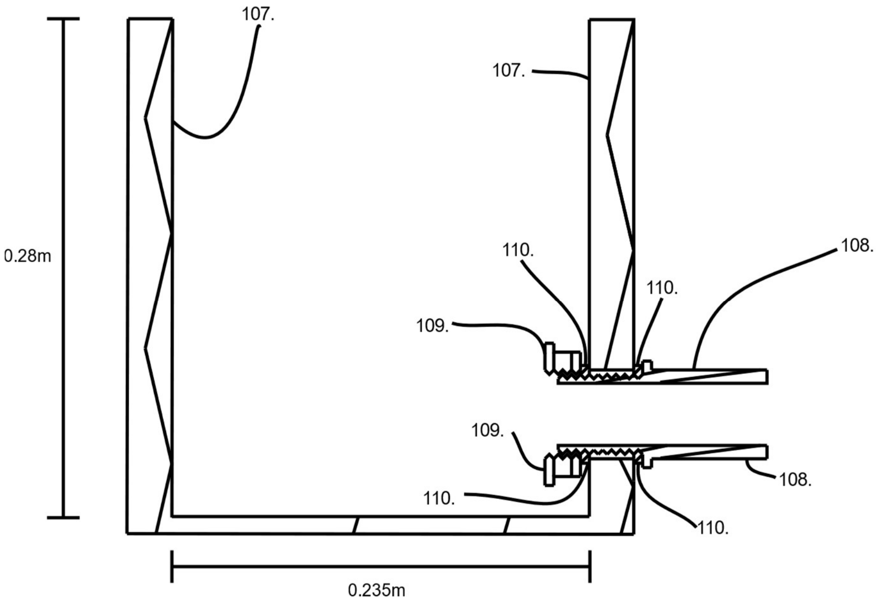

Figure B.2: Technical sketch detailing the components of the tank. It is made up of the following components: [107] transparent tank, [108] pvc (polyvinyl chloride) threaded male hosetails, [109] pvc threaded female backnut and [110] o-rings.

[107]: Transparent tank stores fluid to fuel experimental runs.

[108]: PVC (polyvinyl chloride) threaded male hosetails can be screw into any female socket to provide an area for attaching a hose pipe. To securely attach the pipe, a might t-clamp is placed over the pipe and tightened until firm. This prevents leakages of fluid at the junction between both components.

[109]: PVC threaded female backnut affixes to the threaded male hosetail fitting and compresses against the bulkhead of the tank. It has a hexagonal shape and the large surface area of the backnut allows for a more even distribution of pressure, to prevent any possibility of bulkhead fracturing when tightly screwed.

[110]: O-rings are a synthetic rubber ring, preventing unwanted leakages from the tank. They create an impermeable boundary when inserted between the junctions of pipe fittings and compressed.

B.3 Vent

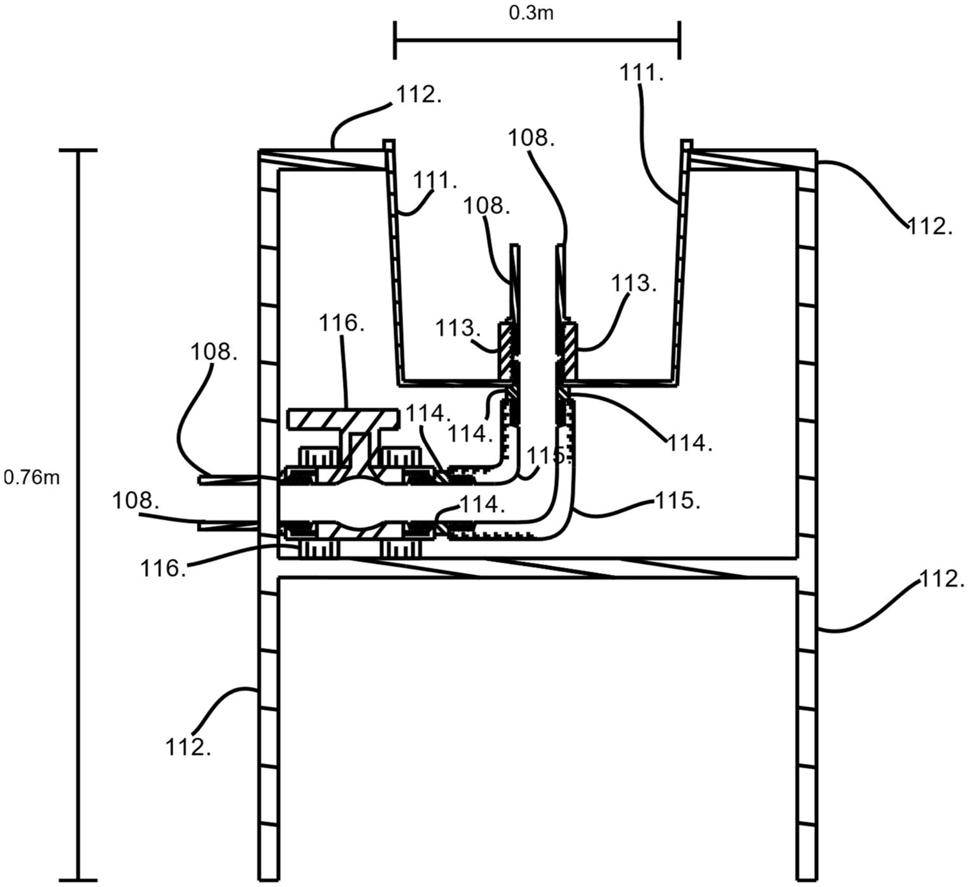

Figure B.3: Technical sketch detailing the components of the vent. It is made up of the following components: [108] pvc (polyvinyl chloride) threaded male hosetails, [111] cylindrical plastic tank, [112] heavy duty chrome shelving unit, [113] pvc threaded female socket, [114] pvc threaded male nipple, [115] 90^0 female threaded elbow and a [116] pvc ball valve EPDM threaded.

[111]: Cylindrical plastic tank with an opening cut into the base of the tank allows fluid to be fed by a pipe with attached plumbing fixtures. Silica sealant is applied around the perimeter of the opening to ensure the tank maintains a constant fluid level when filled.

[112]: Heavy duty chrome shelving unit provides a stable base with two metallic shelves; the upper shelf has an opening created to accommodate the cylindrical plastic tank. The second shelf is spaced below the upper shelf such that a ball valve and other pipe fixtures rest upon it.

[113]: PVC threaded female socket creates a bridge between two male fittings when they are inserted into the socket. Polytetrafluoroethylene (PTFE) tape is placed on the threads of the male fittings, preventing fluid from leaking along the threads of the fitting.

[114]: PVC threaded male nipple screws into two female plumbing fittings to create a junction between them. PTFE tape is laced along the threads of the nipple.

[115]: 90^0 **female threaded elbow** directs fluid upwards from the horizontal ball valve and pipe into the artificial vent.

[116]: PVC ball valve EPDM threaded at the base of the vent controls the flow of fluid. The valve is manually operated and prohibits flow when closed. Opening the

[117]: 2” PVC flexible light duty hose connects the tank and vent. The interior of the pipe is smoothed to reduce friction and the exterior is bound by rigged plastic rings, preventing any expansion or contraction of the pipe.

Appendix C – Mathematical Derivations

This section contains the complete derivations for the equation of maximum flow velocity and the Hagen-Poiseuille equation, as discussed in chapter 4.

C.1 Maximum flow velocity:

For an incompressible fluid, undergoing steady state flow along an impermeable, inelastic circular pipe of radius R, a cylindrical element of fluid with radius dr and length dx moves within a parallel streamline with a constant velocity (Figure C.1)

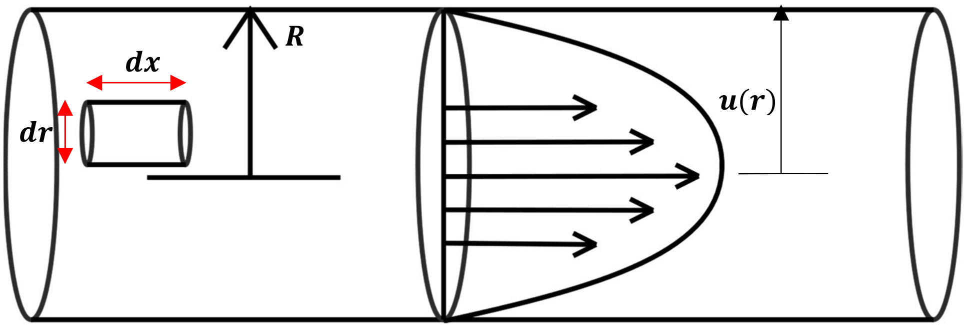

Figure C.1: A fluid element of incompressible fluid with radius dr and length dx travelling in the direction of flow within a pipe of radius R. Velocity as a function of radial position within the pipe is denoted by $u(\mathrm{r})$.

As the velocity of the fluid element remains constant, acceleration is zero and the forces acting upon the element must balance. Performing a force balance (Figure C.2) of the fluid element then gives the following equation:

$$(2\pi r dr P)_x + (2\pi r dx \tau)_r = (2\pi r dr P)_{x+dx} + (2\pi r dx \tau)_{r+dr} \qquad \text{C.1}$$

where dr is the radius of the fluid element, P is the pressure acting on the fluid element, r is the radial distance of the element from the centreline of flow and τ is the wall shear stress (Pa). The subscripts denote the relative positions of each force relative to one another, with $x + dx$ being the force acting on the element at a distance x plus the element length dx and $r + dr$ being the force acting on the element at a radial distance r plus the element radius dr.

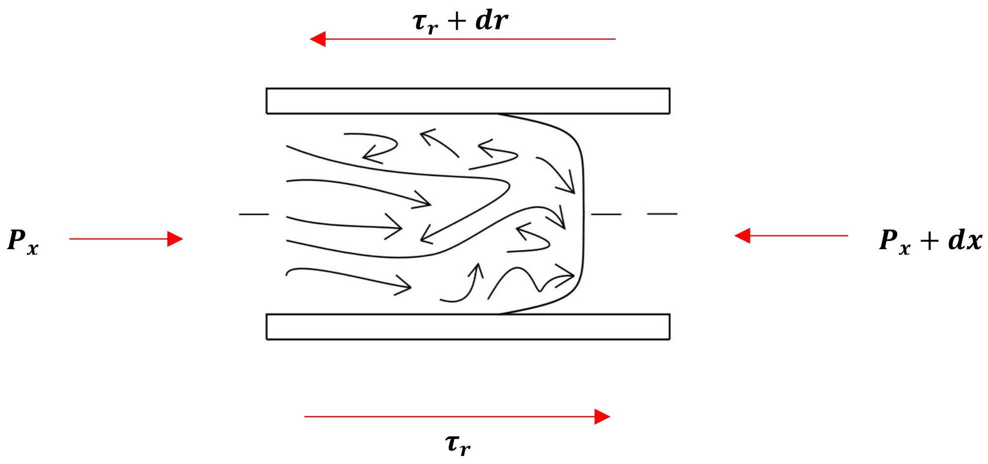

Figure C.2: Force balance on a fluid element of radius dr and length dx. Where P is the pressure acting on the fluid element and τ is the wall shear stress acting on the element. The subscripts denote relative positions of each force to one another in the lateral and radial directions.

Dividing by $2\pi drdx$, then rearranging the equation and taking the limits when dr

And dx are equal to zero gives:

$$r\frac{(dP)}{dx} + r\tau\frac{d}{dr} = 0. \tag{C.2}$$

Taking the relationship between shear stress and viscosity $\left(\tau = -\mu\frac{du}{dr}\right)$ and substituting:

$$r\frac{(dP)}{dx} - \mu r\frac{du}{dr}\frac{d}{dr} = 0. \tag{C.3}$$

Then dividing by μ, rearranging the equation and evaluating the second indefinite integral with respect to r gives:

$$u(r) = -\frac{dP}{\mu dx}\left[\frac{r^4}{4} + C_1 lnr + C_2\right] \qquad \text{C.4}$$

as pressure decreases in direction of flow, $\frac{dp}{dx}$ is negative.

By applying the boundary conditions of $u = 0$ when $r = R$ (due to the effects of the no slip condition and $\frac{du}{dr} = 0$ when $r = 0$, as velocity remains unchanged at the centre of flow due to minimal viscous effects, the equation becomes:

$$u(r) = -\frac{dP}{4\mu dx}[R^2 - r^2]. \qquad \text{C.5}$$

Then taking the equation for the average velocity of flow:

$$V = \frac{2}{R^2}\int_0^R u(r)rdr \qquad \text{C.6}$$

and substituting equation C.6 into equation C.5, then rearranging, simplifying and taking the integral with the limits $r = R$ and $r = 0$ (which are the pipe radius and the centreline of flow respectively), equation C.6 then becomes:

$$V = -\frac{dPR^2}{8\mu dx}. \qquad \text{C.7}$$

Rearranging equation C.7 to solve for $\frac{dP}{dx}$ and substituting into equation C.6 gives:

$$u(r) = 2V\left(1 - \frac{r^2}{R^2}\right). \qquad \text{C.8}$$

To determine the maximum value of velocity, $r = 0$ at the centreline of flow where viscous effects are their minium, equation C.8 then becomes:

$$u_{max} = 2V. \qquad \text{C.9}$$

C.2 Hagen-Poiseuille Equation:

Taking a general expression for the difference in pressure between two points for an incompressible fluid, in an impermeable, inelastic, circular pipe, P_1 and P_2, where $P_2 > P_1$, across a pipe of length L:

$$\frac{dP}{dx} = \frac{P_2 - P_1}{L}. \qquad \text{C.10}$$

Then by substituting equation C.10 into the equation for average velocity (equation C.7) and rearranging for pressure yields:

$$\Delta P = \frac{8\mu LV}{r^2}. \qquad \text{C.11}$$

By rearranging equation C.11 to solve for velocity and then substituting into the formula for volumetric flux $(Q = VA)$, the equation for flux then becomes:

$$Q = \left(\frac{\Delta P r^2}{8\mu L}\right) A. \qquad \text{C.12}$$

Then multiplying out the equation, where $A = \pi r^2$ for circular pipes, gives the equation:

$$Q = \frac{\Delta P r^4}{8\mu L} \qquad \text{C.13}$$

which is the Hagen-Poiseuille equation. This equation is only valid for fluid flow within the laminar regime $(\mathrm{Re} \leq 2300)$.

Bibliography

Abramoff M.D., Magelhaes P.J., and Ram S.J., (2004). Image processing with ImageJ. Biophotonics Int 11:36–42

Bloomfield L.J., and Kerr R.C., 2002. Inclined turbulent fountains. J. Fluid. Mech. Vol. 451 pp. 283-294.

Buckingham, E., 1914. On physically similar systems; illustrations of the use of dimensional equations, Physical review. Vol.4 pp.345-376.

Bruce P.M., and Huppert H.E., 1989. Thermal controls of basaltic fissure eruptions. Nature. Vol 342. 665-667.

Bruce P.M., and Huppert H.E., 1990. Solidification and melting along dykes by laminar flow of basaltic magma. Magma transport and storage, ed MP Ryan, pp. 87-101.

Cengel, Yunus A. and Cimbala, John M., 2014. Fluid Mechanics: Fundamentals and Applications 3rd Edition. Published by Mc Graw Hill India.

Christensen, Nikolas. I., and Wilkens, Roy. H., 1982. Seismic Properties, Density, and Composition of Icelandic Crust Near Reydarfjordur. Journal of geophysical research, Vol. 87 No. B8, Pages 6389-6395.

Colebrook, C. F., 1939. Turbulent flow in pipes with particular reference to the transition region between the smooth and rough pipe laws, Journal of ICE, Vol.11, No.4, 1939, 133-156.

Crisp J.A., 1984. Rates of magma emplacement and volcanic output. Journal of volcanology and geothermal research 20: 177-211.

Daly R.A., Manger G.E., and Clark S.P., 1966. Density of Rocks, Geol Soc Am Mere 97:19 26

Delaney P.T., and Pollard D.D., 1982. Solidification of basaltic magma during flow in a dyke. American journal of science, Vol. 282, P 856-885.

Freret-Lorgeril V., Donnadieu F., Scollo S., Provost A., Freville P., Guehenneux Y., Hervier C., Prestifilippo M., and Coltelli M., 2018. Mass eruption rates of tephra plumes during the 2011-2015 lava fountain paroxysms at Mt. Etna from doppler radar retrievals. Front. Earth Sci. 6:73.

Giberti G., and Wilson L., 1990. The influence of geometry on the ascent of magma in open fissures. Bull Volcanol 52:515-521.

Giordano, D., Russell, J.K, Dingwell,. D.B., 2008. Viscosity of magmatic liquids: A model. Earth and Planetary Science Letters 271, 123-134.

Gonnermann H.M., and Manga M., 2007. The Fluid mechanics inside a volcano. Annu. Rev Fluid Mech. 2007. 39:321-356.

Haaland, S. E., 1981. Simple and explicit formulas for the friction factor in turbulent pipe flow, J. Fluids Eng 105, 89-90.

Head J.W., and Wilson L., 1987. Lava fountain heights at Pu'u 'O'o, Kīlauea, Hawaii: Indicators of Amount and variations of exsolved magma volatiles. Journal of geophysical research. Vol. 92, No. B13, Pages 13715-13719.

Head J.W., and Wilson L., 1998. Basaltic pyroclastic eruptions: influence of gas-release patterns and volume fluxes on fountain structure, and the formation of cinder cones, spatter cones, rootless flows, lava ponds and lava flows. Journal of Volcanology and Geothermal Research, 37: 261-271.

Helfrich K.R., 1995. Thermo-viscous fingering of flow in a thin gap: a model of magma flow in dikes and fissures. J. Fluid Mech. Vol. 305, pp.219-238.

Heliker C., Swanson D.A., and Takahashi T.J., 2003. The Puu Oo-Kupaianaha Eruption of Kilauea Volcano, Hawaii: The First 20 Years. U.S Geological Survey professional paper 1676.

Heliker, C., Kauahikaua J., Sherrod D.R., Lisowski M., and Cervelli P.F., 2003. The Rise and fall of the Puu Oo cone, 1983-2002. U.S Geological Survery professional paper 1676, p 29-51.

Houghton B.F., Taddeucci J., Andronico D., Gonnermann H.M., Pistolesi M., Patrick M.R., Orr T.R., Swanson D.A., Edmonds M., Gaudin D., Carey R.J., Scarlato P., 2016. Stronger or longer: Discriminating between Hawaiian and Strombolian eruption styles. Geology 44: 163-166.

Jones T.J., Llewellin E.W., Houghton B.F., Brown R.J., and Brown C.Vye., 2017. Proximal lava drainage controls on basaltic fissure eruption dynamics. Bull Volcanol 79:81.

Jones, T.J., 2018. Fissures and fountains: magma dynamics in basaltic conduits, PhD thesis, Durham University, England.

Lin Y.J.P., and Linden P.F., 2005. The entrainment due to a turbulent fountain at a density interface. J. Fluid. Mech. Vol. 542, pp. 25-52.

Llewellin, E.W., 2002. The rheology of bubble-bearing magmas: theory and experiments, PhD thesis, University of Bristol, England.

Moody, L. F., 1944. Friction factors for pipe flow, transactions of the A.S.M.E, Vol. 66, 671-684.

Moore, J. G., 2001. Density of basalt core from Hilo drill hole, Hawaii. Journal of Volcanology and Geothermal Research 112 (2001) 221-230

Murase, T., McBirney, A.R., 1973. Properties of some common igneous rocks and their melt at high temperatures. GSA Bulletin 84, 3563-3592

Orr T.R., Poland M.P., Patrick M.R., Thelen W.A., Sutton A.J., Elias T., Thornber C.R., Parcheta C., and Wooten K.M., 2015. Kīlauea’s 5-9 March 2011 Kamoamoa Fissure Eruption and its relation to 30+ years of activity from Pu‘u ‘Ō‘ō. Hawaiian Volcanoes: From source to surface, Geophysical Monograph 208. First edition. Edited by Carey R., Cayol V., Poland M., and Weis D.

Parfitt E.A., and Wilson L., 1995. Explosive volcanic eruptions – IX. The transition between Hawaiian-style fountain and strombolian explosive activity. Geophys. J. Int. 121, 226-232

Parfitt E.A., Wilson L., and Neal C.A., 1995. Factors influencing the height of Hawaiian lava fountains: implications for the use of fountain height as an indicator of magma gas content. Bull Volcanol. 57: 440-450.

Parfitt E.A., 2004. A discussion of the mechanism of explosive basaltic eruptions. Journal of volcanology and geothermal research. 134 77-107.

Percheta C.E., Houghton B.F., and Swanson D.A., 2012. Hawaiian fissure fountains 1: Decoding deposits-episode 1 of the 1969-1974 Mauna Ulu eruption. Bull Volcanol 74:1729-1743.

Poiseuille, J.L.M., 1840. Recherches expérimentelles sur le mouvement des liquids dans les tubes trés petits. C. R. Acad. Sci. Paris, 11, 961-967, 1041.

Tilling R.I., 1987. Fluctuations in surface height of active lava lakes during 1972-1974 Mauna Ulu Eruption, Kilauea Volcano, Hawaii. Journal of Geophysical Research Vol 92 No. B13, p 13721-13730.

Turner J.S., 1966. Jets and plumes with negative or reversing buoyancy. J. Fluid. Mech. Vol. 26 part 4, pp. 779-792.

Reynolds, O., 1883. An experimental investigation of the circumstances which determine whether the motion of water shall be direct or sinuous, and of the law of resistance in parallel channels, Phil. Trans. R. Soc. Lond. 1883 174, 935-982.

Reynolds P., Brown R.J., Thordarson T., Llewellin E.W., 2h016. The architecture and shallow conduits of Laki-type pyroclastic cones: Insights into a basaltic fissure eruption. Bull Volcanol 78:36.

Richter D.H., Eaton J.P., Murata K.J., Ault W.U., and Krivoy H.L., 1970. Chronological Narrative of the 1959-60 Eruption of Kilauea Volcano, Hawaii. U.S Geological Survey professional paper 537 - E

Sigurdsson, H., Houghton, B., Mcnutt, S., Rymer, H., Stix, J., 2015. Encyclopedia of Volcanoes, 2nd edition. Published by Academic Press.

Stovall W.K., Houghton B.F., and Gonnerann H., 2010. Eruption dynamics of Hawaiian-style fountains: the case study of episode 1 of the Kīlauea Iki 1959 eruption. Bull Volcanol 73:511-529.

Sumner J.M., Blake S., Matela R.J., and Wolff J.A., 2005. Spatter. Journal of Volcanology and Geothermal Research. 142, 49-65.

Swanson, D.A., Duffield W.A., Jackson D.B., and Peterson D.W., 1979. Chronological narrative of the 1969-71 Mauna Ulu eruption of the Kilauea Volcano, Hawaii. U.S. Geol. Surv. Prof. Pap., 1056, 55.

Valentine G.A., Gregg T.K.P., 2008. Continental basaltic volcanoes – Processes and problems. Journal of volcanology and geothermal research 177: 857-873.

Wiesbach, J., 1845. Lehrbuch der Ingeniuer- und Maschinen-Mechanik, Vol. 1. Theoretische Mechanik, Vieweg und Sohn, Braunschweig.

Wilson, L., Sparks, R.S.J., Walker, G.P.L., 1980. Explosive volcanic eruptions – IV. The control of magma properties and conduit geometry on eruption column behaviour. Geophys J. R. astr. Soc. 63, 117-148.

Wilson L., and Head J.W., 1981. Ascent and Eruption of Basaltic Magma on the Earth and Moon. Journal of Geophysical Research. Vol. 86, pages 2971-3001.

Wilson, L., Parfitt, E.A., Head, J.W., 1995. Explosive volcanic eruptions – VIII. The role of magma recycling controlling the behaviour of Hawaiian-style lava fountains. Geophys. J. Int. 121, 215-225.

Witt, T., Walter T.R., Müller D., Guðmundsson M.T., and Schöpa A., 2018. The relationship between lava fountaining and vent morphology for the 2014-2015 Holuhraun eruption, Iceland, analysed by video monitoring and topographic mapping. Front. Earth Sci. 6:235.

Wolfe, E.W., (Ed.) 1988. The Puu Oo eruption of Kilauea Volcano, Hawaii: Episodes 1 through 20, January 3, 1983, through June 8, 1984, U.S. Geol Surv. Prof. Pap. 1463, 251.